2008

First Measurement of Top Quark Pair Production Cross-Section in Muon Plus Hadronic Tau Final States

Suharyo Sumowidagdo

THE FLORIDA STATE UNIVERSITY

COLLEGE OF ARTS AND SCIENCES

FIRST MEASUREMENT OF TOP QUARK PAIR PRODUCTION CROSS-SECTION IN MUON PLUS HADRONIC TAU FINAL STATES

By

SUHARYO SUMOWIDAGDO

A Dissertation submitted to the
Department of Physics
in partial fulfillment of the
requirements for the degree of
Doctor of Philosophy

Degree Awarded:
Spring Semester, 2008

The members of the Committee approve the Dissertation of Suharyo Sumowidagdo defended on November 26, 2007.

Todd Adams
Professor Directing Dissertation

Ettore Aldrovandi
Outside Committee Member

Horst Wahl
Committee Member

Laura Reina
Committee Member

Simon Capstick
Committee Member

The Office of Graduate Studies has verified and approved the above named committee members.

To my family and friends who have always believed in me ...

A K U

Kalau sampai waktuku
'Ku mau tak seorang 'kan merayu
Tidak juga kau

Tak perlu sedu sedan itu

Aku ini binatang jalang
Dari kumpulannya terbuang

Biar peluru menembus kulitku
Aku tetap meradang menerjang

Luka dan bisa kubawa berlari
Berlari
Hingga hilang pedih perih

Dan aku akan lebih tidak perduli

Aku mau hidup seribu tahun lagi

Chairil Anwar, 1922-1949

So! now 'tis ended, like an old wife's story

John Webster, c. 1580 - c. 1634

ACKNOWLEDGEMENTS

This dissertation could not have seen the light of the day without the hard work, dedication, and support of many people. First of all, I thank members of the DØ Collaboration and the technical staff of Fermilab that have provided world-class research facilities with their endless hard work, days and nights.

I thank my advisor Todd Adams for being a patient advisor and sharing many wisdoms he has about doing physics analysis. For allowing me to propose and carry out research on a topic of my own, and keep supporting and working with me from the beginning until the end despite all the difficulties and challenges faced.

To Harrison Prosper who has been a second advisor with many discussions I had with him, and for his insights in shaping the analysis strategy. To Horst Wahl, Laura Reina, Simon Capstick, and Ettore Aldrovandi for the time they spent serving in my graduate committee. Horst and Simon provided many useful critics and suggestions which improve the manuscript. To the other faculty members of the experimental high energy physics group at Florida State University, for all the support you gave me all these years.

To members of the DØ Top Group who helped me one way or another during the time I was working on the analysis. Amnon Harel and Dag Gilberg helped me getting started with the analysis framework, and answered a lot of questions I raised. Amnon also helped when I worked on data sets and Monte Carlo samples used in this analysis. Lisa Shabalina for her comments on the analysis note, and her assistance with the evaluation of systematic uncertainties and cross-section combination. Michele Weber for the data quality and luminosity calculation. Michael Begel for many discussions I had with him, and for repeatedly putting me back on track.

To members of the DØ Tau Identification Group for developing and establishing tau identification algorithm. To members of my editorial board for the time they spent on reviewing the analysis note, and for the many suggestions they made. Many of those suggestions made it into the final

version of the dissertation.

To the Florida State University people at Fermilab: Andrew, Bill, Dan, Daekwang, Edgar, Jadranka, Jose, Norm, Oleksiy, Silke, and Trang. Thanks for the time we spent together, and putting up with my antics at the office. For Andrew, Dan, and Oleksiy: thank you for your cheerful attitudes which helped me relieving a lot of tension off my head. Silke Nelson taught me a lot about tau identification algorithm during the earlier phase of this analysis. Daekwang Kau and I joined DØ together in the summer of 2002, and he has been a good friend since then. Especially during the tough period we had together during dissertation writing and defense phase.

To Kathy Mork of the High Energy Physics Office; Sherry Tointigh of the Graduate Student Office; Joy Ira, Marjorie Fontalvo and Erin Skelly of the International Student Center. Thank you for helping me through all the bureaucracy and paperwork related to travel, academic matters, and immigration while I was away at Fermilab.

Down in the control room and deep inside the DØ Assembly Building, I had a demanding but rewarding experience in working with Fritz Bartlett, Geoff Savage, Vladimir Sirotenko, Stan Krzywdzinski, Dean Schamberger, Bill Lee, and Norm Buchanan. I have learned a lot from their work ethics and attitudes. I will always remember that without hard work on the detector side, there will never be any results on the physics side.

To my undergraduate professors at the Nuclear and Particle Theory Group, University of Indonesia. Terry Mart introduced me to the real world of physics research, supervised my first scientific work, and helped me to start a career in physics. The late Darmadi Kusno introduced me to high-energy physics, taught me a lot of physics in and out of class, and always convinced me that there is a real chance, despite all the hardships in Indonesia, to pursue a real career in physics. May his soul rest in peace.

To my housemates Dan and Marco, for being a constant source of fun and entertaiment, and for putting up with my rants and complains.

To my family who have always supported me ever since I decided to pursue a career in physics. For allowing me to be far away in space and time. For always remembering me even during the times when I forget about them and am swamped in my work. I can never thank them enough.

To Jutri Taruna and Alvin Kiswandhi, my sister and brother here in the United States, a place so far away from our home country. It has been a long journey we've been through together. From our days in Depok and Salemba. I couldn't have done it without you, and words will never be enough to express my feelings of gratitude for you.

TABLE OF CONTENTS

LIST OF TABLES

LIST OF FIGURES

ABSTRACT

This dissertation presents the first measurement of top quark pair production cross-section in events containing a muon and a tau lepton. The measurement was done with 1 fb^{-1} of data collected during April 2002 through February 2006 using the DØ detector at the Tevatron proton-antiproton collider, located at Fermi National Accelerator Laboratory (Fermilab), Batavia, Illinois. Events containing one isolated muon, one tau which decays hadronically, missing transverse energy, and two or more jets (at least one of which must be tagged as a heavy flavor jet) were selected. Twenty-nine candidate events were observed with an expected background of 9.16 events. The top quark pair production cross-section is measured to be

$$\sigma(t\bar{t}) = 8.0^{+2.8}_{-2.4}\,(\text{stat})^{+1.8}_{-1.7}\,(\text{syst}) \pm 0.5\,(\text{lumi})\ \text{pb}.$$

Assuming a top quark pair production cross-section of 6.77 pb for Monte Carlo signal top events without a real tau, the measured $\sigma \times \text{BR}$ is

$$\sigma(t\bar{t}) \times BR(t\bar{t} \to \mu + \tau + 2\nu + 2b) = 0.18^{+0.13}_{-0.11}\,(\text{stat})^{+0.09}_{-0.09}\,(\text{syst}) \pm 0.01\,(\text{lumi})\ \text{pb}.$$

CHAPTER 1

FOUNDATIONS

1.1 The Standard Model of Particle Physics

This dissertation presents an investigation in the field of elementary particle physics, whose goal is to understand the fundamental constituents of matters and the laws governing them. The standard model (SM) is the currently accepted theory which describes a vast range of phenomena in elementary particle physics, including the strong, weak, and electromagnetic interactions. It is consistent, renormalizable, and has been tested in precision to a high degree of accuracy.

There are two key features of the standard model. The first one is gauge invariance, which means the physics described by the standard model should not change under phase transformations which are functions of space-time coordinates. The second is the Higgs mechanism, the formalism which endows the particles of the standard model with mass.

The gauge invariance principle constrains the particle contents and the interactions between them in a unique way. Given a set of particles, the symmetry group of transformation, and the gauge bosons, the principle defines the form of interactions between the particles mediated by the bosons. The standard model is a theory based on the $SU(3)_C \times SU(2)_L \times U(1)_Y$ symmetry groups. The subscript C, L, and Y refers to the *color* group, *left-handed, weak isospin* group, and *weak hypercharge* group, respectively.

A theory of fundamental particle interactions built from the gauge invariance principle alone doesn't allow the existence of massive gauge bosons. In the standard model, the masses of the gauge bosons of weak interactions are generated by the *Higgs* mechanism. It transforms degrees of freedom in the Higgs field(s), which are scalar field(s), into masses of the weak gauge bosons. In elementary particle theory, the Higgs mechanism that generates these masses is also known as *electroweak symmetry breaking*. Within the electroweak theory, the Higgs mechanism is also resposible for generating the masses of the fermion contents of the standard model.

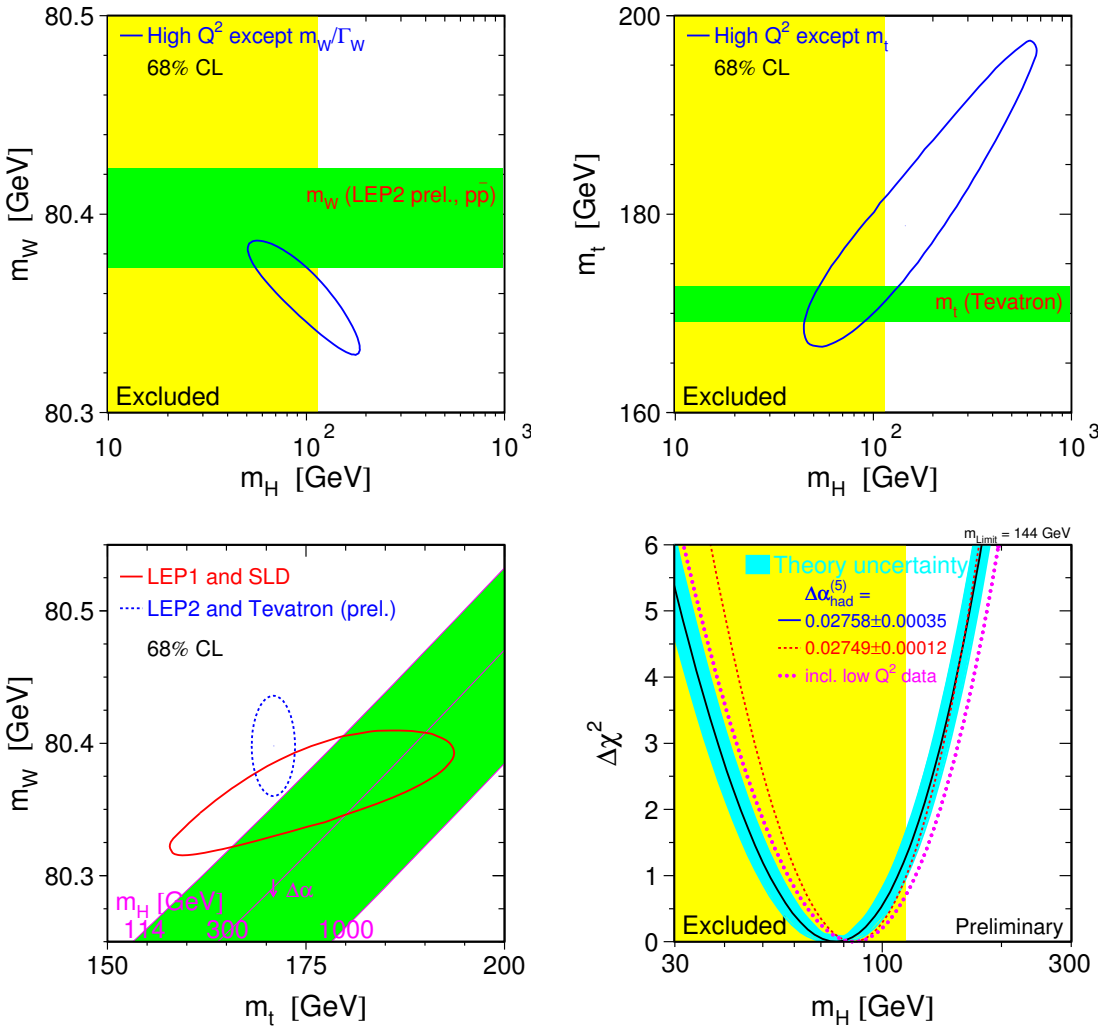

Figure 1.1: Plots of electroweak constraints of the mass of the standar model Higgs particle from other standard model measurement. Top left: constraints from the mass of W bosons, m_W; top right: constraints from the mass of the top quark, m_t; bottom left: constraints from both mass of the top quark and the W bosons, bottom right: constraints from the global electroweak fit. Figures are taken from the report of LEP Electroweak Working Group [1].

There is no unique formulation of the Higgs mechanism in the standard model. It is therefore more custom to use the term *Higgs sector* when discussing the more general aspects of electroweak symmetry breaking and the origin of mass of standard model fermion. In the standard model, the minimal implementation of the Higgs mechanism is an $SU(2)$ doublet which corresponds to the existence of an electrically neutral, scalar particle.

A tremendous amount of effort has been put to explore and understand the Higgs sector of the standard model. As of the year 2007, there is no direct experimental confirmation of the physics of the Higgs sector, be it the minimal one or any of the extended ones. The available knowledge about the Higgs sector is obtained by constraints from other parts of the standard model. Figure 1.1 shows four graphs that show the constraints on the minimal standard model Higgs from other well-measured parameters of the standard model.

An important property of the Higgs particles[1] is that the couplings between Higgs particles and other particles are proportional to the other particles' masses. The top quark is currently the heaviest known particle, and is expected to play important role in the exploration of electroweak symmetry breaking mechanism. The next section discusses top quark production and decays at the Tevatron.

1.2 Top Quarks Production and Decay

In 1995, two major collaborations at Fermilab announced the discovery of the top quark [2, 3]. It was observed in the form of $t\bar{t}$ or top quark-antiquark pair production (hereby will be loosely addressed by the term "top quark pair"). The discovery verified the previous theoretical prediction for the existence of three generations of quarks. Due to the small amount of data, enormous backgrounds, and tight cuts in triggering and analysis, each of the collaborations could obtain only tens of top quark events. Those events were just enough for both groups to claim observation. Using the complete data set recorded from 1992 to 1996 at the Tevatron[2], the collaborations were able to measure the top quark mass and top quark pair production cross section at the corresponding center-of-mass energy.

Figure 1.2 shows the four leading-order Feynman diagrams for top quark pair production at the Tevatron via strong interaction. At the Tevatron's center-of-momentum (c.m.) energy of 1.96 TeV, the quark fusion process dominates (85%) over the gluon fusion (15%) processes in contributing

[1] Plural form is chosen.

[2] This period of Tevatron operation is often referred as "Run I".

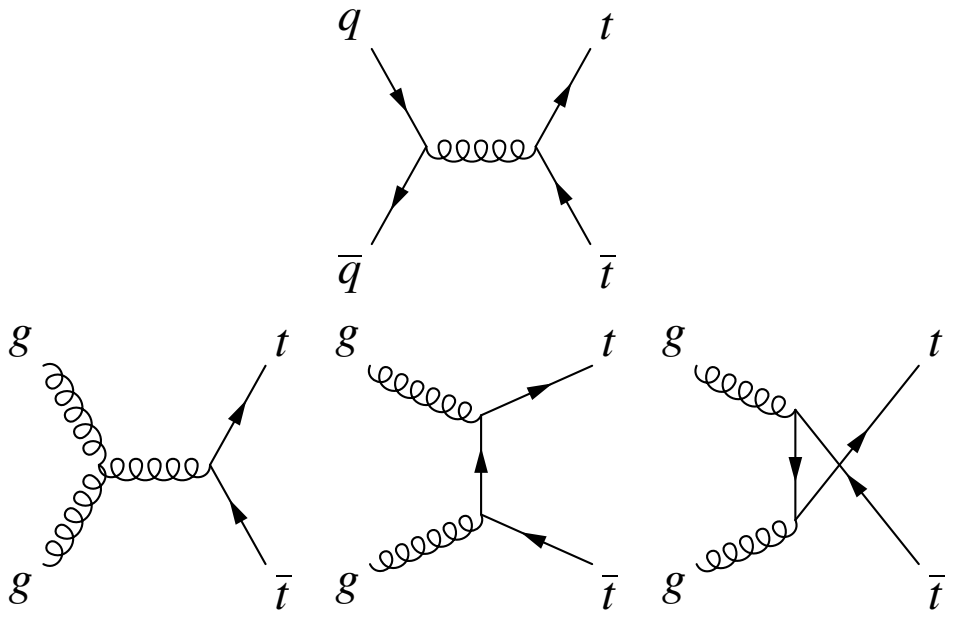

Figure 1.2: Four leading-order Feynman diagrams for top quark pair production at the Tevatron. Upper figure is the s–channel quark fusion process. Lower figures, starting from left, are the s–channel, t–channel, and u–channel gluon fusion processes, respectively.

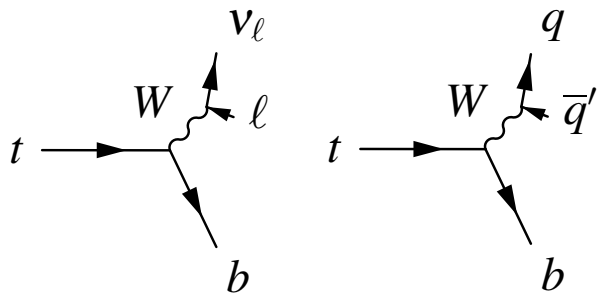

Figure 1.3: Feynman diagrams for leptonic and hadronic decay mode of top quark.

toward the total cross-section. The theoretical prediction at next-to-leading order for $p\bar{p} \to t\bar{t}$ cross-section at $\sqrt{s} = 1.96$ TeV is about 6.8 ± 0.8 pb [4, 5]. DØ's most precise measurement of the $t\bar{t}$ cross-section is

$$\sigma_{p\bar{p}\to t\bar{t}} = 8.3^{+0.6}_{-0.5}\ (\text{stat})\ ^{+0.9}_{-1.0}\ (\text{syst})\ \pm 0.5\ (\text{lumi})\ \text{pb}.$$

as reported in Ref. [6].

In the standard model, the top quark decays predominantly to a W boson plus a b quark as

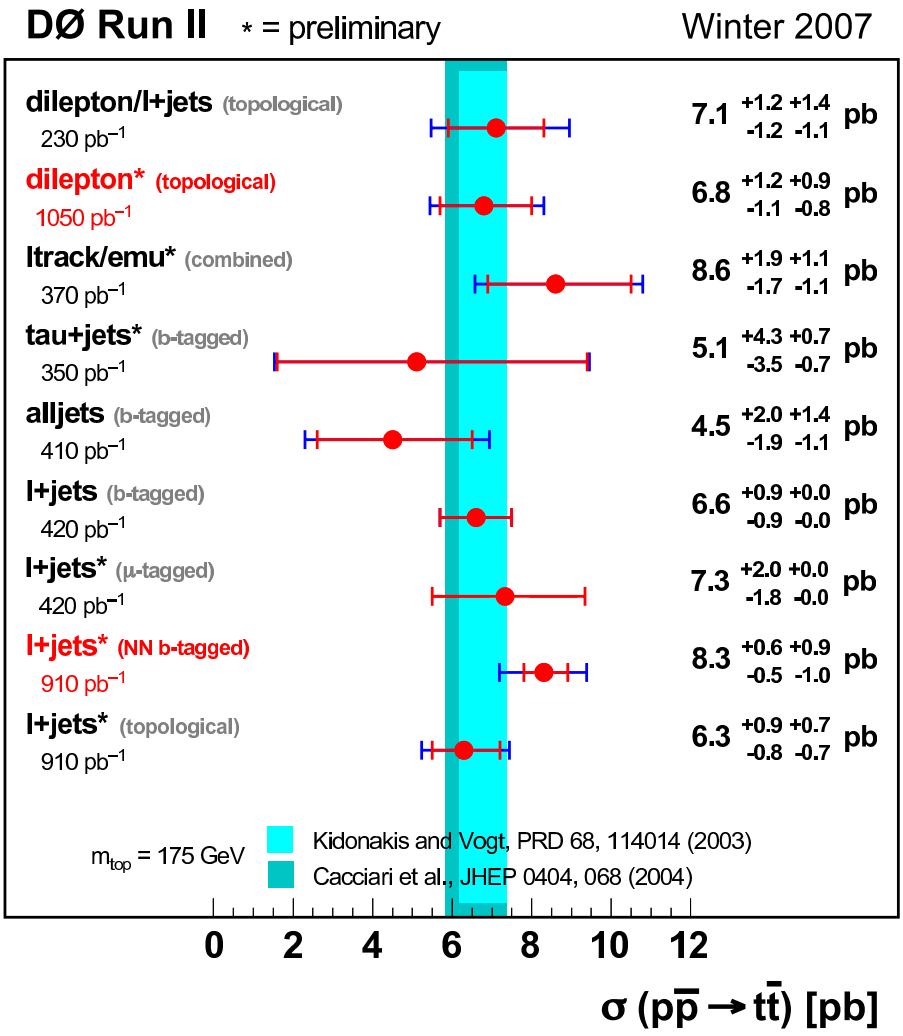

Figure 1.4: Summary of DØ measurements of $t\bar{t}$ cross-section at the Tevatron in various channels as of Winter 2007 [7].

displayed in Figure 1.3. Any other decay modes (if they exist) have not been observed. In the case of $t\bar{t}$ production, the decays of the two W bosons determine the final state. The W bosons can decay into either a charged lepton-neutrino pair ($e\nu_e$, $\mu\nu_\mu$, and $\tau\nu_\tau$), or quark-anti quark pair. The branching ratio (neglecting decay kinematics and CKM suppression) is $\frac{1}{9}$ for each lepton flavor, and $\frac{1}{3}$ for each qq' mode. Thus, for the case of $t\bar{t}$ one has

1. equal dilepton channel, where both W bosons decay to the same lepton flavor (ee, $\mu\mu$, $\tau\tau$), each channel with BR of $\frac{1}{81}$.

2. unequal dilepton channel, where the two W bosons decay to different lepton flavors ($e\mu$, $e\tau$, $\mu\tau$), each channel with BR of $\frac{2}{81}$.

3. lepton+jets channels, where one W boson decays into a lepton-neutrino pair, and the other W boson decays to a quark-antiquark pair (e + jets, μ + jets, and τ + jets), each channel with BR of $\frac{4}{27}$.

4. all jets channel where both W bosons decay into qq' final states, with BR $\frac{4}{9}$.

Measurement of $t\bar{t}$ cross-section has been performed by DØ in several dilepton channels (ee, $\mu\mu$, $e\mu$) [8, 9], lepton+jets channels (e+jets, μ+jets, τ+jets) [10–13], and the all hadronic channel [14]. Figure 1.4 shows a comparison of DØ results on $t\bar{t}$ cross-section measurements in the different channels as of Winter 2007. All measurements are done with the assumptions of top mass $m_t = 175$ GeV and standard model decay of top quarks. It can be seen that most of the experimental effort to study top quark events have been focusing on channels involving electrons, muons, and jets only. The tau sector in top decay has lagged behind the other channels.

1.3 The Tau Lepton

The tau lepton was discovered in 1975 at the Stanford Linear Accelerator Center [15]. Physicists from the MARK I Collaboration observed events in e^+e^- collisions whose final states have two leptons with different flavor

$$e^+e^- \rightarrow e^{\pm}\mu^{\mp} + 2 \text{ or more undetected particles.}$$

The explanation for those events is production of a new lepton pair, $\tau^+\tau^-$, which later decays into e/μ and neutrinos.

The tau has properties similar to the two lighter leptons, electron and muon, except for mass, and lifetime. Its mass is 1.77 GeV/c^2, heavier even than a proton, roughly an order of magnitude heavier than the muon, and three orders of magnitude heavier than the electron. Conservation of lepton number means that tau can only decays through charged-current weak interaction via emission of a virtual W boson. It can decays into leptonic final states ($e\nu_e\nu_\tau$ and $\mu\nu_\mu\nu_\tau$) or hadronic final states (charged and neutral mesons). The lifetime of the tau lepton is extremely short, 2.9×10^{-13} seconds, with $c\tau = 87$ μm.

This analysis will focus on the hadronic decay modes of tau leptons. Figure 1.5 shows tree-level Feynman diagrams for the leptonic and the two dominant hadronic decay modes of the tau.

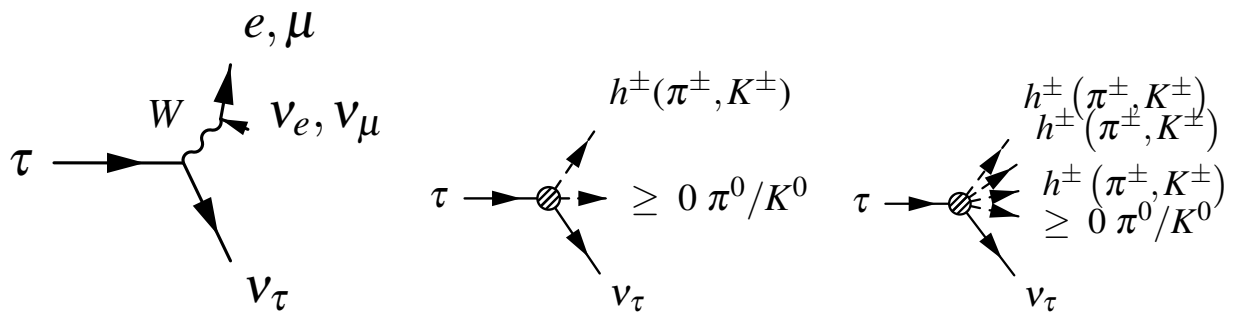

Figure 1.5: Illustrations for tau leptonic decay (left), tau hadronic one-prong decay (middle), and tau hadronic three-prong decay (right). Here h is a charged hadrons (mostly charged pions), and neutrals are either neutral pions or photons.

The decay modes into one charged hadron are also known as "one-prong" decays, while the decay modes into three charged hadrons are known as "three-prong" decays. The hadrons in tau decay are strongly dominated by pions. In more than 60% cases of all hadronic decays, one or more neutral pion which decays into two photons appear(s) in the final states. In almost all cases, tau hadronic decays will appear as narrow jets, sometimes accompanied with electromagnetic showers.

1.4 Research Motivations and Objectives

Analyses of dilepton modes of top quark production/decay benefit from relatively small backgrounds but suffer from small branching ratios. By including hadronic taus explicitly in $t\bar{t}$ analyses, two goals are achieved at once. The first goal is improvement of $t\bar{t}$ dilepton analyses by the addition of a final state which was not feasible before. This analysis will improve the statistics for dilepton analyses by adding one of the remaining three channels. The combination of this channel and the electron+tau channel is one of the larger dilepton samples. The second goal is to extend the sensitivity of $t\bar{t}$ analysis to include aspects to which muon or electron identification is not sensitive, but tau identification is.

1.4.1 Historical overview.

Prior to this work, all searches for top quark decays into the muon/electron+hadronic tau decay channel have been done by CDF. The first used approximately 110 pb^{-1} of Run I data [16]. A second search involved about 200 pb^{-1} Run II data [17]. Finally, two searches were done using about 350 pb^{-1} Run II data: one looking for new phenomena [18] and another for top quark pair

production [19].

In Run II, DØ performed an analysis using approximately 350 pb^{-1} of data to measure the top quark production cross-section in the τ + jets channel [13]. The measured value is

$$\sigma_{p\bar{p}\to t\bar{t}} = 5.1^{+4.3}_{-3.5}\ (\text{stat})^{+0.7}_{-0.7}(\text{syst}) \pm 0.3(\text{lumi})\ \ \text{pb}.$$

This value is the first DØ result using top quark decay to a tau lepton. This work presented here will complement the τ+jets results by including the $\mu + \tau$ channel.

1.4.2 The importance of top decays to tau lepton.

The decay of top quarks into tau lepton, $t \to \tau\nu_\tau b$ is a pure third generation decay. As such, this decay is a unique probe to new physics, which alters the top quark decay modes into states that favor subsequent decay to taus rather than other standard model particles.

A well-known candidate for new physics in $t \to \tau X$ decay is the existence of charged Higgs boson, with mass $m_{\rm H} < m_t - m_b$ [20]. If such a particle exists, the top quark could decay into a charged Higgs plus a b quark ($t \to Hb$) in addition to the known W boson plus b quark. The charged Higgs is expected to decay preferentially into a tau, which is the heaviest lepton.

$$t \to H^{\pm} b \to \tau\nu_\tau b \tag{1.1}$$

In some theories beyond the minimal Higgs sector of the standard model, the top quark decay to $H^{\pm}b$ is even more favored than the SM decay into Wb. A precise measurement of top quark pair production cross section in decay channels involving hadronic taus will provide a way to test such theories.

1.5 Overview of the analysis' approach

From the viewpoint of the physical processes that contribute to the final states, this analysis has the characteristics of $t\bar{t}$ dilepton analyses such as:

1. Small branching ratio from $t\bar{t}$ initial state.
2. The presence of two leptons with opposite-sign charges.
3. The presence of large missing transverse energy which is strongly correlated with the two leptons due to the presence of two or more neutrinos.

However, hadronic taus have a similar signature to jets, and can be faked by jets. Therefore, this analysis also has the characteristics of a $t\bar{t}$ muon+jets analysis. This dual feature of $t\bar{t}$ muon+tau analysis is crucial in forming the analysis strategy. Many aspects of the analysis from triggering, the choices of data sets, background composition and estimation, have been strongly influenced by $t\bar{t}$ dilepton and muon+jets analyses.

There are two primary categories of backgrounds to be considered. The first type comprises events with a real isolated muon and a real isolated hadronic tau. The primary source of this background is the Drell-Yan process $Z/\gamma^* \rightarrow \tau^-\tau^+ +$ jets with final states in which one of the taus decays to a muon, and the other tau decays hadronically. Since tau decays produce one or more neutrinos, Drell-Yan $Z/\gamma^* \rightarrow \tau\tau +$ jets will have real missing transverse energy. Other significant SM processes with a similar signature are the diboson (WW, WZ, and ZZ) events in which the bosons decay into two or more leptons with taus included.

The second background category has an object which is misidentified as an isolated hadronic tau. This misidentified object can be an electron, a muon, or a jet. There are two primary sources of this type of background. The first source is the process $Z/\gamma^* \rightarrow \mu^-\mu^+ +$ jets. The second source involves a jet falsely reconstructed as a tau lepton. Multijet events and production of W bosons with jets are examples. While the efficiency of jets to pass the tau identification algorithm is small, the large cross-sections make this background non-negligible.

This analysis selects events with one isolated high-p_T muon, one isolated hadronic tau, large missing transverse energy, and two high-p_T jets. Because this leaves large multijet, W and Z/DY backgrounds, this analysis applies $b-$tagging to take advantage of the heavy quark content of the top decays relative to the much smaller heavy quark content of the background.

After applying $b-$tagging, the sample is dominated by top quark events. These events are a mixture of $\mu + \tau_h + 2\nu + 2b$, other dilepton and $\mu/e +$ jets events, where τ_h is a tau lepton which decays hadronically. A two staged analysis is performed.

1. First, the top production cross-section is measured using all available top events. This result can be combined with other measurements by accounting for any overlap between samples.

2. Second, the cross-section $\times$ branching ratio for the specific final states, $t\bar{t} \rightarrow \mu + \tau_h + 2\nu + 2b$, is measured as a step toward tests of universality and searches for a charged Higgs boson.

Figure 1.6 shows a flow diagram of the analysis strategy. We select a muon+jets sample that is enriched in W+jets events. At this stage, we normalize the W+jets background, which is one

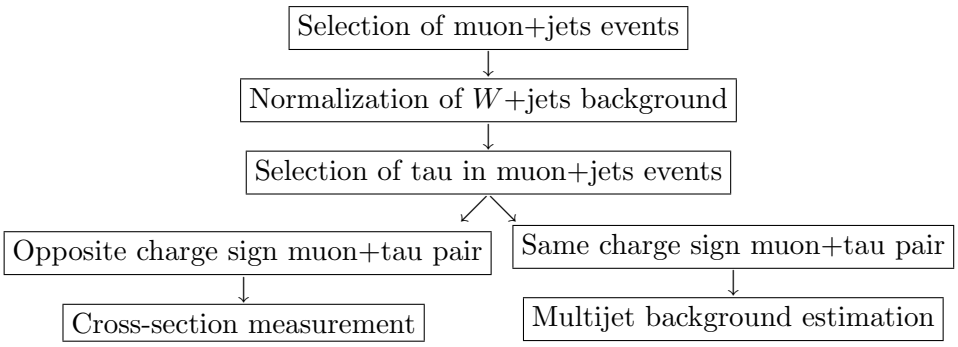

Figure 1.6: The strategy adapted by this analysis.

of the major background. The, we proceed to select a tau in the muon+jets sample, effectively selecting a muon+tau+jets sample. We then divide the muon+tau+jets sample into two disjoint samples. The first sample contains lepton-tau pairs with opposite charge sign (OS). This sample contains the signal events, and the cross-section measurement will be done using this sample. The second sample contains the muon-tau pairs with same-sign charge (SS). This sample will be used to estimate multijet background in the OS sample.

1.6 Convention

Throughout this document, the following terms are used:

τ_h: A τ lepton which decays to hadron(s) and a tau neutrino.

τ_e: A τ lepton which decays to an electron, an electron neutrino, and a tau neutrino.

τ_μ: A τ lepton which decays to a muon, a muon neutrino, and a tau neutrino.

To aid in understanding of how this analysis is different from, and how it is related to, the other $t\bar{t}$ analyses, the meaning of a particular $t\bar{t}$ final state is redefined in terms of *the set of final objects* which are actually seen by the detector. For example, the decay $W \to \tau\nu_\tau \to e(\mu)\nu_{e(\mu)}\nu_\tau$ is assigned to the observable final state $e(\mu)$. Table 1.1 lists the W branching ratio after combination of the decay $W \to e(\mu)\nu_{e\mu}$ with the decay $W \to \tau\nu_\tau \to e(\mu)\nu_{e(\mu)}\nu_\tau$, where the values of W and τ branching ratios have been taken from the 2006 Particle Data Book [21].

With the observed final states of W boson decays as given in Table 1.1, one can compute the branching ratio into observed final states of $t\bar{t}$ decays, with the assumption that the top quark decays predominantly into a W boson and a b quark (Table 1.2).

Table 1.1: The branching ratio of W boson with adjustment to the observed final state objects..

Observable W decay	Branching ratio
BR (e) = BR $(W \to e\nu_e)$ + BR $(W \to \tau\nu_\tau \to e\nu_e\nu_\tau\nu_\tau)$	0.1276
BR (μ) = BR $(W \to \mu\nu_\mu)$ + BR $(W \to \tau\nu_\tau \to \mu\nu_\mu\nu_\tau\nu_\tau)$	0.1252
BR (τ_h) = BR $(W \to \tau\nu_\tau)$ × BR $(\tau \to \text{hadrons} + \nu_\tau)$	0.0729
BR (qq')	0.6743

Table 1.2: Branching ratios for various $t\bar{t}$ final states, adjusted to the observed final state objects.

Decay modes		Value
BR $(t\bar{t} \to ee)$	BR (e) × BR (e)	0.01628
BR $(t\bar{t} \to e\mu)$	2 × BR (e) × BR (μ)	0.03195
BR $(t\bar{t} \to e\tau_h)$	2 × BR (e) × BR (τ_h)	0.01860
BR $(t\bar{t} \to \mu\mu)$	BR (μ) × BR (μ)	0.01568
BR $(t\bar{t} \to \mu\tau_h)$	2 × BR (μ) × BR (τ_h)	0.01825
BR $(t\bar{t} \to \tau_h\tau_h)$	BR (τ_h) × BR (τ_h)	0.00531
BR $(t\bar{t} \to \ell\ell), (\ell \in \{e, \mu, \tau\})$	BR (ℓ) × BR (ℓ)	0.10608
BR $(t\bar{t} \to e + \text{jets})$	2 × BR (e) × BR (qq')	0.17208
BR $(t\bar{t} \to \mu + \text{jets})$	2 × BR (μ) × BR (qq')	0.16884
BR $(t\bar{t} \to \tau_h + \text{jets})$	2 × BR (τ_h) × BR (qq')	0.09831
BR $(t\bar{t} \to \ell + \text{jets}), (\ell \in \{e, \mu, \tau\})$	2 × BR (ℓ) × BR (qq')	0.43924
BR $(t\bar{t} \to \text{alljets})$	BR (qq') × BR (qq')	0.45468

Finally, the shorthand $\mu\tau$ will be used when referring to the channel $t\bar{t} \to \mu + \tau_h + \nu_\mu\nu_\tau + b\bar{b}$.

CHAPTER 2

EXPERIMENTAL APPARATUS

The work presented in this dissertation was done utilizing two major experimental facilities in high energy physics. The first is the Tevatron accelerator which provides beams of high energy particles. The second is the DØ detector which provides a means to study results of collision of high energy particle beams from the Tevatron. Both are located at Fermi National Accelerator Laboratory in Batavia, Illinois.

2.1 The Tevatron Accelerator

The Tevatron is a storage ring that collides high-energy proton and antiproton beams. Each beam has an energy of 980 TeV, making the total center-of-momentum (c.m.) energy in the collision processes to be 1.96 TeV. Tevatron has a diameter of approximately 2 km. Figure 2.1 shows an aerial picture of the Tevatron and other accelerators at Fermilab. Viewed from above, the proton beam circulates in the clockwise direction, while antiproton beam circulates in the counter-clockwise direction. There are six designated points on the Tevatron where the beams are made to cross with each other. At two of those six points, named **B0** and **D0**, the beams are made to collide with each other. The DØ detector is located at the **D0** collision point, hence the origin of the name.

The Tevatron operates by circulating bunches of particles instead of continuous beams. There are 36 bunches each of protons and antiprotons. At the two mentioned collision points, crossings of protons and antiprotons bunches happen every 396 ns. Typical values of instantaneous luminosity ($\mathcal{L}$) delivered by the Tevatron are $10^{31} - 10^{32}$ cm^{-2} sec^{-1}.

The amount of data recorded by the DØ detector is expressed in units of luminosity integrated over time (cm^{-2}). A convenient way to express this unit is to convert it into another unit which has the dimension of inverse area. Commonly accepted units are pb^{-1} (10^{36} cm^{-2}) or fb^{-1} (10^{39} cm^{-2} = 1000 pb^{-1}.)

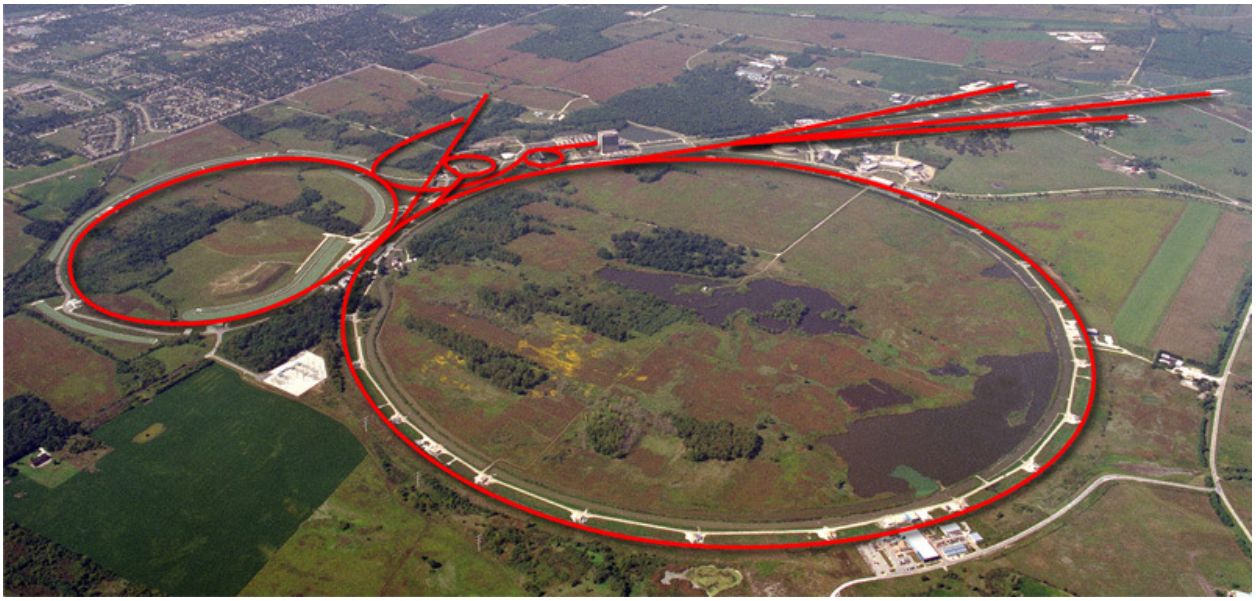

Figure 2.1: An aerial view of Fermilab, looking in the northwestward direction. The red lines show the schematic of the accelerator complex. Tevatron is the largest circle in the foreground. DØ detector is located at the building complex near the lower-right corner.

2.2 The DØ Detector

The DØ detector is a general purpose particle detector designed to study hard scattering processes in proton-antiproton collisions at the TeV energy scale. The detector has three principal subsystems: central tracking detectors, a hermetic uranium/liquid argon calorimeter, and muon spectrometer. Figure 2.2 shows a side view of the detector. An exhaustive description of the DØ detector is available [22].

A right-handed coordinate system is used to describe the detector and physics events. The $z-$axis is directed along the direction of the proton beam, and the $y-$axis is directed upward. The polar angle θ is the angle between a vector from the origin and the positive $z-$axis. In addition, it is convenient to define the two quantities *pseudorapidity* and *transverse momentum*. The pseudorapidity is defined as:

$$\eta = -\ln\left(\tan\left(\frac{\theta}{2}\right)\right) \tag{2.1}$$

which approximates the true rapidity y,

$$\eta = \frac{1}{2}\ln\left(\frac{E + p_z c}{E - p_z c}\right) \tag{2.2}$$

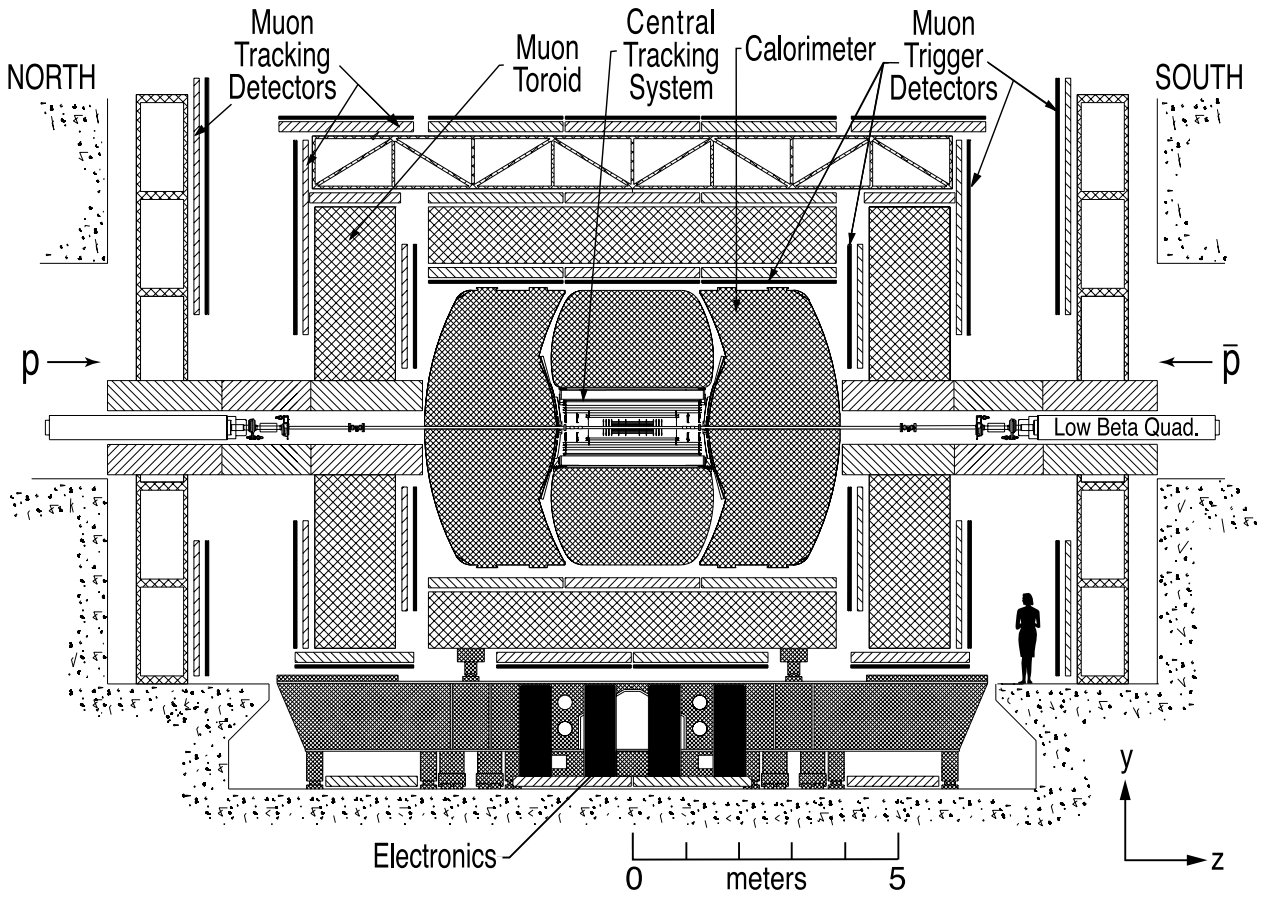

Figure 2.2: A side view of the DØ detector as seen from the West side of the detector.

in the massless approximation, $(mc^2/E) \to 0$. The region which has a large value of $|\eta|$ is called "forward". The transverse momentum (p_T) is defined as the component of momentum projected onto a plane perpendicular to the beam axis.

$$p_T = p \sin\theta \tag{2.3}$$

Two choices of the coordinate system's origin are used: the reconstructed primary vertex of $p\bar{p}$ interaction and the center of the detector. The first one is referred as the physics coordinate, and the second one is referred as detector coordinate.

2.3 Central Tracking Detector

The central tracking detector consists of the silicon microstrip tracker (SMT), the central fiber tracker (CFT), a solenoidal magnet, and the preshower detector. Figure 2.3 shows the central

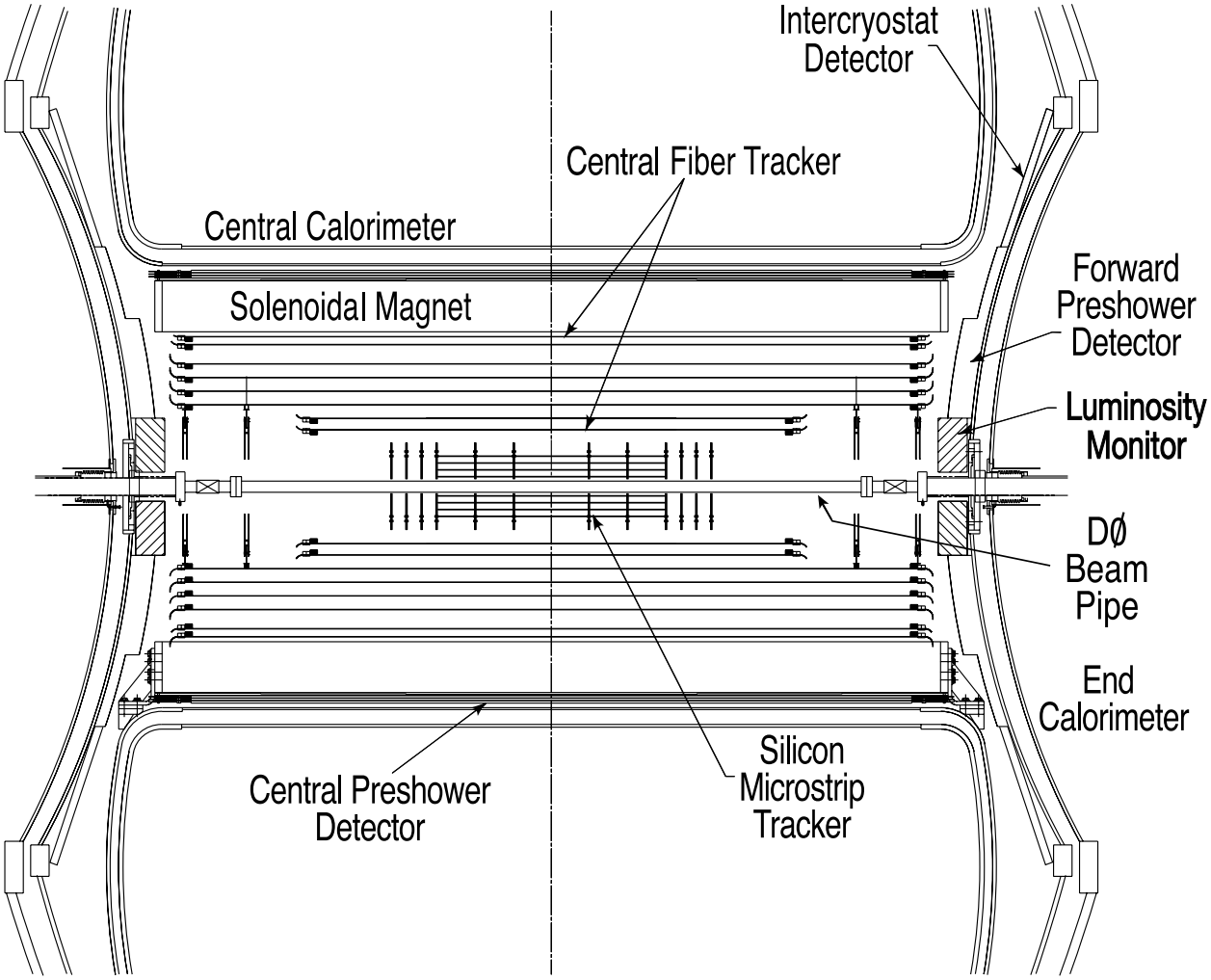

Figure 2.3: The central tracking region of the DØ detector.

tracking system of DØ detector. The SMT and CFT are located within a cylindrical volume inside the magnet with approximate length of 2.5 m and radius of 50 cm. The solenoidal magnet generates a nearly uniform magnetic field along the $z-$direction with a strength of 2 T. Together, the central tracking detectors allow reconstruction of charged particle tracks and independent measurement of their momenta, precise determination of the primary vertex, and reconstruction of secondary vertices to identify heavy quark jets.

The SMT consists of silicon detectors in the form of barrel modules and disk modules. Figure 2.4 shows a three-dimensional rendering of the SMT detector. There are six barrel modules, each has four cylindrical layers of silicon detectors. The barrels are interspersed by the disk modules

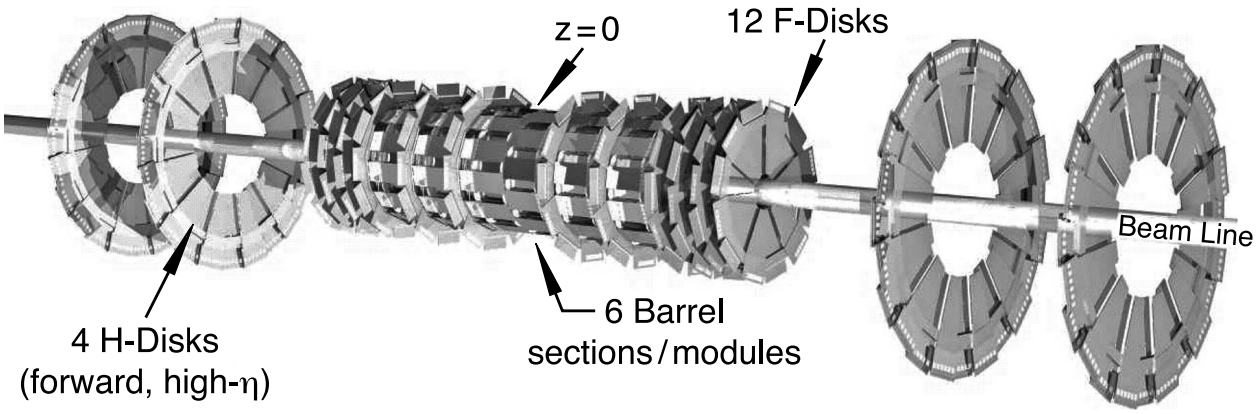

Figure 2.4: The DØ silicon microstrip tracker detector.

along the beam direction. Two larger disks are located further in the $z-$direction to cover the forward region. The barrel detectors provide positional measurement in the transverse plane, while the disk detectors provide measurement in the longitudinal direction as well as in the transverse plane. The radius of the smaller disk modules in the middle part is 10 cm, while the larger disk at the ends have a radius of 26 cm.

The CFT consists of sixteen layers of scintillating fibers which are mounted on eight cylindrical support structures. The innermost cylinder has a radius of approximately 20 cm while the outermost radius has a radius of approximately 50 cm. Each cylinder supports two doublet layers of scintillating fibers: one with the fibers oriented parallel with the beam (z), and one with the fibers oriented at a stereo angle of either $+3^\circ$ (u) or -3° (v). Starting from the innermost cylinder, the layers are arranged in the sequence: $zu - zv - zu - zv - zu - zv - zu - zv - zu - zv$. The scintillating fibers are connected optically to clear fiber waveguides which send the optical signal further to the readout electronics.

The solenoidal magnet provides almost uniform magnetic field of strength 2 T along the $z-$direction. The TOSCA [23] program is used to model the magnetic field map within the detector. A study with $J/\psi \to \mu^+\mu^-$ events shows that the the magnetic field map is accurate within 0.5% precision. The magnet operates at a temperature of 10 K and draws a current of approximately 4750 A.

The preshower detector has a role of both calorimeter and tracking detectors. It aids in the identification of electrons, photons, and pions from tau decays. The preshower detector is divided into two subsystems: central preshower detector (CPS) which covers the region up to $|\eta| < 1.3$ and

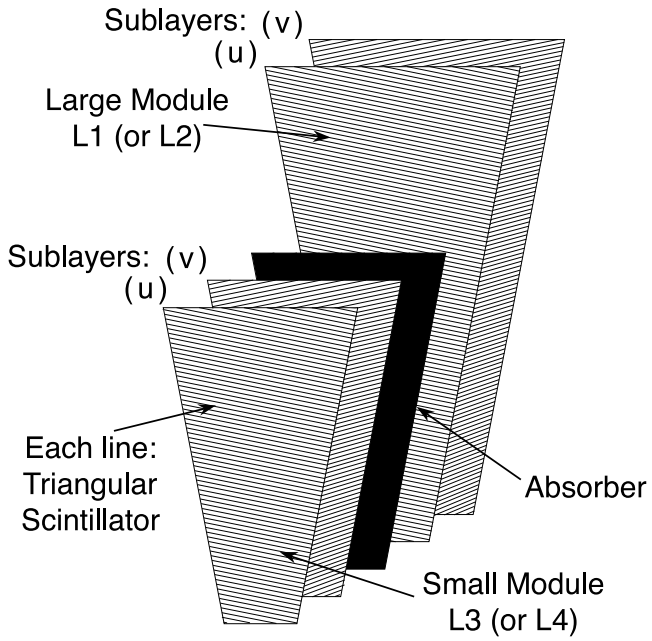

Figure 2.5: A complete ϕ segment of the forward preshower detector with the four layer of wedge-shaped detectors.

the forward preshowers detectors (FPS) which cover the region $1.5 < |\eta| < 2.5$.

The CPS is located between the solenoidal magnet and the central calorimeter module. It consists of three concentric, cylindrical layers of scintillating fibers. One layer has axial orientation, and two layers have stereo orientation of approximately $\pm 24°$. The FPS are attached to the faces of the endcap calorimeter modules. They have the form of disks built from wedge-shaped segments. Each segment has two layers of scintillating fibers with different orientation, separated by an angle of $22.5°$. Figure 2.5 shows a complete segment of the FPS detector.

2.4 Calorimeter and Inter-Cryostat Detector

The DØ calorimeter system is built from three uranium/liquid-argon, sampling calorimeters and inter-cryostat detector (ICD). The central calorimeter (CC) covers the region of detector $|\eta| < 1.0$, and the two endcap calorimeters (EC) cover the region $1.4 < |\eta| < 4.2$. The calorimeters operate at a temperature of 90 K and each of them is contained within its own cryostat. Between the central and the endcap calorimeters are the ICD detectors which are built from scintillating tile detectors. They provide readout in the region where the calorimeters have incomplete coverage.

The calorimeter is segmented into projective towers which have size of approximately 0.1×0.1

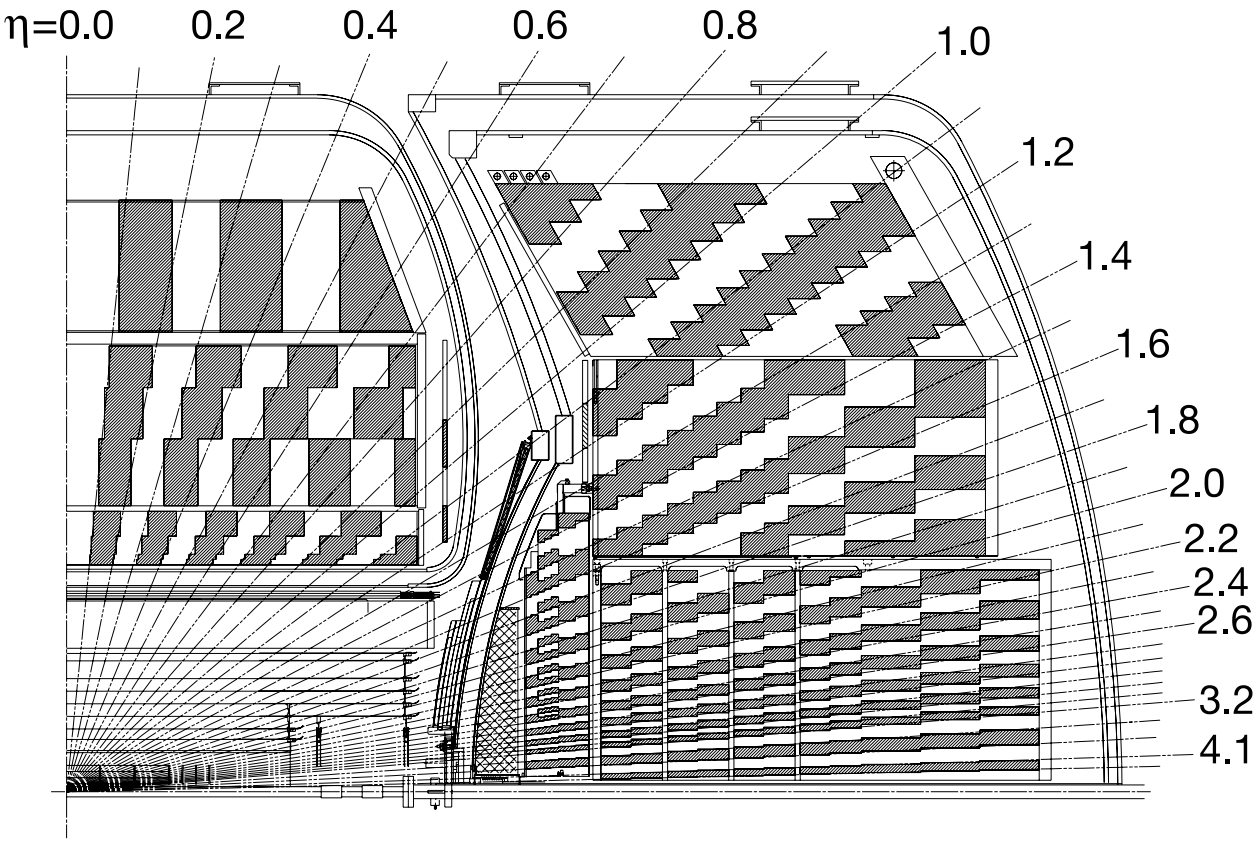

Figure 2.6: A side view of a quarter of the calorimeter, showing the segmentation of the calorimeter into cells and towers. The rays from the center of the detector are rays of contanst pseudorapidity.

in $\eta - \phi$ space. Figure 2.6 shows a side view of a quarter of the calorimeter, together with the rays which show the projective towers. In the radial outward direction, each tower is divided into cells which are grouped further into different type of layers. From inside to outside, the layers are: electromagnetic, fine hadronic, and coarse hadronic. Figure 2.7 shows a schematic view of a calorimeter cell.

Each type of layer uses a different design of absorber plate for its readout cells. The electromagnetic layers use thin plates (3-mm-thick in CC or 4-mm-thick in EC) made of nearly depleted uranium. The fine hadronic layers use 6-mm-thick plates made of uranium-niobium alloy in both CC and EC. The coarse hadronic layers use 46.5-mm-thick copper plates (in EC) or stainless steel plates (CC). Due to the presence of more material in the readout cells, the coarse hadronic

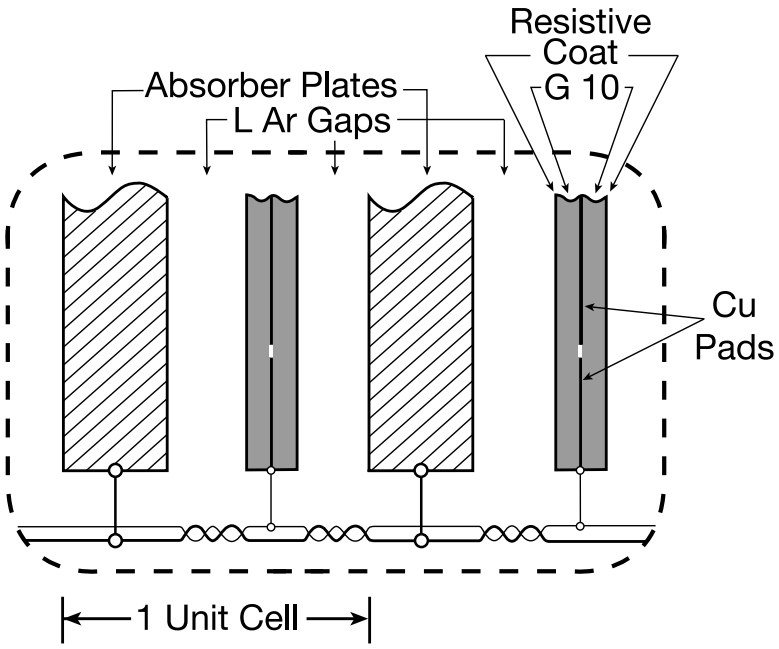

Figure 2.7: A schematic view of a calorimeter readout cell with its liquid argon gap and signal board.

layers have a much higher noise level compared to the electromagnetic and fine hadronic layers.

The electromagnetic layers play an important role in the reconstruction of electrons, photons, and taus. There are four layers of electromagnetic readout modules both in CC and EC. The EM layers cover the region up to $|\eta| < 2.5$, with a gap in the interval $1.1 < |\eta| < 1.5$, which corresponds to the region between CC and EC. Of particular importance is the third EM layer which has spatial resolution of 0.05×0.05, twice that of the other layers . This finer resolution aids in precise reconstruction of electrons, photons, and neutral pions from tau decays.

2.5 Muon Spectrometer

The muon spectrometer is divided into the central muon detector and two forward muon detectors. The central muon detector covers the region up to $|\eta| < 1.0$, while the forward muon detectors cover the region in the range $1.0 < |\eta| < 2.0$. There are two main components used to build the detectors: drift chambers and scintillation counters. The drift chambers provide spatial information, while the scintillation counters provide fast and precise timing measurement for triggering and positional measurement.

The central muon detector consists of proportional drift tubes (PDT), scintillation counters,

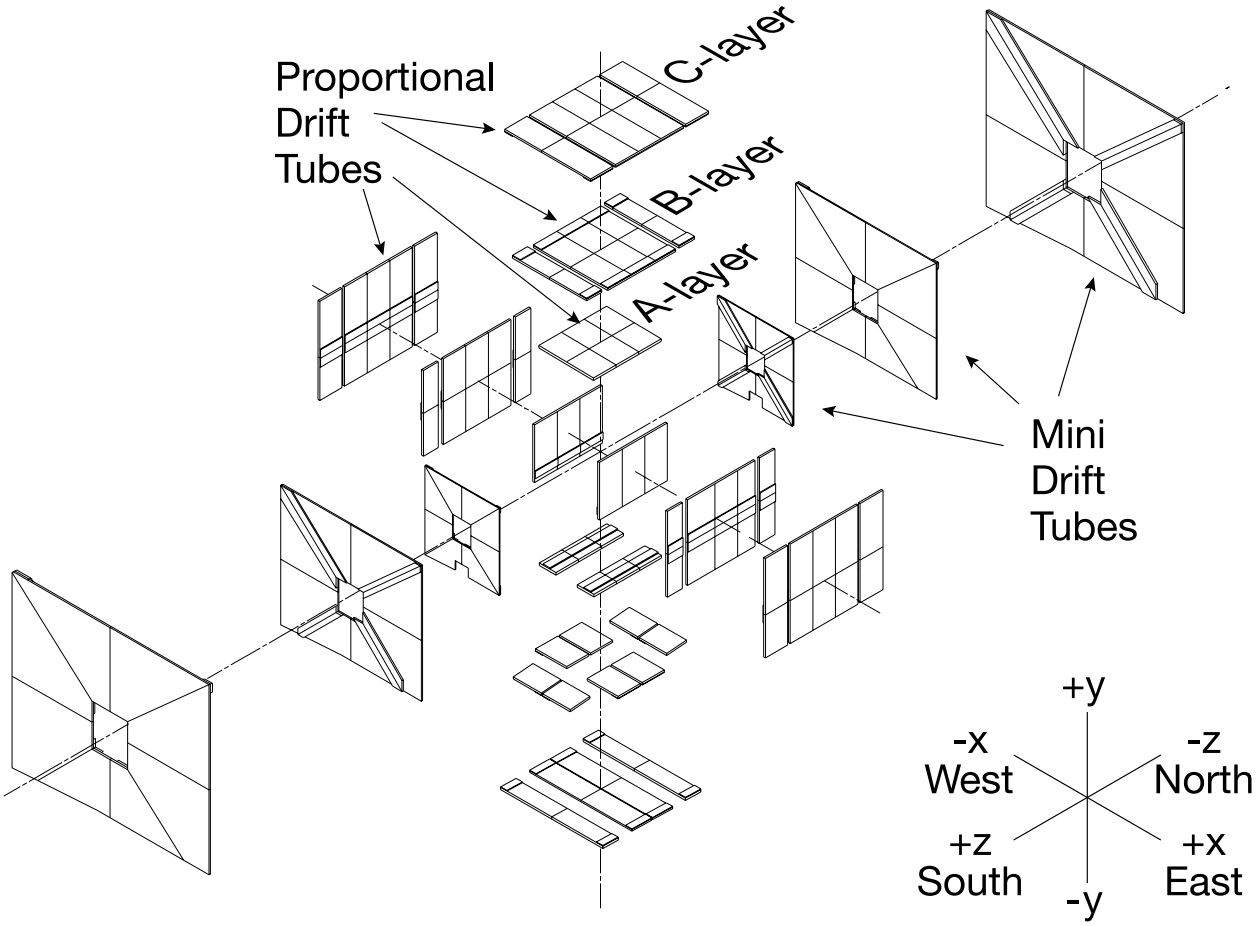

Figure 2.8: Exploded view of the muon drift chambers.

and a toroidal magnet. There are three layers of drift chambers, one is located within the magnet (A layer), and two outside (B and C layer). Two layers of scintillation counters are installed, one right inside the A layer and one right outside the C layer.

The forward muon detectors consist of mini drift tubes (MDT) and scintillation counters. They are arranged in three layers, each layer has both MDTs and scintillators. Similar to the central muon detectors, there is one layer inside the toroidal magnet and two layers outside the toroidal magnets.

Figure 2.8 and Figure 2.9 show the expanded views of the muon chambers and muon scintillators, respectively.

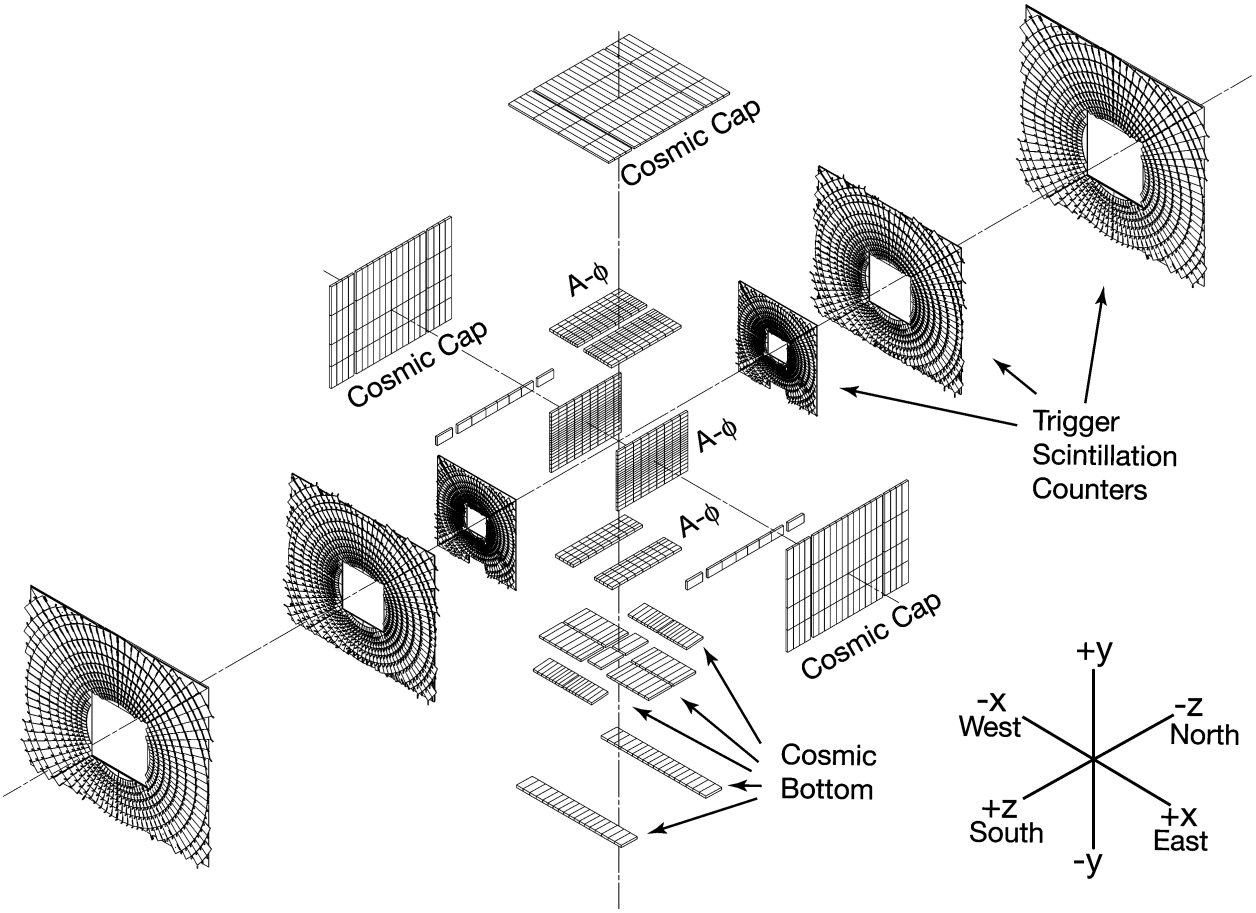

Figure 2.9: Exploded view of the muon scintillators.

2.6 Luminosity Monitor and Measurement

The luminosity detector is built of two arrays of 24 wedge-shaped scintillation counters and photomultiplier tube (PMT) attached into each wedge. They are located at the front of the endcap calorimeters, covering the pseudorapidity region $2.7 < |\eta| < 4.4$, as can be seen in Figure 2.3. A zoomed drawing, focusing on the luminosity monitor only, can be found in Figure 2.10.

The instantaneous luminosity of $p\bar{p}$ collisions in the DØ detector's interaction region is determined by measuring the counting rate of inelastic $p\bar{p}$ collisions,

$$\mathcal{L} = \frac{1}{\sigma_{\text{eff}}} \frac{dN}{dt} \tag{2.4}$$

where $\mathcal{L}$ is the instantaneous luminosity, σ_{eff} is the effective inelastic $p\bar{p}$ cross-section (taking into account geometrical acceptance and efficiency of the luminosity detector), and $\frac{dN}{dt}$ is the counting

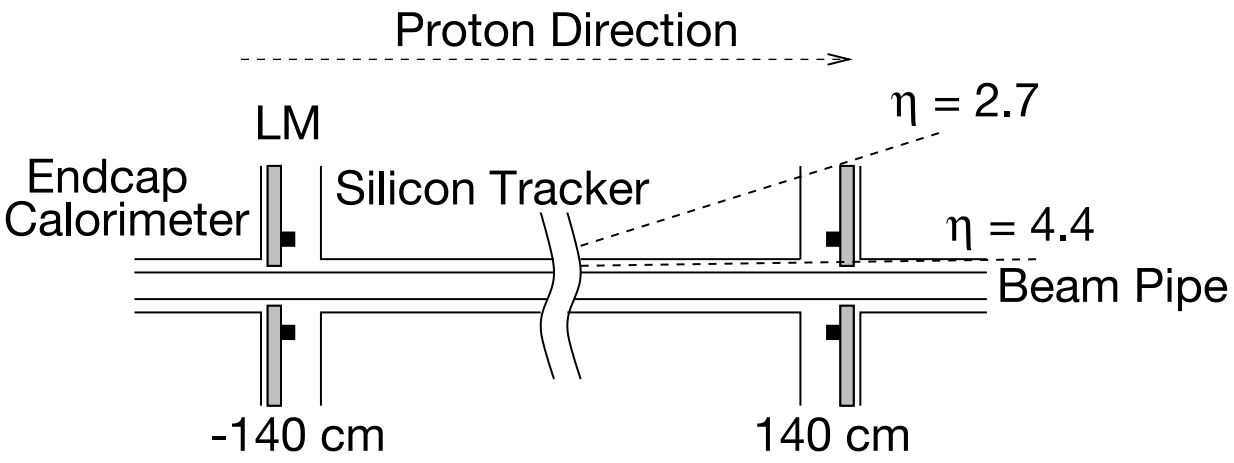

Figure 2.10: Schematic drawing of the luminosity detector and its location within the DØ detector.

rate measured by the detector. To eliminate background from beam halo, the origin of collisions must be within $|z| < 100.0$ cm. The origin of collisions is estimated from the time of flights recorded at the two sides of the luminosity counter.

In practice, the counting rate is determined by counting the fraction of beam crossing with no collisions recorded, and then use Poison statistics to determine $\frac{dN}{dt}$. This method is known as the *counting zeros* technique, and it ensures that multiple collisions are treated properly [24]. The measurement is done over a time period which is short enough to ensure that the instantaneous luminosity is constant throughout the period, and long enough to make the statistical uncertainty on the counting rate negligible. This time period is known as luminosity block. A unique number (luminosity block number) is assigned to each luminosity block. The calculation of total integrated luminosity for a given data is done by integrating the instantaneous luminosity over time, treating each luminosity block as a timeslice in the integration.

2.7 Trigger and Data Acquisition System

The DØ detector uses a three-level trigger system to reduce the number of readout events to approximately 50-100 Hz for recording to tape. Figure 2.11 shows an overview of the triggering and data acquisition system.

The first level (Level 1 or L1) takes input from the central tracking detector, calorimeter, and muon system. It has a maximum accept rate of 1800 Hz. The trigger looks for specific signatures

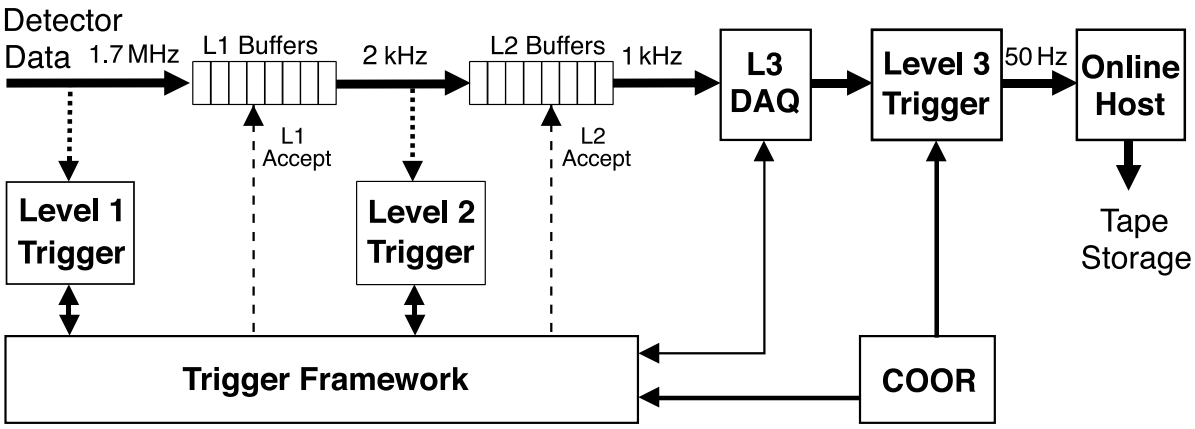

Figure 2.11: Schematic display of data flow in DØ trigger and data acquisition system.

such as:

- Hit patterns in the central tracking detector consistent with a charged particle above a certain p_T threshold.
- Energy depositions in the calorimeter above a certain energy threshold, either on the electromagnetic layers only, or on the full tower.
- Hits in the muon chambers and muon scintillators above a minimum number of hits.

Candidate events passing the L1 requirement are then sent to the the next level (Level 2 or L2).

The Level 2 trigger consists of subdetector-specific processing nodes, and a global node which tests for correlation between information across the subdetectors. The detector-specific nodes can perform simple reconstruction of physics objects using information only from their assigned subdetector. The L2 trigger is designed to have a maximum accept rate of 850 Hz.

Figure 2.12 shows the flow of information from various sub-detectors into the L1 and L2 trigger system.

The last level, Level 3 (L3), consists of two subsystems: The Level 3 Data Acquisition Cluster (L3 DAQ) and Level 3 filter. The L3 DAQ is an event builder which reads event information from all subdetectors and reconstructs complete physics objects in the event. Simplified versions of the reconstruction algorithms are used here as there is a time constraint during data taking. The event builder then sends information to the L3 filter which makes decisions using the complete

event information. The L3 filter applies more complicated selection criteria such as requirements of isolation, object-matching, or object-separation. The final output of the L3 trigger has a rate of approximately 50-100 Hz.

Events which pass all three trigger levels are written temporarily onto local disks on the online data-taking cluster. The data are later transferred into a robotic tape system for further post-recording reconstruction and processing.

It is convenient to define three kind of events that are recorded by the DØ detector:

- *Zero bias*: events which are recorded without any requirements on the trigger. The content of those events is dominated by readout electronics' noises and energy deposited by cosmic muons.

- *Minimum bias*: events which are recorded with a requirement that a proton-antiproton collision has happened in the detector. In addition to the content of zero bias events, they also contains energy coming from underlying events.

- *Data*: events which are recorded with requirements on the trigger and contain signatures of physics processes of interest.

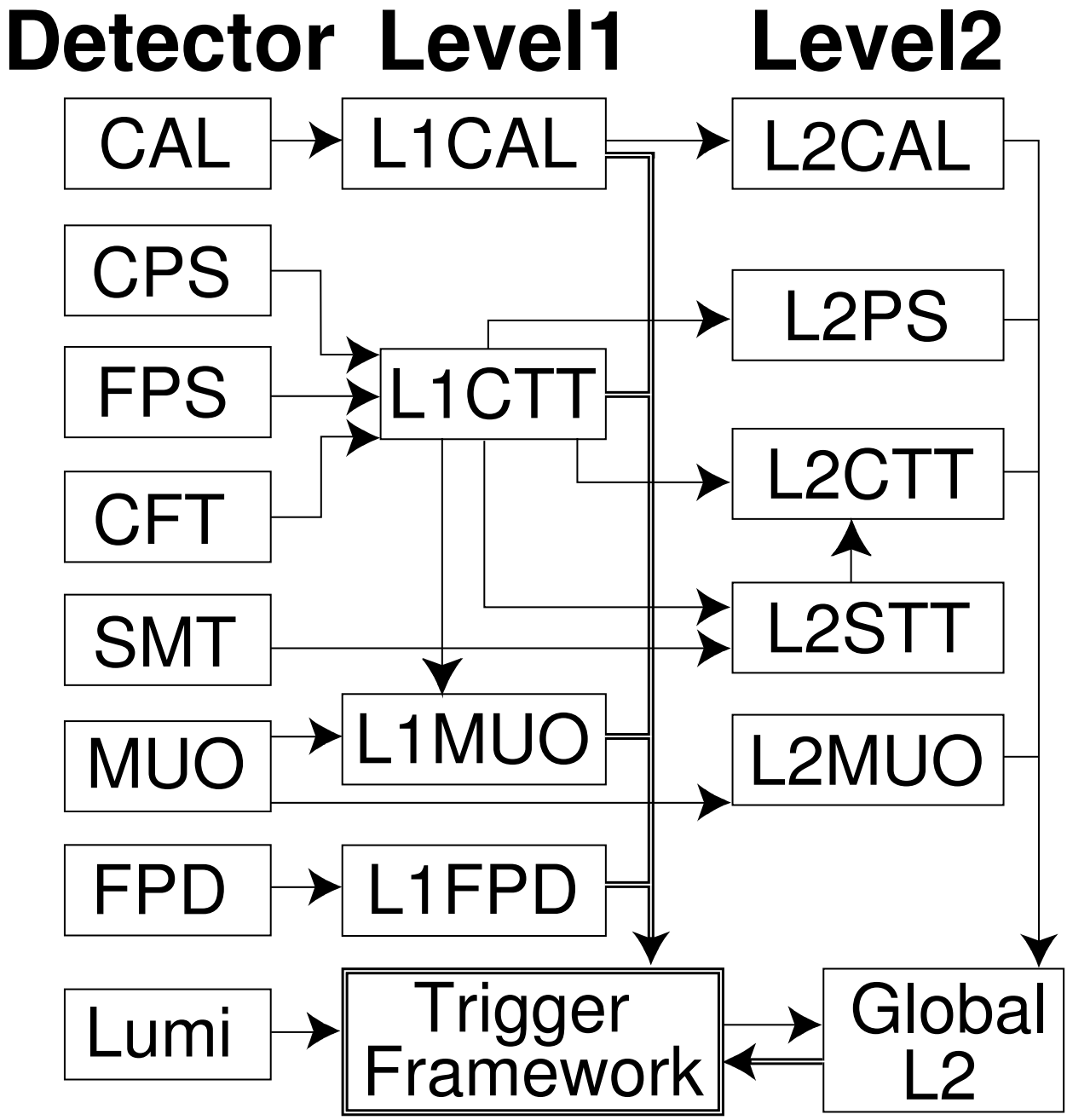

Figure 2.12: Flow diagrams of DØ Level 1 and Level 2 trigger systems, with the arrow lines show the flow of trigger information between subsystems.

CHAPTER 3

EVENT RECONSTRUCTION AND OBJECT IDENTIFICATION

The reconstruction process which converts raw data from the DØ detector proceeds in three steps:

1. Conversion of raw data into hits which correspond to position and energy measurement.

2. Reconstruction of basic physics objects: charged particle tracks in the tracking detector, clusters of energies in the calorimeters, and tracks in the muon system.

3. Combination of basic physics objects into final physics objects: electrons, photons, muons, taus, jets, and vertices.

This chapter describes the principal ideas of reconstruction algorithms for physics objects at DØ with the exception of taus, which require an in-depth treatment. Chapter 4 describes the reconstruction of taus in detail.

3.1 Charged Particle Track Reconstruction

Reconstruction of charged particle tracks uses information exclusively from the central tracking detectors. There are two steps in the reconstruction process: candidate track finding and track fitting.

In the first step, two methods are used to build a list of candidate tracks. The first one uses histograms to find patterns of particle trajectories among hit clusters in the tracking detector [25]. It is based on a Hough transformation which was originally used to find patterns in bubble chamber pictures [26]. The second one uses hit clusters in the SMT to form roads, onto which hits in additional tracking detector layers are added [27].

In the second step, the list of candidate tracks from the first step are passed to a track fitter [28] which uses the Kálmán filter algorithm [29]. At the core of the track fitting algorithm is the

DØ interacting propagator [30], which is a generic black box algorithm that propagates a track in the DØ tracking system, taking into account the DØ solenoid's magnetic field and interaction of charged particles with detector material. For each candidate track, the algorithm incrementally adds hit clusters associated with the candidate track into the fit and recalculates the optimal track parameters. This step is repeated until all hit cluster information has been used.

3.2 Primary Vertex Reconstruction

The primary vertex is the origin of tracks from hard scattering processes in $p\bar{p}$ collisions. The algorithm's goal is to separate the primary vertex from vertices produced in minimum-bias interactions and decays of long-lived particles. There are three steps in the primary vertex reconstruction algorithm: track clustering and selection, vertex fitting, and vertex selection [31].

In the first step, tracks are clustered along the $z-$direction. The clustering algorithm begins with the track which has the highest p_T and adds tracks to the cluster if the $z-$distance between the track and the cluster is less than 2 cm. Tracks are required to have $p_T > 0.5$ GeV, at least two (zero) SMT hits if they are inside (outside) the SMT geometrical acceptance region. At the end of this step is a list of candidate vertices which may contain the hard scatter primary vertex and additional vertices from minimum bias interactions and decay of long-lived particles.

In the second step, a two-pass algorithm is used for each $z-$cluster to fit the clustered tracks to a common vertex. In the first pass, a tear-down Kálmán vertex fitter fits all tracks into a common vertex, and removes the track which contributes the largest χ^2 into the fit. The fit is repeated until the total χ^2/n.d.o.f. of the fit is less than 10.

In the second pass, the tracks in each $z-$cluster are first sorted in order of their distance of closest approach (DCA) in the $x-y$ plane to the beam spot, using beam-spot information determined in the first pass. Only tracks which have significance (defined as $|DCA|/\sigma_{DCA}$) less than 5.0 are selected. The selected tracks are then fitted to a common vertex with an adaptive Kálmán vertex fitter. The fitter weighs the χ^2 contribution of each track by a Fermi function,

$$w_i = \frac{1}{1 + e^{(\chi_i^2 - \chi_c^2)/2T}} \tag{3.1}$$

where χ_i^2 is the χ^2 contribution of the track to the vertex fit, χ_c^2 is the cutoff value, and T is a parameter which determines the sharpness of the function [31].

In the last step, a probabilistic method is used to determine the primary vertex. The method computes the probability of a vertex to be a minimum bias vertex by using the vertex track p_T

distribution. The vertex which has the smallest probability to be a minimum bias vertex is selected as the primary vertex [32].

3.3 Muon Reconstruction

Muons are identified by using hit information in the muon system and tracks reconstructed by the central tracking detector [33]. The algorithm begins by combining scintillator and wire chamber hits into trajectories in the muon system (called *local muons*) which are consistent with muons coming from the interaction region. Reconstructed local muons are then matched with tracks in the tracking detector. Here it is necessary to propagate tracks from the central tracking detector to the muon system [34]. The final reconstructed, track-matched muons use the tracks' information to obtain the muons' charge and momenta.

In this analysis, two definitions of muon are used, one is a subset of the other one.

- **Loose muon**

  1. The muon is required to have wire and scintillator hits inside and outside the muon toroid.
  2. Muon is required to have scintillator hit times to be less than 10 ns from the time a bunch crossing happens. This cut helps to to reject cosmic muons.
  3. The muon must be matched to a track in the central tracking detector. The track is required to have a good fit with $\chi^2/n.d.o.f. < 4.0$ and the distance of closest approach ($|DCA|$) to the primary vertex to be less than 0.2 cm for tracks without hits in the silicon detector. For tracks which have hits in the silicon detector, the DCA requirement is tightened to $|DCA| < 0.02$ cm.
  4. The muon is separated from jets which have p_T at least 15.0 GeV by $\Delta R > 0.5$ in $\eta - \phi$ space. This condition is called loose isolation condition.

- **Tight muon**

  Tight muons are required to fulfill the loose muon requirements and the tight isolation conditions. The conditions for a tight isolation are:

  1. The sum of calorimeter transverse energy in an annular cone with inner radius 0.1 and outer radius 0.4 around the muon direction must be less than 15% of the muon transverse

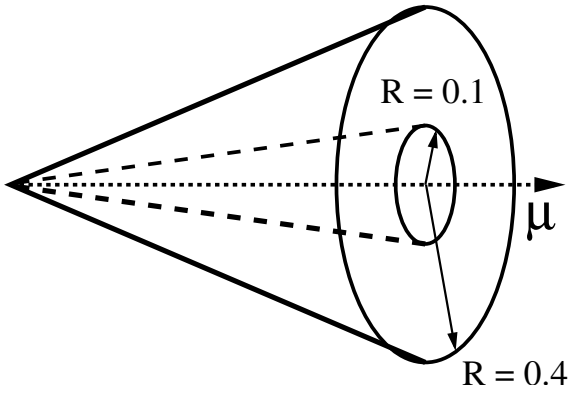

Figure 3.1: Hollow cone used in defining muon calorimeter isolation variable.

momentum,

$$\left| \frac{\sum^{\text{cells}} E_T}{p_T^{\mu}} \right| < 0.15, \tag{3.2}$$

The sum is performed over all calorimeter cells within the cone with the exception of cells within the coarse hadronic layers. Figure 3.1 shows the definition of hollow cone used in calculating the muon calorimeter isolation.

2. The momentum sum of all tracks (excluding the muon track) in a cone of radius 0.5 (in $\eta - \phi$ space) around the muon direction, must be less than 15 % of the muon transverse momentum.

$$\left| \frac{\sum^{\text{tracks}} p_T}{p_T^{\mu}} \right| < 0.15, \tag{3.3}$$

In Monte Carlo events, the efficiency to reconstruct a muon is corrected to simulate the efficiency in data. For each reconstructed muon in the event, a correction factor is multiplied to the event's weight. An exhaustive table of the correction factor as function of muon kinematics is determined by using the tag-and-probe method in dimuon data sample and in $Z \to \mu^+\mu^-$ Monte Carlo sample. The correction factor is broken down into correction for muon detector hits reconstruction, muon track reconstruction, and muon isolation in the tracking detector and calorimeter.

Figure 3.2 to Figure 3.4 shows distributions of efficiency corrections factors for muon reconstruction, broken down into the three different corrections mentioned earlier. The average correction values in top signal Monte Carlo for muon hit reconstruction, muon track reconstruction, and muon isolation are 0.98, 0.92, and 1.01, respectively.

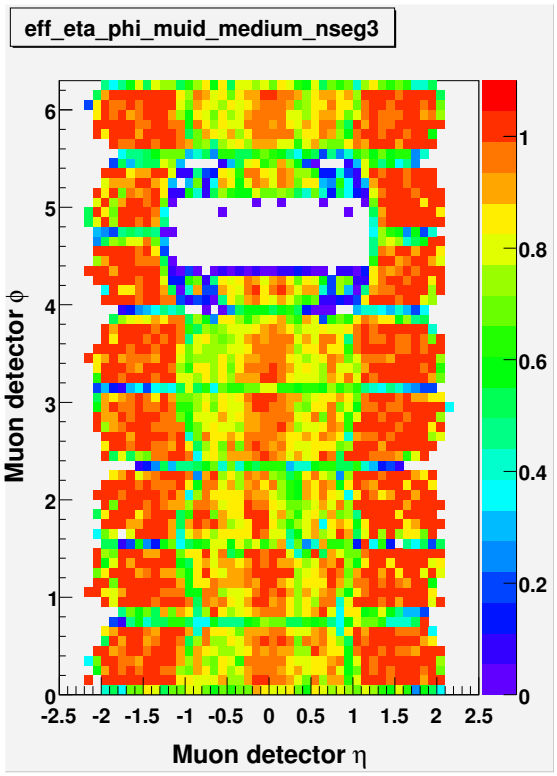

Figure 3.2: Muon reconstruction correction factor as a function of muon detector η and ϕ.

3.4 Calorimeter Energy Clusters

Reconstruction of energy cluster in the calorimeter is a principal step in identification of electrons, photons, taus, and jets. Two basic algorithms used to reconstruct calorimeter cluster will be discussed: the simple cone algorithm and the nearest-neighbor cell algorithm.

3.4.1 Simple cone algorithm

The simple cone algorithm uses a list of towers to build clusters which become input to more specific algorithms which reconstruct jets, electrons, photons and taus. The algorithm takes calorimeter towers as input and proceeds in the following steps:

1. All towers above a certain threshold ire collected in a list L, which is sorted in order of decreasing tower E_T.

2. The first tower in the list, I, is removed and becomes part of a new cluster C.

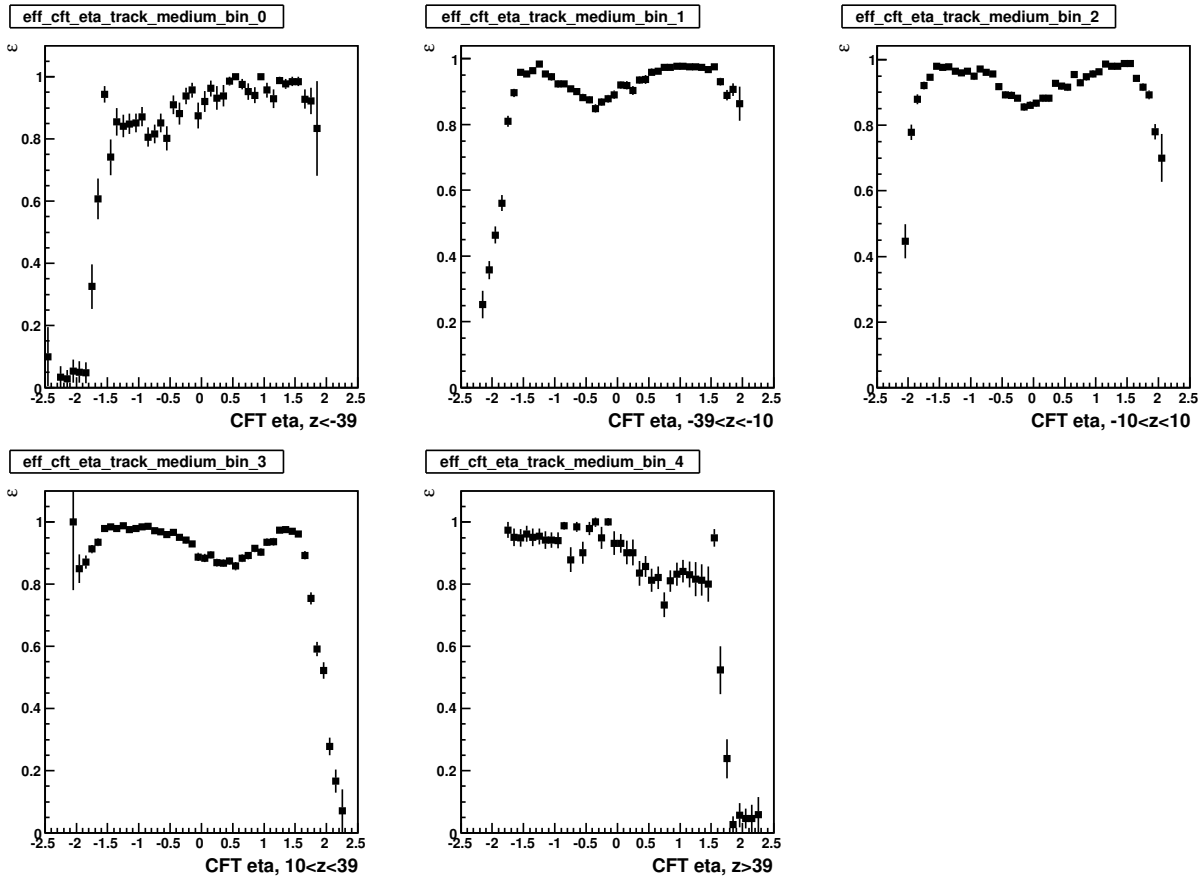

Figure 3.3: Muon track reconstruction correction factor as a function of CFT detector η, for different range of the track $z-$position.

3. The algorithm then loops over the remaining towers in the list. If the algorithm finds a tower J whose distance from the current cluster C, $\Delta R(C, J)$ is less than R_{cone}, where R_{cone} is the radius parameter of the algorithm, then the tower J is added to the cluster C and removed from the list of towers.

4. When the algorithm has reached the end of the list of towers, then the current cluster is added to the list of clusters.

5. Steps 1 to 4 are repeated until there are no more towers in the tower list.

The simple cone algorithm uses three key parameters: the minimum energy of a tower to be considered in the list of towers, the minimum energy of a tower to be combined with the current cluster, the maximum radius between a tower and the current cluster to have the tower combined

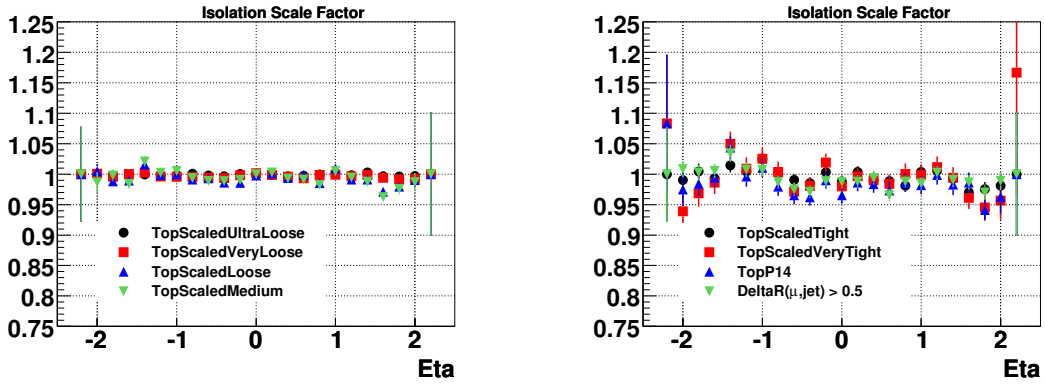

Figure 3.4: Muon isolation correction factor as a function of muon detector η, for different isolation criteria. The isolation criterion used in this analysis is TopScaledMedium.

with the cluster.

3.4.2 Nearest-neighbor (CellNN) algorithm

The principal difference between the simple cone algorithm and the nearest-neighbor (CellNN) algorithm is that the latter algorithm reconstructs a calorimeter cluster using cell information instead of tower information. An exhaustive description of the algorithm is available [35]. At DØ, this algorithm is used exclusively to reconstruct electromagnetic-related objects: electrons, photons, and electromagnetic sub clusters in tau decays. The motivation is to take full advantage of the third electromagnetic calorimeter layer (EM3) which has higher resolution as described in Section 2.4.

The algorithm first builds clusters of calorimeter cells for each layer (called *floor-cluster*) and then combines the resulting floor-clusters into global clusters. Each cell, on the same layer, with an energy readout above 200 MeV will start a new floor-cluster. Additional cells, again on the same layer, with energy above 25 MeV will be added to an existing floor-cluster if they are a neighbor to the seed cell in the floor-cluster. Figure 3.5 shows the two definitions of neighbor. A cell is neighbor to another cell if both of them share a side (four neighboring cells scheme) or a corner (eight neighboring cells scheme).

Merging of floor-clusters proceeds differently within the two neighboring schemes. For the 4-neighboring cell scheme, two seed cells are merged if they are sharing a corner, and the difference between the two seed cells (Cell 2 and 3 in Figure 3.6.(a)) and the maximum cell energy of the two

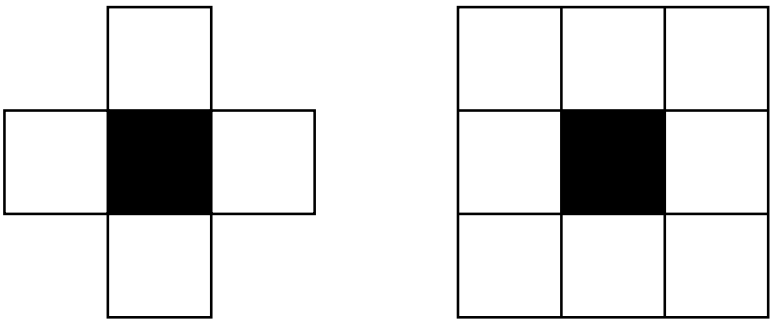

(a). Four neighboring cells scheme (b). Eight neighboring cells scheme

Figure 3.5: Two different neighboring schemes in nearest-neighbor cell clustering algorithm.

common neighbor cells (Cell 1 and 4 in the same figure) is less than 150 MeV.

For the 8-neighboring cell scheme, two seed cells are merged if the energy difference between one of the seed cells (Cell 1 or 3 in Figure 3.6.(b)) and the middle cell (Cell 2 in the same figure) is less than 350 MeV.

Reconstructed floor-clusters are then merged into global-clusters. Starting from the third electromagnetic layer, additional floor-clusters are added if their centroid are in a cone defined by a certain radius and the cone axis is defined by the floor-cluster in third electromagnetic layer and the interaction vertex.

3.5 Reconstruction of Electromagnetic Objects

Electromagnetic objects (electrons and photons) are reconstructed using information from the calorimeter, particularly the electromagnetic layers, and the track information [36, 37]. The reconstruction algorithm begins with reconstruction of electromagnetic calorimeter clusters. Two methods are used to perform this task:

1. A calorimeter cluster, found by either the simple cone algorithm or the nearest-neighbor cell algorithm. A cone radius of 0.4 is used to define the cluster size.

2. A track in the central tracking detector pointing to a electromagnetic calorimeter cells.

Electromagnetic object candidates are required to have a significant fraction of their energy deposited in the EM layer of the calorimeter. Their shower profiles are required to be consistent

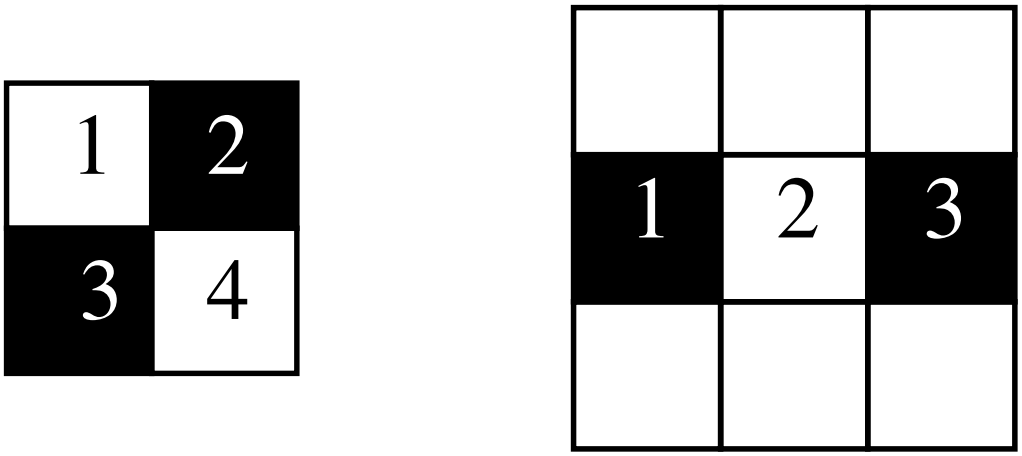

(a). Cluster merging in the 4-neighbor scheme. (b). Cluster merging in the 8-neighbor scheme.

Figure 3.6: Merging of two seed cells in the 4-neighbors scheme and 8-neighbor scheme to one single merged cluster.

with those of electrons or photons. The consistency check is performed with a χ^2 analysis of seven shower profile variables and comparing the results with those of signal electrons,

$$\chi^2_{\rm cal} = \sum_{i,j=1}^{7} \left(x_i - \overline{x}_i\right) H_{ij} \left(x_j - \overline{x}_j\right), \tag{3.4}$$

where the index i, j are running over the set of variables, x are the shower profile variables of the reconstructed electron, $\overline{x}$ are the averages of variables. The H_{ij} are elements of the inverse error matrix H, that is related to the well-known variance-covariance matrix M by

$$H_{ij} \;\; = \;\; (M^{-1})_{ij}. \tag{3.5}$$

The matrix M itself is determined using a large samples of well-reconstructed, reference electrons in Monte Carlo events and/or test beam events. Mathematically, the elements of the matrix M are defined as

$$M_{ij} \;\; = \;\; \frac{1}{N}\sum_{n=1}^{N}(x_i^n - \bar{x}_i)(x_j^n - \bar{x}_j). \tag{3.6}$$

Here the index n is running over the set of electrons, while the index i and j are running over the set of shower profile variables.

An electromagnetic isolation condition for the candidates is required. The definition of isolation fraction is:

$$f_{\rm iso} = \frac{E_{\rm tot}(\Delta\mathcal{R} < 0.4) - E_{EM}(\Delta\mathcal{R} < 0.2)}{E_{EM}(\Delta\mathcal{R} < 0.2)} \tag{3.7}$$

where $E_{\rm tot}(\Delta\mathcal{R} < 0.4)$ is the total energy inside the a cone of size $\Delta\mathcal{R} < 0.4$ around the direction of the electron, and $E_{EM}(\Delta\mathcal{R} < 0.2)$ is the energy in a similar cone of size $\Delta\mathcal{R} < 0.2$, summed over EM layers only.

For electrons only, they are required to have a track matched with their calorimeter clusters. The track must be within a road, centered at the centroid of the calorimeter cluster, and of size 0.1×0.1 in $\eta - \phi$ space. The final identification of electrons uses a likelihood discriminant with seven input variables [38]. Distributions of these seven variables are obtained from signal-like Monte Carlo events and background-dominated real events. The likelihood is defined as:

$$\mathcal{L} = \frac{P_{\rm sig}(\mathbf{x})}{P_{\rm sig}(\mathbf{x}) + P_{\rm bkg}(\mathbf{x})}, \tag{3.8}$$

where $\mathbf{x}$ is the vector of input variables to the likelihood. The probability is defined as the product of individual probability of each input variables, without correlations taken into account:

$$P_{\rm sig/bkg}(\mathbf{x}) = \prod_{i=1}^{7} P^i_{\rm sig/bkg}(x_i) \tag{3.9}$$

In this work, electron identification is used to find electrons for veto purposes, to reject electrons which fake jets, and to recalculate missing transverse energy. Two definitions of electrons are used: medium and tight.

- **Medium electron**

  1. Electrons are reconstructed either by the simple cone algorithm with cone size $R = 0.4$ or by extrapolation of a track from the central tracking detector to the electromagnetic calorimeter cells.
  2. Electrons must have fraction of energy deposited in the electromagnetic layer to be greater than 0.9,

  $$f_{\rm EM} > 0.9. \tag{3.10}$$

  3. Electrons are isolated from hadronic activity by requiring the electromagnetic isolation fraction, f_{iso}, to be less than 0.15,

  $$f_{\rm iso} < 0.15. \tag{3.11}$$

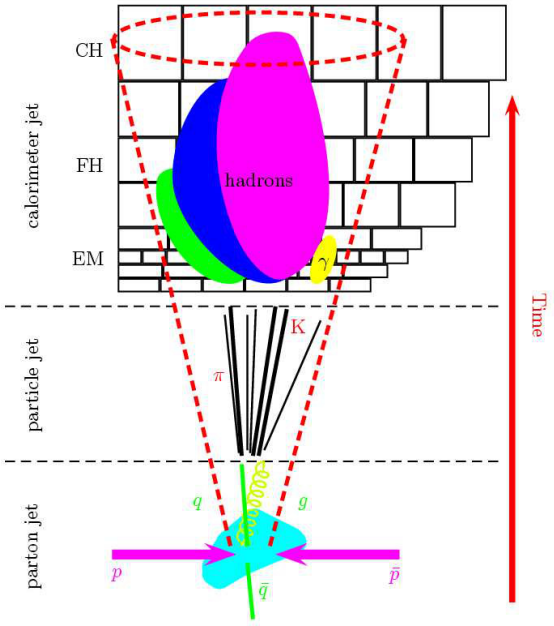

Figure 3.7: Evolution of a parton coming from hard scattering process into jet in the calorimeter.

4. Electrons must be matched to a track with p_T at least 5 GeV.
5. Electrons are required to have shower profiles consistent with an electron, $\chi^2_{\text{cal}} < 50.0$.

- **Tight electron**

  Tight electrons are required to fulfill the medium electron requirements and the electron likelihood requirements, $\mathcal{L} > 0.85$.

3.6 Jet Reconstruction

Strongly interacting partons (quarks and gluons) coming from hard scattering events will evolve into streams of hadrons and are reconstructed as energy deposition in the calorimeter. Figure 3.7 shows the evolution of a jet as seen by the detector. Initially the jet begins as a parton (gluon or quark) coming from a hard scatter event. At this stage, the jet is labeled as *parton-jet*. The parton hadronizes into hadrons, mostly pions and kaons. The jet at this stage is labeled as *particle-jet*. Finally, the hadrons deposit their energy in the calorimeter, and this final stage of evolution is named as *calorimeter jet*. This is the one which is seen by the detector, and reconstructed by the reconstruction algorithm.

Jets are reconstructed from energy in the calorimeter using Run II cone algorithm with cone size $R \leq 0.5$ [39]. The algorithm uses preclusters built by the simple cone algorithm with radius $R \leq 0.3$ as input [40]. A minimum threshold value of 6 GeV is used at both the particle-jet level and the reconstructed level. The DØ standard jet id cuts is used, which include requirements on Level 1 calorimeter trigger information, calorimeter electromagnetic fraction, and calorimeter coarse hadronic fraction [41].

3.6.1 Jet energy corrections

Corrections of the jet energy and momenta are done with the preliminary jet energy scale corrections for Run IIa data [42], which was determined using approximately 150 pb^{-1} of data. For jets which contain a muon with $\Delta R(\mu, jet) < 0.5$, we include semileptonic corrections which are assumed due to the decay of heavy flavors to muons.

The equation which expresses the jet energy correction can be written as:

$$E_{jet}^{particle} = \frac{E_{jet}^{raw} - O}{F_\eta \times R \times S} \tag{3.12}$$

where $E_{jet}^{particle}$ is the corrected jet energy, E_{jet}^{raw} is the uncorrected jet energy, O is the offset energy correction, F_η is the relative response correction (η-intercalibration), R is the absolute response correction, and S is the showering correction.

The offset energy correction corresponds to subtracting energy which is not coming from the hard scattering processes. The source of offset energies are underlying events, calorimeter noise, pile-up effect (energy from the previous collisions), and multiple interactions in the same beam crossing. This correction is measured using minimum bias events, taking into account the number of primary vertices in the events. This correction, for different primary vertex multiplicity, is shown in Figure 3.8. The amount of offset energy grows larger with higher vertex multiplicity. This is due to the presence of multiple interactions. It can be seen that the amount of offset energy is relatively small in the central pseudorapidity region, and grows larger toward the forward region.

The relative response correction adjusts for non-uniformities of response as a function of calorimeter pseudorapidity. Measurement of this correction is done on samples of γ+jets and dijet events, using the missing transverse energy projection fraction (MPF) method. The method is a tag-and-probe method which relates the momentum imbalance in the transverse plane between the tag object and the probe object. Figure 3.9 gives a schematic illustration of this method. For this measurement, the tag object (photon or jet) is required to be in the central calorimeter ($|\eta| < 0.5$)

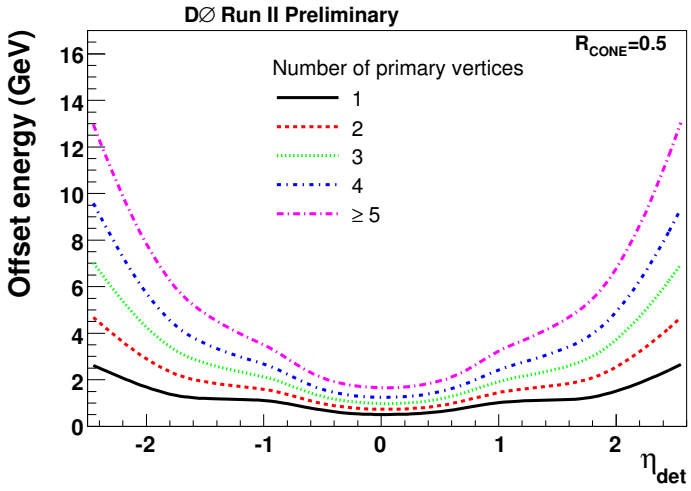

Figure 3.8: Offset energy correction for different primary vertex multiplicities as a function of the jet detector pseudorapidity.

to ensure that the tag object is fully reconstructed within the central calorimeter. Correction is measured as function of pseudorapidity, and observed to be largest in the gap region between the calorimeter cryostats, as can be seen in Figure 3.10.

After the offset and relative response corrections are applied, the calorimeter is expected to give uniform response as a function of energy. The uniform response correction is also measured by the MPF method on $\gamma+$ jet events with first applying the offset and relative response corrections to the probe object. Figure 3.11 shows the absolute response correction in data.

The last correction is the showering correction, which is applied to correct for energy leaking from(into) the jet reconstruction cone. It is important to understand that the showering correction is intended to correct for detector effects only, and not for physical effects such as gluon radiation. This correction is determined by measuring the jet energy profile density as a function of the radial distance in $\eta - \phi$ space from the jet axis. In data events, the measurement yields correction due to physics and detector effects, while in Monte Carlo the measurement yields correction to physics effects only. The ratio between data and Monte Carlo correction is the final showering correction. Figure 3.12 shows the showering correction as function of jet transverse energy.

Figure 3.13 shows the total fractional uncertainties on jet energy scale as a function of uncorrected jet transverse energy. The uncertainties are shown for three different pseudorapidity values. The individual uncertainties for different types of correction are also shown. The principal

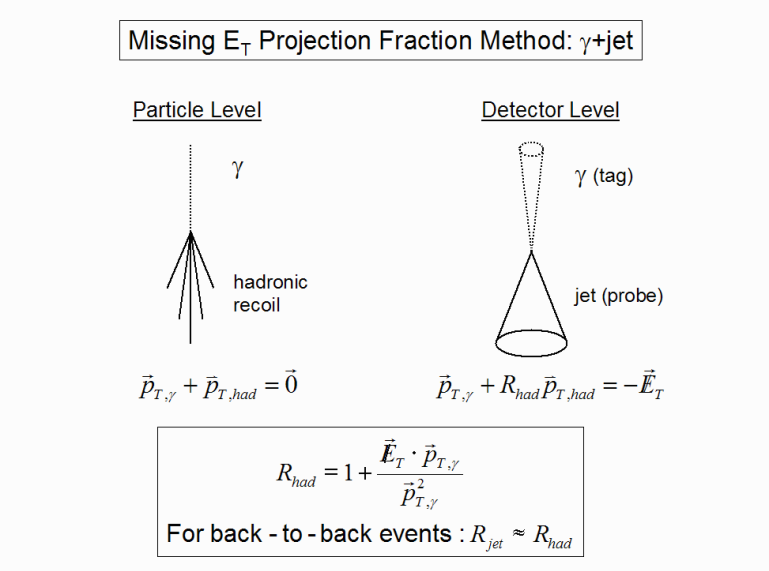

Figure 3.9: Schematic illustration of MPF method.

source of uncertainties is the response corrections. Statistical limitation dominates the uncertainties at high transverse energy domain, and also in the forward direction.

In Monte Carlo events, in addition to energy scale corrections, we also smear the jet energy and correct for the differences in jet reconstruction efficiency, and jet energy resolution in data and Monte Carlo [43]. This procedure is often referred as 'Jet Shifting, Smearing, and Removal (JSSR)'.

3.6.2 Identification of $b-$quark jets

The presence of one or more jets coming from a $b-$quark is an extremely powerful discriminator between signal top quark events and background events. This analysis uses a neural network algorithm to identify if a jet originated from a b-quark [44–46]. The algorithm uses seven input variables which characterize the difference between $b-$jets and light quark/gluon jets: properties of secondary vertices within the jets, impact parameter significance, and probability of the jet to originate from the primary vertex. Table 3.1 lists the seven input variables and their explanation.

We have chosen to use the MEDIUM operating point which is equivalent to requiring the neural network discriminant output to be greater than 0.65. For jets with corrected $p_T > 15$ GeV and $|\eta| < 2.4|$, the average efficiency for this operating point is about 54% for a b-jet, while the average fake rate is about 1%.

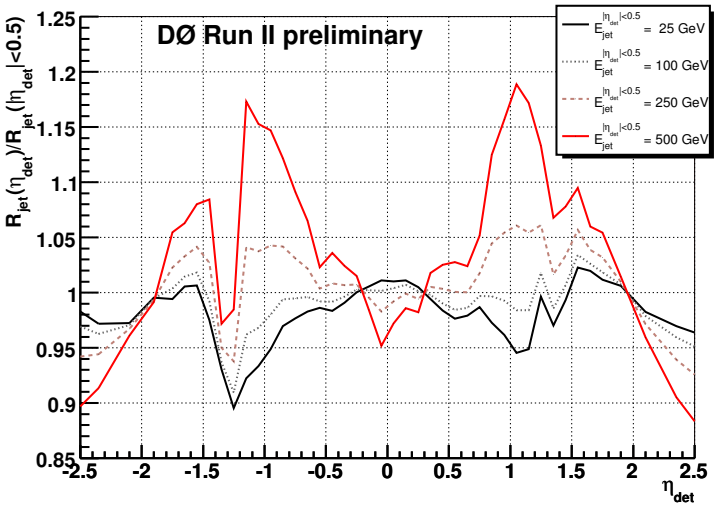

Figure 3.10: Relative response correction in data as a function of jet detector pseudorapidity.

Table 3.1: Input variables to the neural-network-based algorithm to identify $b-$quark jets.

Variable	Description
SVT_{SL} DLS	Decay length significance of the secondary vertex
CSIP Comb	Weighted combination of the tracks' impact parameter significance
JLIP Prob	Probability that the jet originates from the primary vertex
SVT_{SL} $\chi^2_{d.o.f.}$	Chi square per degree of freedom of the secondary vertex
SVT_L N_{tracks}	Number of tracks used to reconstruct the secondary vertex
SVT_{SL} Mass	Mass of the secondary vertex
SVT_{SL} Num	Number of secondary vertices found in the jet

In data events, the tagging algorithm is applied directly to jets in the events which pass the selection criteria. For each jet processed by the algorithm, the tagging algorithm decides if the jet is a b-jet or not.

In Monte Carlo events, the tagging algorithm is not applied directly. Instead, the algorithm assigns a probability value to each jet in the event to have originated from a $b-$quark. This probability value is measured from data and is often referred to as the "tag rate function". To increase the statistical power in Monte Carlo events, all possible permutations of the outcome of applying the tagging algorithm are considered. This permutation allows one to take advantage of event characteristics which are dependent on the kinematics of the $b-$jets.

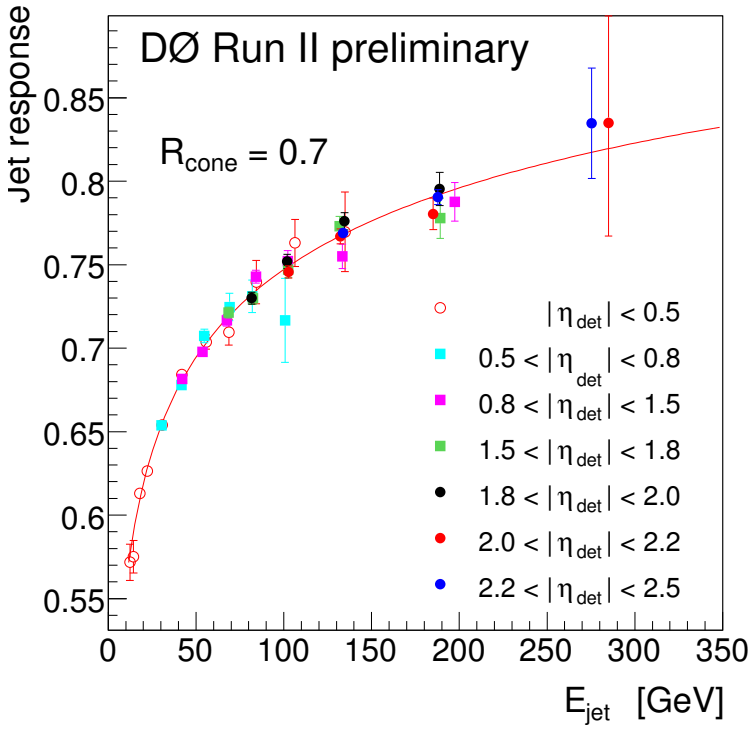

Figure 3.11: Absolute response correction in data after offset and relative response corrections as a function of partially-corrected jet energy.

3.7 Missing Transverse Energy

Neutrinos created in $p\bar{p}$ collisions will escape detection. The only signature of their presence is a non-vanishing sum of the momenta of reconstructed particles.

Reconstruction of missing transverse energy in an event begins by defining a four-momentum for each calorimeter cell, using the event's primary vertex to defined the direction of the four-momentum. Then the algorithm performs a vector sum of the transverse components (x and y) of all four-momenta associated with all cells, with the exception of cells in the coarse hadronic (CH) layers that are not associated with a well-reconstructed jet.

The sum is then corrected for the presence of well-reconstructed muons, electrons, and jets in the event. Energy scale corrections are applied to electrons and jets. The final result is the missing transverse energy which used in this analysis [47, 48].

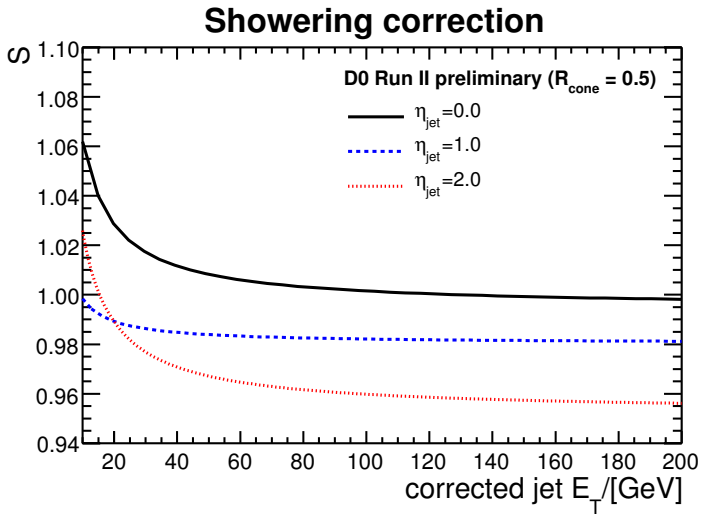

Figure 3.12: Showering correction in data as a function of corrected jet transverse energy.

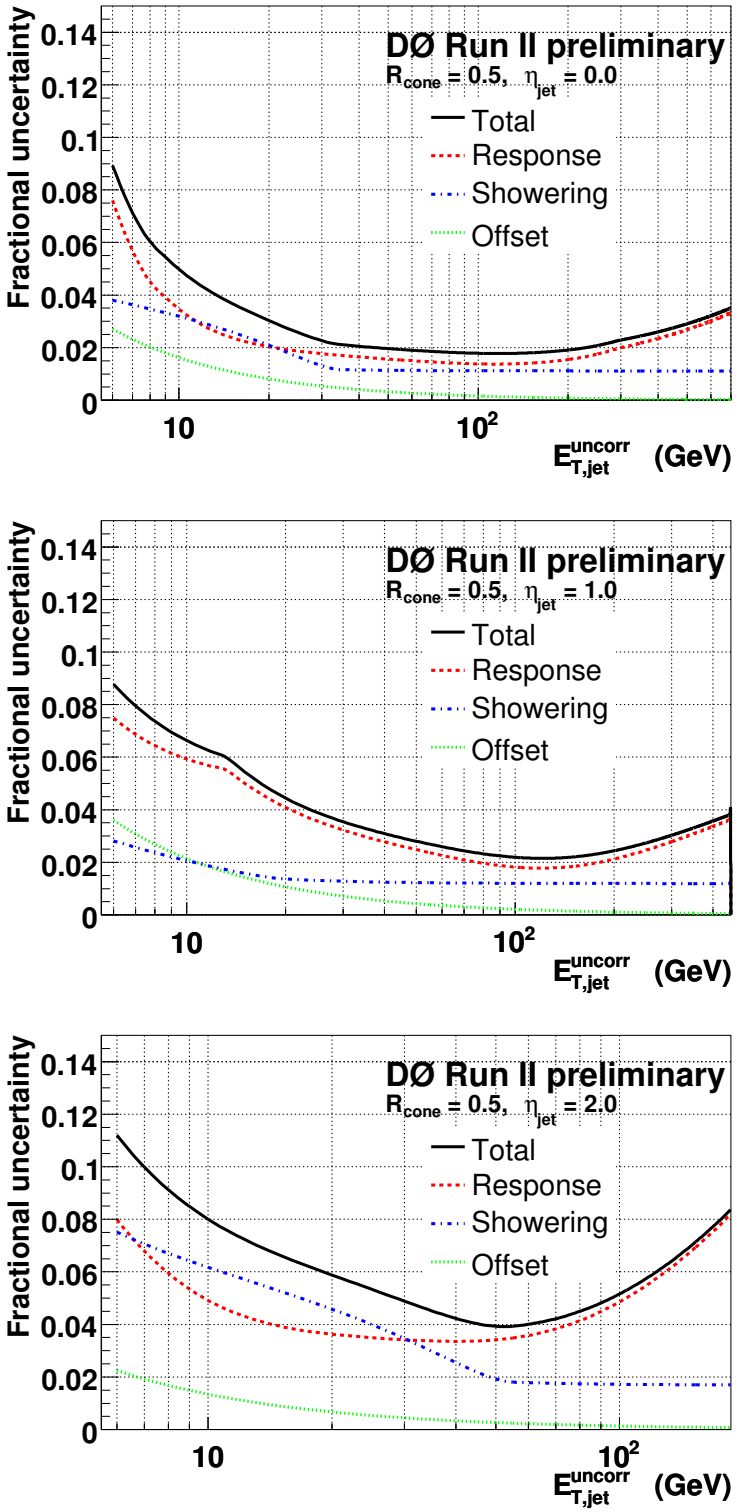

Figure 3.13: Fractional jet energy scale uncertainties as a function of uncorrected jet transverse energy, plotted for three different pseudorapidity values.

CHAPTER 4

TAU RECONSTRUCTION AND IDENTIFICATION

In the standard electroweak theory, the tau lepton belongs to the same family as electrons and muons. Its coupling to the electroweak vector bosons $W^{\pm}$ and Z is identical to that of the electron and the muon, while the tau differs in mass, lifetime, and decay modes. Table 4.1 lists the basic properties of the three charged leptons. Taus have lifetime of order 290×10^{-15} seconds with $c\tau = 87$ μm which is four to five times smaller than the $b-$quark lifetime. Therefore, the only way to observe taus is by reconstructing its decay products.

Taus can decay both into leptonic (electron or muon) or hadronic final states as has been shown before (Fig. 1.5). From Table 4.2, one can see that the branching ratio of tau decays into electrons or muons is approximately 35%. Electrons and muons from tau decays cannot be easily distinguished from electrons and muons coming directly from the parent particle. For example, the observable final state particles from

$$X \rightarrow \tau + \nu_{\tau} + Y \rightarrow e/\mu + \nu_{e/\mu} + \nu_{\tau} + Y,$$

are the same as for

$$X \rightarrow e/\mu + \nu_{e/\mu} + Y.$$

Therefore, leptonic decay modes of tau are usually included in analyses involving electrons or

Table 4.1: Basic properties of the three charged leptons.

Particle	Spin ($\hbar$)	Mass (MeV)	Charge (e)	Lifetime
e	1/2	0.511	-1	stable ($> 4.6 \times 10^{26}$) years
μ	1/2	105.658	-1	2.197×10^{-6} seconds
τ	1/2	1776.9	-1	0.290×10^{-12} seconds

Table 4.2: Branching ratios (in unit of %) for dominant leptonic and hadronic decay modes of tau, sorted by expected tau type, as stated in [21].

Decay modes	Branching ratio (%)
Leptonic decay	
$\tau^- \to e^- \bar{\nu}_e \nu_\tau$	17.84 ± 0.05
$\tau^- \to \mu^- \bar{\nu}_\mu \nu_\tau$	17.36 ± 0.05
Type 1 Hadronic single-prong decay without π^0	
$\tau^- \to \pi^- \nu_\tau$	10.90 ± 0.07
Type 2 Hadronic single-prong decay with π^0	
$\tau^- \to \pi^- \pi^0 \nu_\tau$	25.50 ± 0.10
$\tau^- \to \pi^- 2\pi^0 \nu_\tau$	9.47 ± 0.12
$\tau^- \to \pi^- 3\pi^0 \nu_\tau$	1.04 ± 0.08
Type 3 Hadronic three-prong decays	
$\tau^- \to \pi^- \pi^+ \pi^- \nu_\tau$	9.33 ± 0.08
$\tau^- \to \pi^- \pi^+ \pi^- \pi^0 \nu_\tau$	4.59 ± 0.07

muons. This analysis uses the hadronic decay modes to identify taus. From hereafter, the term tau will be used specifically to address taus which decay hadronically.

4.1 Reconstruction of Tau Candidates

In almost all hadronic decay modes of taus, charged and neutral pions are the dominant decay products. Charged pions deposit energy in the electromagnetic and hadronic layers of the calorimeter, and leave tracks in the tracking detector. Neutral pions decay into two photons which will deposit most of their energies in the electromagnetic layers of the calorimeter. A tau which decays hadronically will have many similarities to a jet from strongly interacting particles.

However, there are some major differences between tau jets and typical hadronic jets. Most taus produced from the decay of heavy particles like W or Z bosons are fairly energetic and have high boost factors resulting in decay products that are mostly collinear with the taus themselves. Jets from tau decays have a narrower radius than jets from hadronization of strongly interacting particles. They are also expected to have a small number of tracks, between one to three, associated with them, which result from the charged pions. The total sum of energy for the remaining tracks surrounding the tau is expected to be small.

The DØ tau reconstruction algorithm [49] finds and builds tau candidates from three primary elements:

1. **Calorimeter cluster**, which is reconstructed by a simple cone algorithm. The tau cone algorithm use a radius of $R < 0.5$. A co-axial cone of radius $R_{\rm iso} < 0.3$ is used to defined tau calorimeter isolation variables.

2. **Electromagnetic sub cluster(s)**, which is reconstructed using by the nearest-neighbor algorithm and is expected to come from neutral pions in tau decays.

3. **Track(s)**, which are expected to come from the charged pions in tau decays. The tau track matching algorithm follows these steps in matching a tau calorimeter cluster with tracks:

   (a) All tracks with transverse momentum greater than 1.5 GeV in a cone of radius 0.5 about the centroid of the calorimeter cluster are considered as candidates for the tau tracks. They are sorted in order of decreasing transverse momentum.

   (b) The first track (the one with the highest p_T) is always attached to the tau.

   (c) Up to two more tracks can be assigned to the tau if the tracks' $z-$position are within 2 cm from the first track at closest approach.

   (d) A second track is added if the invariant mass of the first and the second track is less than 1.1 GeV.

   (e) A third track is added if the invariant mass of the three tracks is less than 1.7 GeV and the total sum of their charges is either $+1$ or -1.

There is a possibility for tau candidates to have two tracks with charges sum to zero. Since this analysis requires the tau to have charge sign opposite that of the charge of lepton, such tau candidates are rejected. Tau candidates with two tracks that have a net charge of $+2$ or -2 are retained, and assigned a unit charge of the same sign with the total charge, i.e. $+1(-1)$ for taus with charge $+2(-2)$.

The tau identification sorts the reconstructed tau candidates into three types:

1. **Type 1:** One track without associated electromagnetic sub cluster. This type of tau candidates is expected to come from the decay $\tau^- \to \pi^- \nu_\tau$.

2. **Type 2:** One track with associated electromagnetic sub cluster. This type of tau candidates is expected to come from the decay $\tau^- \to \pi^- \, N\pi^0 \nu_\tau$, where there are $N \geq 1$ neutral pions.

3. **Type 3:** Two or three tracks. This type of tau candidate is expected to come from the decay $\tau^- \to \pi^-\pi^+\pi^- \, N\pi^0 \nu_\tau$, where there are $N \geq 0$ neutral pions.

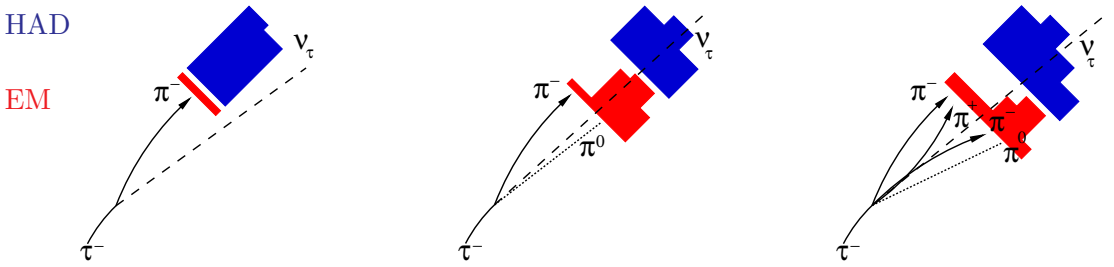

Type 1 Type 2 Type 3

Figure 4.1: Three tau decay types as defined by DØ tau reconstruction algorithm.

Figure 4.1 illustrates all three types. Notice the distinct feature of each tau decay type, in particular how each type gives different signatures in the central tracking detectors, electromagnetic, and hadronic calorimeter.

After the reconstruction stage, tau candidates contain candidates from real taus and other objects (fake taus). The primary source of fake taus is hadronic jets. Other physics objects which can also be reconstructed as fake taus are electrons and muons. Further selection criteria are then required to separate real taus from fake taus.

4.2 Separation of Taus and Hadronic Jets using Neural Network

A tau neural network (denoted by NN_τ in what follows) has been developed to distinguish taus from hadronic jets. A set of discriminating variables is selected as input to the neural network. The neural network is then trained by using tau candidates in $Z/\gamma^* \rightarrow \tau\tau$ Monte Carlo events in the mass range 130–250 GeV as signal, and tau candidates in fake-tau enriched data as background.

Twelve variables are used as input to the tau neural network. Each tau type will use a subset of these twelve variables. The chosen variables emphasize the difference of taus from hadronic jets: low track multiplicity, narrow calorimeter clusters, isolation in the central tracking system and the calorimeter, and correlation between the track(s) and calorimeter cluster(s). The variables are derived from tau tracks, hadronic and electromagnetic calorimeter cluster energies, shower shape, and the detector geometry. To minimize dependence on the absolute values of measured tau variables, many of the neural net input variables are defined as a ratio between two measured tau variables.

The chosen variables are:

1. $EM12isof$, which is defined as

$$EM12isof = \frac{E^{EM_1} + E^{EM_2}}{E^{\tau}}$$

where E^{τ} is the energy of the tau calorimeter cluster, E^{EM_1} and E^{EM_2} are energies deposited in the first two layers of the electromagnetic calorimeter, all in a cone of radius $R < 0.5$.

2. $trkiso$, which is defined as

$$trkiso = \frac{\sum p_T^{track}}{\sum p_T^{\tau_{track}}}$$

where $\sum p_T^{track}$ is sum of p_T of all extra tracks not associated with the tau within a cone of radius $R < 0.5$, and $\sum p_T^{\tau_{track}}$ is the sum of p_T of all tau track(s).

3. fhf (fine hadronic fraction), which is defined as the fraction of tau energy E_T^{τ} deposited in the fine hadronic layers of the calorimeter.

4. ET_o_sum, which is defined as

$$ET\_o\_sum = \frac{E_T^{\tau}}{E_T^{\tau} + \sum p_T^{\tau_{track}}}$$

where E_T^{τ} is the energy of the tau calorimeter cluster, and $\sum p_T^{\tau_{track}}$ is the sum of the tranverse momenta of all tracks associated with the tau tracks.

5. $dalpha$, which is defined as

$$dalpha = \frac{\sqrt{\left(\frac{\Delta\phi}{\sin\theta}\right)^2 + (\Delta\eta)^2}}{\pi}$$

where θ is polar angle of the vector sum of the tau track momenta. $\Delta\phi$ and $\Delta\eta$ are the difference in azimuthal angle and pseudorapidity, respectively, between the vector sum of the tau tracks and the vector sum of all electromagnetic sub clusters.

6. $prf3$, which is defined as transverse energy of leading EM sub cluster divided by the transverse energy deposited in the 3rd electromagnetic layer of the calorimeter within a cone of radius $R < 0.5$.

7. $profile$, which is defined as

$$profile = \frac{E_{T_1} + E_{T_2}}{E_T^{\tau}}$$

where E_{T_1} and E_{T_2} are the transverse energy of the two most energetic calorimeter towers.

8. $emET\_o\_ET$, which is defined as

$$emET\_o\_ET = \frac{E_T^{em}}{E_T^{\tau}}$$

where E_T^{em} is the transverse energy of the EM sub clusters.

9. $ett1\_o\_ETiso$, where

$$ett1\_o\_ETiso = \frac{p_T^{\text{leading } \tau \text{ track}}}{E_T^{\tau \text{ iso}}}$$

where $E_T^{\tau \text{ iso}}$ is the tau transverse energy within a cone of radius $R < 0.7$.

10. $caliso$, where

$$caliso = \frac{E_T^{\tau} - E_{Tcore}^{\tau}}{E_{Tcore}^{\tau}}$$

where E_T^{τ} is the tau cluster's energy within the cone of radius $R < 0.5$, E_{Tcore}^{τ} is the tau cluster's energy within the cone of radius $R < 0.3$.

11. rms, which is defined as

$$rms = \sqrt{\frac{\sum_{i=1}^{n} \left((\Delta\phi_i)^2 + (\Delta\eta_i)^2 \right) E_{T_i}}{E_T}}$$

where $\Delta\phi$ and $\Delta\eta$ are the differences in azimuthal angle ϕ and pseudorapidity η of the individual calorimeter cells relative to the centroid of the tau calorimeter cluster. The sum is performed over all calorimeter cells in the tau calorimeter cluster. This quantity is a measure of the tau calorimeter cluster width.

12. $etad/3$, which is the defined as

$$etad/3 = \frac{|\eta_{CAL}^{\tau}|}{3.0}$$

where η_{CAL}^{τ} is the η position of the tau cluster at the calorimeter. The factor 3.0 is applied to normalize this variable between 0.0 and 1.0, since the tau id algorithm limits the tau acceptance up to $|\eta_{CAL}^{\tau}| < 3.0$. This variable is meant to make the neural net algorithm sensitive to variation of the other variables with respect to η_{CAL}^{τ}.

Table 4.3 lists all input variables to the tau neural networks, and their usage by each neural network. Figure 4.2, 4.3, and 4.4 show the distributions of tau neural network input variables for $Z \rightarrow \tau\tau$ Monte Carlo events (dominated by real taus), $W \rightarrow \mu$+jets Monte Carlo events (dominated by fake taus), and data events (contain both real and fake taus).

Table 4.3: List of tau neural net input variables, and their usage by a particular tau type as input to their respective neural networks.

Variable name	Type 1	Type 2	Type 3
$EM12isof$	√		
$trkiso$	√	√	√
fhf	√	√	√
ET_o_sum	√	√	√
$dalpha$		√	√
$prf3$		√	
$profile$	√	√	√
$emET\_o\_ET$		√	√
$ett1\_o\_ETiso$			√
$caliso$	√	√	√
rms	√	√	√
$etad$	√	√	√

Figure 4.5 shows the neural net output for three samples: preselected $\mu\tau$ data events without tau neural net cut (contains both real and fake taus), $Z \rightarrow \tau^+\tau^-$ Monte Carlo (dominated by real taus), and $W \rightarrow \mu\nu$ (dominated by fake taus). All plots are normalized to unit area.

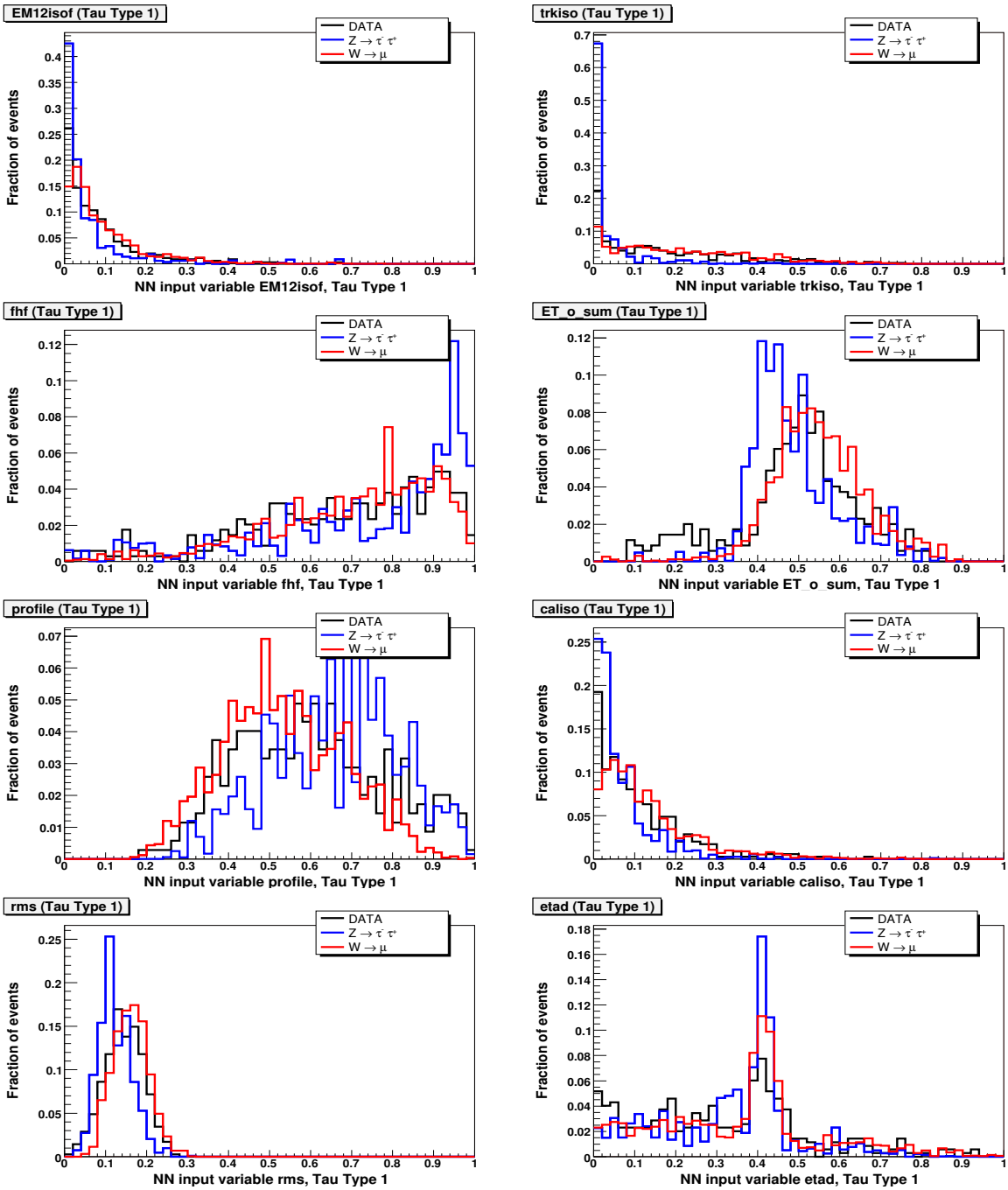

Figure 4.2: Distributions of the NN_τ input variables for tau type 1. Black histogram is data, blue histogram is Monte Carlo $Z \to \tau\tau$, and red histogram is Monte Carlo $W \to \mu$. All histograms are normalized to unit area.

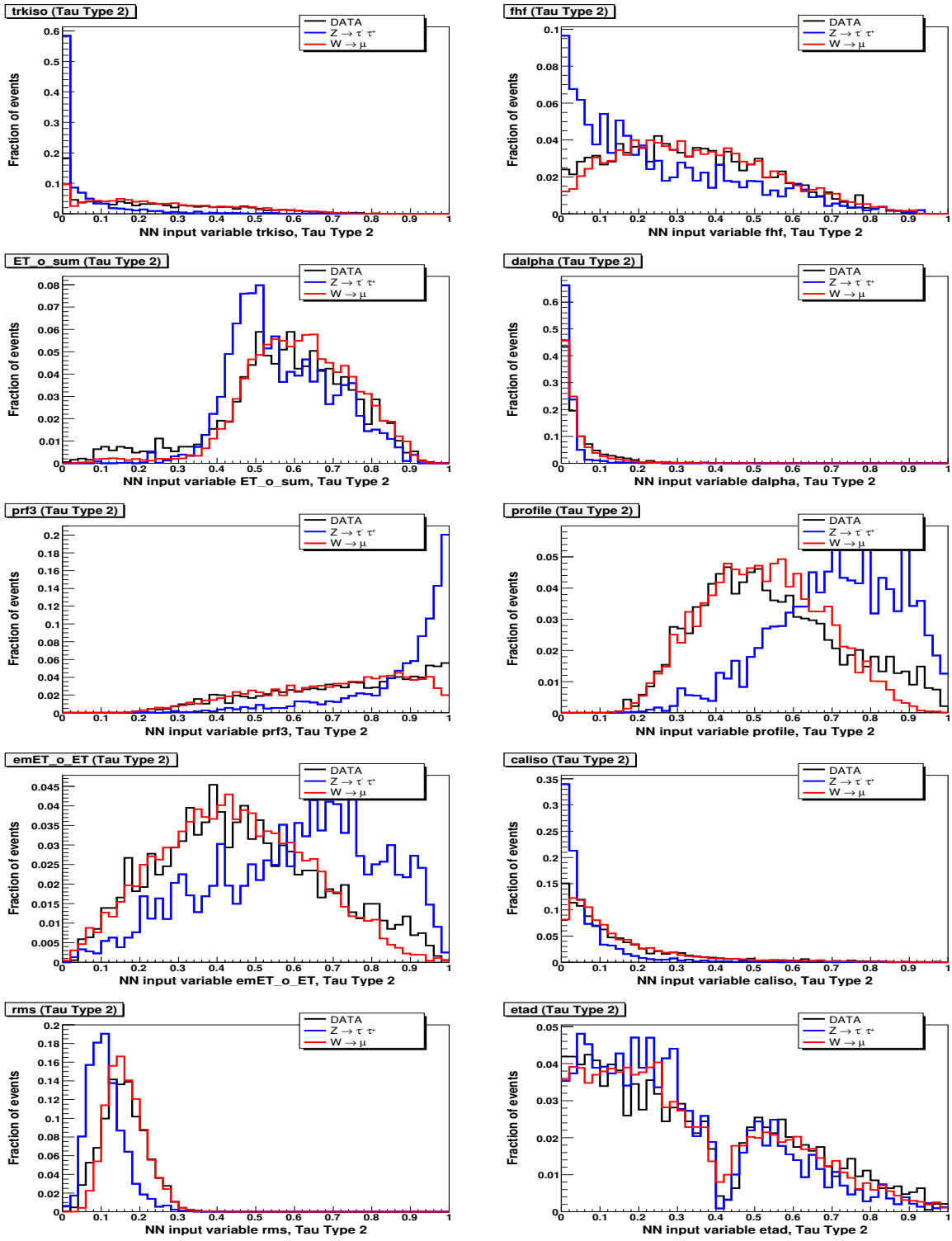

Figure 4.3: Distributions of the NN_τ input variables for tau type 2. Black histogram is data, blue histogram is Monte Carlo $Z \to \tau\tau$, and red histogram is Monte Carlo $W \to \mu$. All histograms are normalized to unit area.

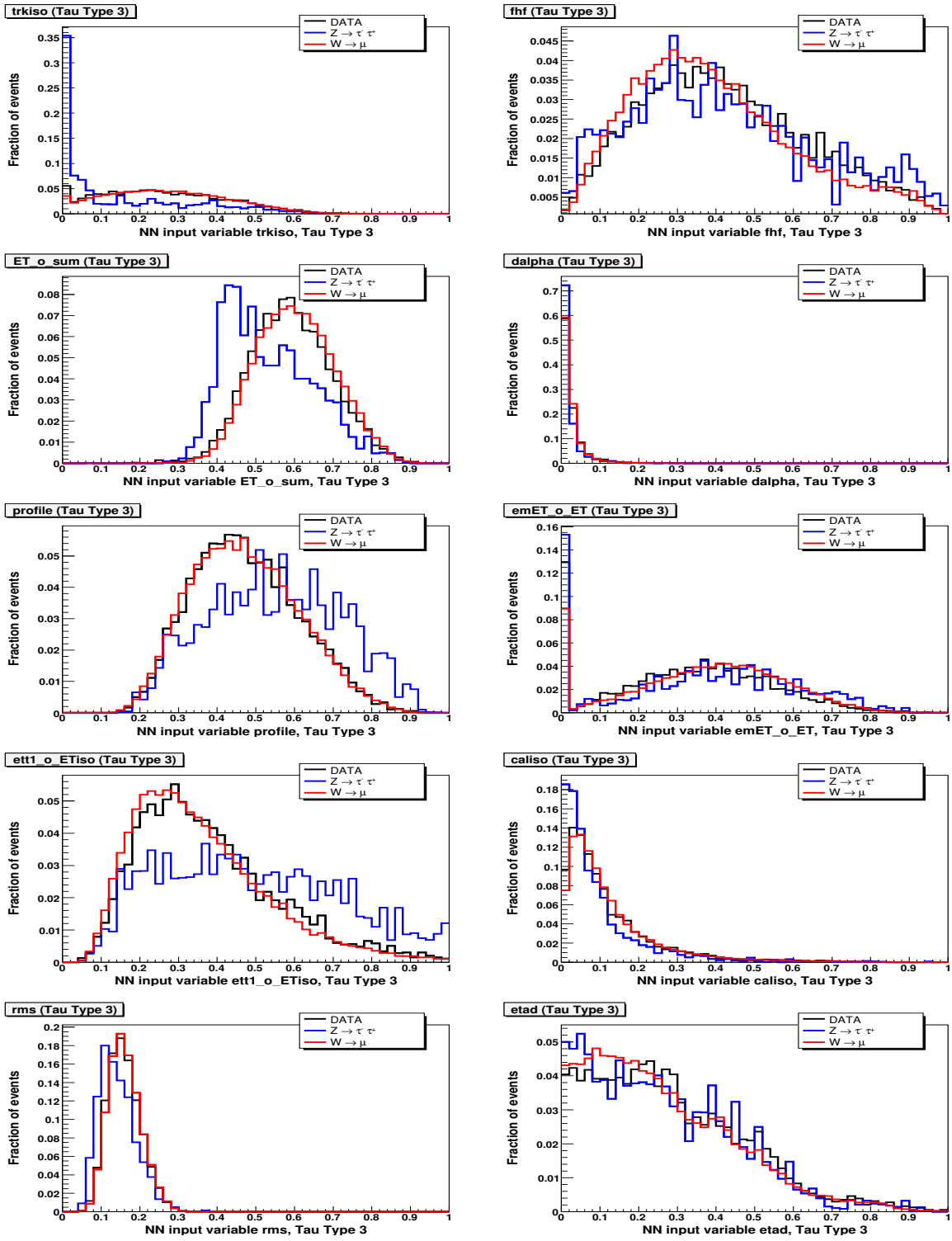

Figure 4.4: Distributions of the NN_τ input variables for tau type 3. Black histogram is data, blue histogram is Monte Carlo $Z \to \tau\tau$, and red histogram is Monte Carlo $W \to \mu$. All histogram is normalized to unit area.

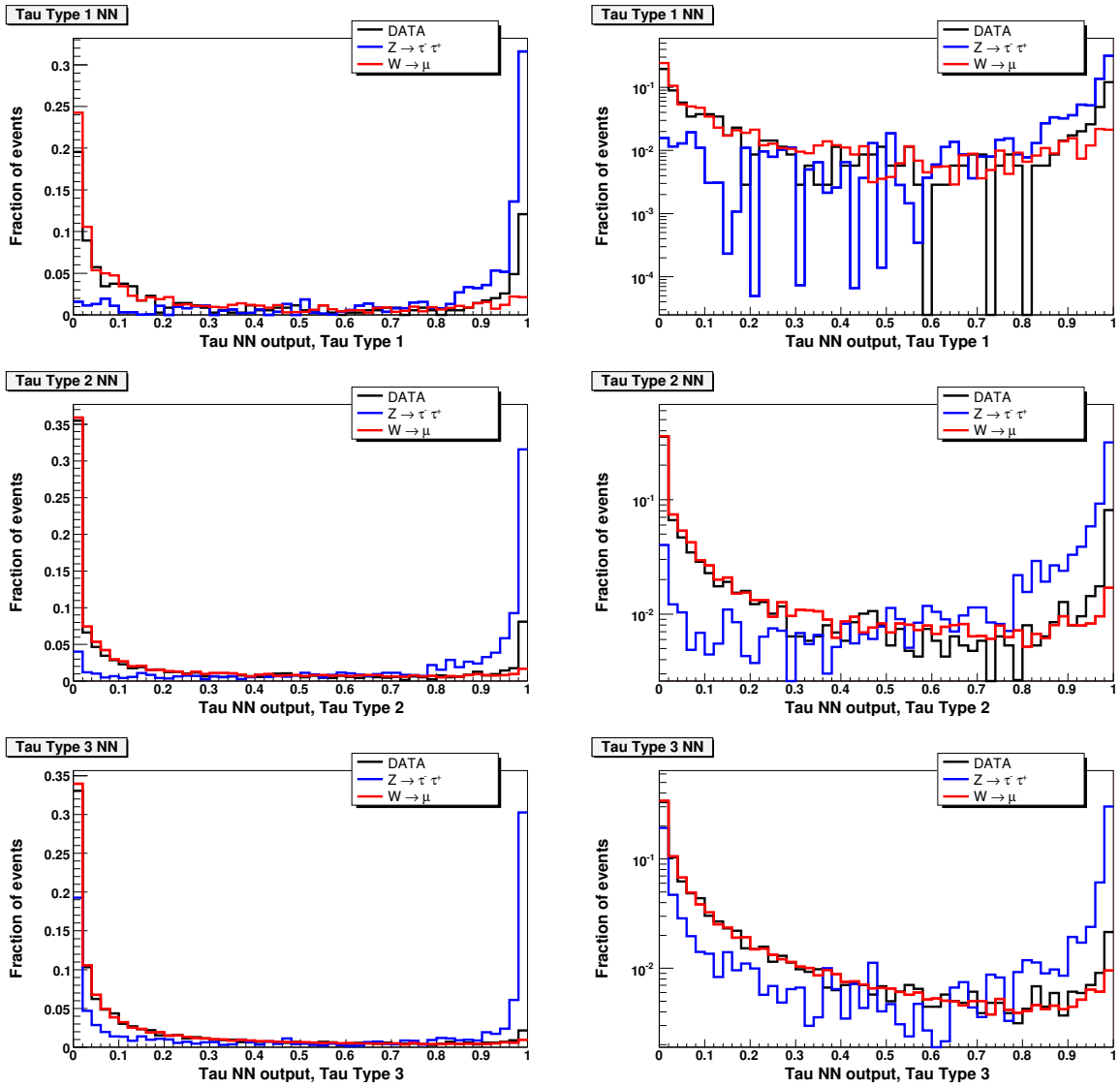

Figure 4.5: Distributions of the tau NN output for all three types. The left column is a linear scale while the right is the same distribution with a logarithmic scale. The top row shows type 1 taus, the middle row is type 2 taus, while the bottom row is type 3 taus. The black histogram is data, the blue histogram is $Z \to \tau\tau$ MC (signal), and the red histogram is $W \to \ell\nu$ MC (fake tau). The histograms are normalized to unit area.

CHAPTER 5

EVENT PRESELECTION

5.1 Data Set

This analysis uses a Run II dataset collected with the DØ detector from the period April 2002 through February 2006. The data have been processed with the DØ reconstruction software, including the new calorimeter hadronic calibration algorithm. The data were then converted into the DØ Common Analysis Format (CAF) and split into three datasets. Each dataset corresponds to the software version used to reconstruct the data, and the loose selection criteria used to create the dataset. This work uses the single muon loose inclusive datasets which require the presence of at least one muon in the events. Table 5.1 lists the datasets and the number of events in each.

5.1.1 Trigger

This analysis uses muon+jets trigger suites which are also used in the top pair production muon+jets analyses and single top production muon+jets analyses. Since the final state of interest consist of a high p_T muon, a hadronic tau which may also be reconstructed as a jet, and two high p_T b-jets, the muon+jet trigger suite is a suitable set of triggers for this analysis. Table 5.2 lists the trigger names used in this analysis and their respective luminosity. The total integrated luminosity is approximately 994 ± 61 pb^{-1}. The principal source of uncertainty in the integrated luminosity is the uncertainty in the value of inelastic $p\bar{p}$ cross-section.

Table 5.1: Names of datasets used in this analysis, and the number of events in each dataset.

Dataset name	Number of events
CSG_CAF_MUinclusive_PASS3_p17.09.03	266,513,739
CSG_CAF_MUinclusive_PASS3_p17.09.06	28,198,829
CSG_CAF_MUinclusive_PASS3_p17.09.06b	25,376,979

Table 5.2: Trigger names and their respective luminosities in each trigger version range.

Trigger version range	Trigger name	Luminosity (pb^{-1})
v8.00-v11.99	MU_JT20_L2M0	125.93
v12.00-v12.99	MU_JT25_L2M0	231.14
v13.00-v13.99	MUJ2_JT25	31.84
v14.00-v14.19	MUJ2_JT25_LM3	16.10
v14.00-v14.19	MUJ2_JT30_LM3	255.33
v14.20-v14.29	MUJ1_JT25_LM3	0.01
v14.30-v14.99	MUJ1_JT25_ILM3	21.89
v14.20-v14.29	MUJ1_JT35_LM3	311.92
Total		994.1 ± 60.6

5.1.2 Data quality

Events are required to be recorded in data-taking runs that are not considered bad for the following parts of DØ detector: calorimeter, silicon tracker, fiber tracker, and muon detector [50]. A list of bad luminosity block numbers, specific for the triggers used in the analysis, was generated. Events which are recorded within these bad luminosity blocks are rejected.

Some types of calorimeter noise occur randomly, independent of bad runs list and bad luminosity blocks list discussed before. Events which are flagged bad due to the presence of calorimeter noises are not used in the analysis. This problem needs to be taken into account as an inefficiency. A study with samples of zero-bias events resulted of an efficiency of 97.14% [51]. This is accounted for in the background estimates and signal efficiency.

The size of the single muon inclusive datasets above is large. A working subset of the datasets was made using the following selection criteria:

- Trigger and data quality.
- At least one loose isolated muon as defined in Section 3.3 with $p_T > 15$ GeV.
- At least one good jet as defined in Section 3.6 with $p_T > 15$ GeV.
- Vertex requirement. The event is required to have a primary vertex within the coverage of the silicon detector, namely the $z-$position to be less than 60 cm from the center of the detector; and to have at least three tracks attached to the primary vertex.

- The loose muon is required to be coming from the vicinity of the primary vertex, $\Delta z(\mu, \text{vertex}) < 1$ cm.

There are 237,308 events in the single muon inclusive dataset that pass these cuts. This will be referred as the *muon+jets skim*.

5.2 Monte Carlo Samples

5.2.1 Monte Carlo generator and samples

The ALPGEN version 2.05 [52] fixed-order matrix element (FOME) generator was used to generate signal $t\bar{t}$ samples and background W+jets and Z+jets samples. The background samples consist of vector bosons with light partons (W+Nlp, Z+Nlp) and heavy flavors ($Wc\bar{c}, Wb\bar{b}, Zc\bar{c}, Zb\bar{b}$). The factorization scale chosen was

$$Q^2 = M_V^2 + p_T^2(V) \tag{5.1}$$

where V refers to the vector boson type (W or Z). The MLM jet-matching algorithm was applied during sample generation [53, 54]. Pythia version 6.323 [55] is then used to add parton-level shower and hadronization. Since Pythia can add a $b\bar{b}$ and/or $c\bar{c}$ pair during the showering and hadronization processes, events in which Pythia has added $b\bar{b}$ and/or $c\bar{c}$ pair are removed. This is important to ensure that all heavy flavor pairs are coming from ALPGEN.

The decays of tau leptons and B mesons are not handled properly by Pythia. The TAUOLA version 2.5 library [56] is used to decay tau leptons. This library offers the following advanced features in simulating tau decays: availability of about twenty tau lepton decay modes, electroweak radiative corrections in leptonic decays, and precise treatment of hadronic decay matrix elements. The EvtGen version 00-00-17 library [57] is used to decay B hadrons. The library includes $CP-$violating decay modes and provides better simulation of angular correlation of B hadron decay products in cascade decays.

5.2.2 Heavy flavor K-factor

Higher-order calculation shows that the ratio of heavy-flavor jets to light flavor jets in W+jets and Z+jets production changed compared to leading-order calculation [58, 59]. We correct the heavy flavor to light flavor ratio in ALPGEN W+jets and Z+jets Monte Carlo by applying a relative scale factor to $W/Z + b\bar{b}$ and $W/Z + c\bar{c}$ samples before combining them with $W/Z + N$lp sample.

The factor for W+jets sample was determined by members of the DØ collaboration [60] to be

$$K_{HF} = 1.17 \pm 0.18. \tag{5.2}$$

For Z+jets sample, we refer to $ZH \to ee b\bar{b}$ and $ZH \to \mu\mu b\bar{b}$ analyses [61] which used the value

$$K_{HF} = 1.1 \pm 0.17. \tag{5.3}$$

5.2.3 Trigger efficiency corrections in Monte Carlo

The trigger efficiency corrections for Monte Carlo samples are done by weighting each Monte Carlo event with its probability to fire any of the triggers used during the data taking period. Efficiency turn-on curves are measured from unbiased data to determine the efficiency of physics objects to fire triggers at all trigger levels. For this analysis the relevant physics objects are the muon and jet, and the relevant triggers are muon triggers and jet triggers.

The muon and jet triggers are independent of each other, therefore the probability of an event to fire a muon+jets trigger can be written as the product of the probability to fire each trigger separately, that is:

$$P(\mu + \text{jets trigger}) = P(\mu \text{ trigger}) \times P(\text{jet trigger}) \tag{5.4}$$

The efficiency of muons(jets) to fire the three-level trigger system can be broken down into products of the probabilities of the muons(jets) to fire the muon(jets) trigger at each trigger level,

$$P(\mu \text{ trigger}) = P(\text{L1 } \mu) \times P(\text{L2 } \mu|\text{L1 } \mu) \times P(\text{L3 } \mu|\text{L2 } \mu \text{ \& L1 } \mu) \tag{5.5}$$

$$P(\text{jet trigger}) = P(\text{L1 jet}) \times P(\text{L2 jet}|\text{L1 jet}) \times P(\text{L3 jet}|\text{L2 jet \& L1 jet}) \tag{5.6}$$

where $P(X|Y)$ denotes the probability of X given a condition Y.

For each Monte Carlo event that passes the selection cuts, we calculate the probabilities that the event will fire each trigger listed in Table 5.2. The trigger probabilities for all triggers are then averaged by weighting the probability for each trigger by its respective recorded luminosity. The final probability for each Monte Carlo event is the probability that the event will fire *any* of the listed triggers during the data taking period. The value of the final trigger efficiency is about $80 - 85\%$.

5.3 Preselection of Muon+Jets Events

As discussed in section 1.5, the muon+tau analysis bears similarities to both a muon+jets and to a dilepton analysis. For example, in most of the running period there is not a muon+tau trigger,

therefore muon+jets trigger, as used by the muon+jets analysis, is chosen. Much of the advantage of having two oppositely charged leptons to reduce backgrounds remains. For the initial selection of events, this analysis combines the most applicable parts of both types of analyses.

5.3.1 General strategy

We adopt several general strategies for our preselection:

- We follow the muon+jets analysis in choosing to use muon+jets triggers.
- The initial preselection follows the muon+jets analysis, where we select events with one isolated muon and one or more good jets (described in this section).
- Then we select tau candidates in the lepton+jets sample (Section 5.4).
- Final selection adds the requirement of one or more of the jets to be $b-$jet.

5.3.2 Muon+jets selection criteria

Preselection at this level is designed to choose muon+jets events that satisfy the trigger requirements with high efficiency. We select events with one muon, at least one jet, and missing transverse energy. The following selection criteria are applied to the muon+jets skim:

- Muon+jets trigger.
- Exactly one tightly isolated muon (as described in Section 3.3) with $p_T > 20$ GeV.
- No other tightly isolated muon with $p_T > 15$ GeV.
- No other track-matched, loose quality muon with $p_T > 15$ GeV whose invariant mass with the isolated muon lies within the $Z-$mass window between 70 to 100 GeV.
- No isolated, tight electron (as described in Section 3.5) in the central calorimeter with $p_T > 15$ GeV.
- At least one jet (with all the corrections applied as described in Section 3.6) with $p_T > 30$ GeV; additional jets are allowed to have $p_T > 20$ GeV.
- Primary vertex to be located within the silicon detector, $|z_{PV}| < 60$ cm, and has at least three tracks attached to it.

Table 5.3: Summary of muon+jets selection criteria with some parameters and their effects on the muon+jets skim.

Cuts	Number of data events
Muon+jets skim	237308
Data quality	234094
Muon+jets trigger requirement as in Table 5.2	234094
Jet energy corrections	234094
Removal of jets which are matched to electrons	234094
Jet selection, at least one jet with $p_T > 20$ GeV, $\|\eta\| < 2.5$	229491
Leading jet selection p_T of the leading jet > 30 GeV	215022
Veto tight electrons	214909
Muon selection, at least one loose isolated muon with $p_T > 20$ GeV, $\|\eta\| < 2.0$	114504
Exactly one tight isolated muon	60136
Matching of the primary muon and fired muon trigger	59477
Veto second tight isolated muon with $p_T > 15$ GeV, $\|\eta\| < 2.0$	59185
Veto on Z-mass window (primary muon,any other muon) $M(\mu, \mu') > 100$ GeV or $M(\mu, \mu') < 70$	58242
Vertex requirement $v_z < 60$ cm, at least 3 tracks, $\Delta z(\mu, \text{vertex}) < 1.0$ cm	58242
Missing transverse energy requirement $15 < \not{E}_T < 200$ GeV	43425

- Muon is required to come from vicinity of the primary vertex, $|\Delta z(\mu, PV)| < 1.0$ cm.
- Missing transverse energy greater than 15 GeV to reject multijet events, and less than 200 GeV to reject events with badly reconstructed muons, $15 < \not{E}_T < 200$ GeV.

Tables 5.3 lists the selection criteria applied to the muon+jets skim and their effects on data reduction.

5.3.3 Normalization of W+jets events

The preseleced muon+jets events arise predominantly from W boson and multijet event production. Since W+jets events are a significant component of our background, we use this sample to determine the normalization factor for W+jets events. The choice to normalize the W+jets background using data is made with the following reasons:

- The ALPGEN Monte Carlo used to generate the W+jets samples is leading-order generator. Thus it can't be expected to yield a precise estimation of the W+jets cross-section.

- We will show later that after the tau selection, the sample will have four major components $W + jets$, $t\bar{t}$, $Z \to \mu^+\mu^-$+jets, and $Z \to \tau^+\tau^-$+jets. It is not trivial to normalize the W+ background at the stage after tau selection. Rather, normalizing this background at a stage where it still strongly dominates the sample would be a simpler and also reasonable approach.

To determine the normalization, we perform a two-component fit of the transverse mass of the muon + missing transverse energy. We use ALPGEN Monte Carlo to model the template of W+jets events (see Sec. 5.2). The template for multijet events was derived by using data events in which the muon is loosely isolated but fails the tight isolation. To gain full statistical power in the fit, we perform the fit using 1-jet inclusive sample. We subtract the estimated theoretical contribution from $t\bar{t}$ and Z+jets, using NLO cross-sections, before we perform the fit. Figure 5.1 shows the results of the fit.

The normalization factors are determined by varying a scale factor for each contribution and calculating a χ^2 between data and the sum of the contributions [62]. For W+jets template, the scale factor is the ratio between the observed number of W+jets events in data from the fit results and the expected W+jets events normalized using ALPGEN cross-sections. For the multijet template, the scale factor is the ratio between the observed number of multijet events in data from the fit results and the size of the multijet sample from which the template is derived. We are only concerned about the scale factor for W+jets events. The scale factor obtained from the fit is

$$\kappa_{W+\text{jets}} = 1.60 \pm 0.01 \tag{5.7}$$

We cross-check our modelling of W normalization by plotting some control variables which are characteristics of W+jets events. Figures 5.2 and 5.3 show some control variables in the μ+jets sample. There is good agreement between the observed data and Monte Carlo prediction in the control plots. Of particular importance is the agreement in jet multiplicity, meaning that the model also works at higher jet multiplicity.

5.4 Selection of Tau Candidates in Muon+Jets Events

Starting from the preselected muon+jets sample, we select events in the sample with at least one tau candidate. This section describes the selection and studies of the muon+tau+jets samples.

We require the following criteria for the tau candidates:

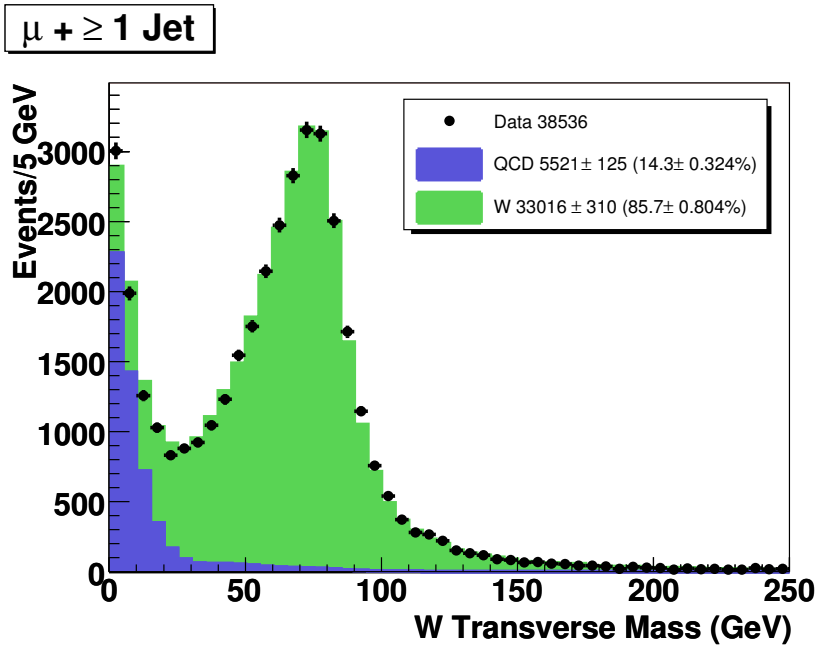

Figure 5.1: Distributions of the transverse mass from the muon+jets sample used to determine the W normalization factor. The filled histograms show the templates used in the fit and have been normalized using the results. Contributions from Z and $t\bar{t}$ have been subtracted from the data.

- Tau calorimeter cluster $E_T > 10/5/10$ GeV for type 1/2/3.
- Tau is required to be reconstructed in the central calorimeter, $|\eta^{\tau}_{CAL}| < 1.0$.
- The tau's leading track $p_T > 7/5/5$ GeV for type 1/2/3. In addition, for tau type 3, the total sum of tau tracks' p_T, $\sum p_T^{\tau\,\mathrm{track}} > 7$ GeV.
- Tau is separated from the muon. We require the muon's track and tau's leading track to be separated by $\Delta R > 0.5$. We also require that the muon's track and the tau'track are not the same object.
- Tau is coming from the same vertex as the muon, $\Delta z(\mu \text{ track}, \tau \text{ leading track}) < 1.0$ cm.
- The tau's charge is opposite that of the muon's charge.
- Tau neural net output is greater than 0.8 for all types.

For events with more than one tau candidate, we choose the one with the highest tau neural net output. After selecting events with a tau candidate, we recount the jet multiplicity in the

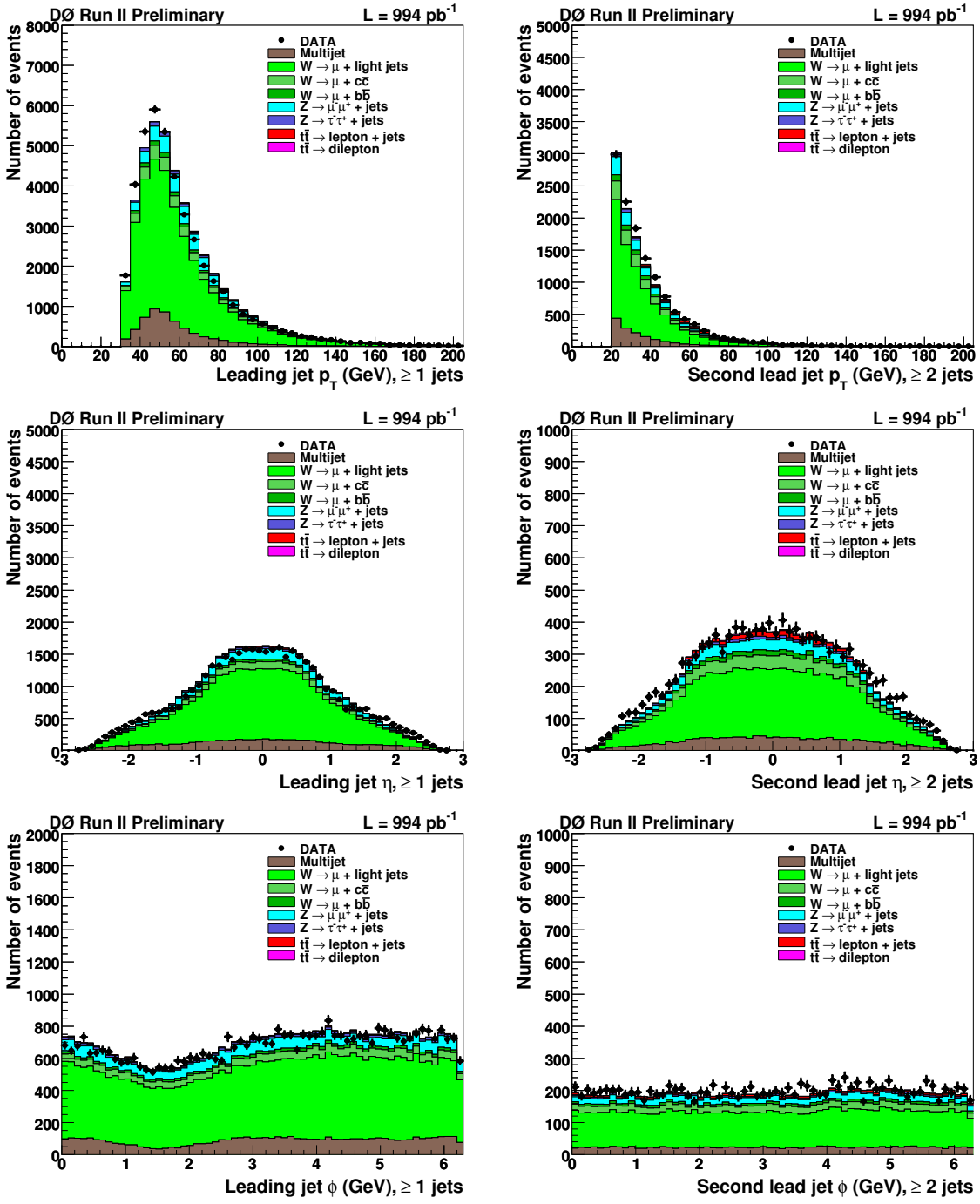

Figure 5.2: Distributions of control variables from the muon+jets sample including all contributions (part 1 of 2).

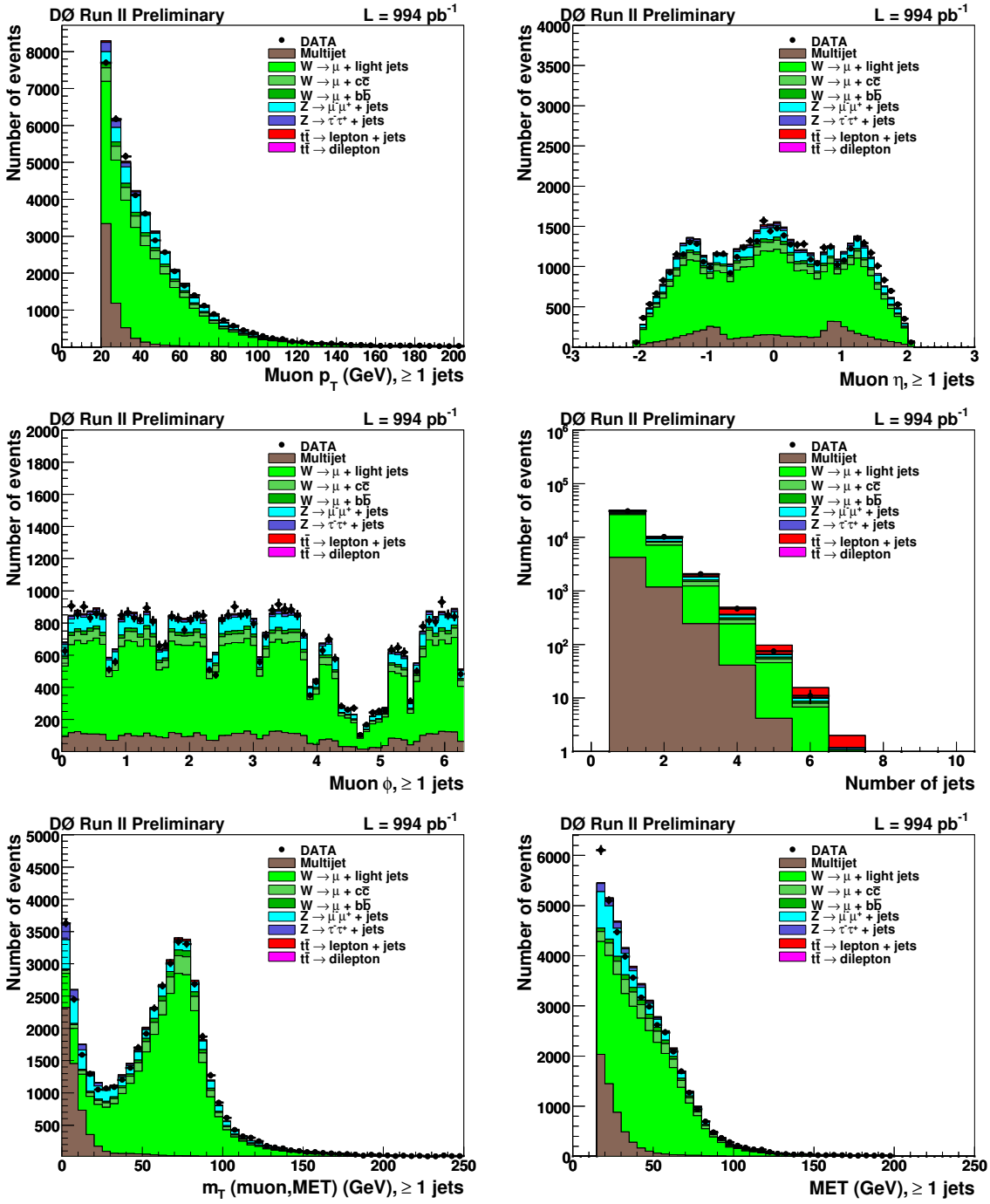

Figure 5.3: Distributions of control variables from the muon+jets sample including all contributions (part 2 of 2).

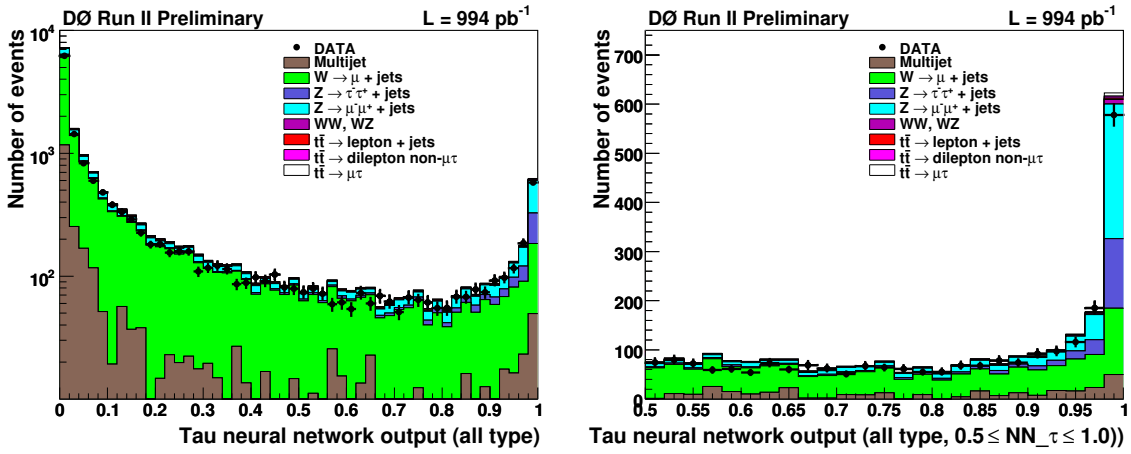

Figure 5.4: Distributions of tau neural net output (NN_τ) in the preselected muon+tau+jets sample before NN_τ cut. Left figure is for all values of NN_τ in logarithmic scale, right figure is for values of NN_τ greater than 0.5 in linear scale.

event. We check if one of the selected jets is the same object as the selected tau candidate. A jet is considered to be the same object as the tau candidate if it is separated from the tau candidate by a distance less than 0.5 in the $\eta - \phi$ plane

$$\Delta R(\tau, j) < 0.5. \tag{5.8}$$

If a jet is matched to the tau candidate, it is discarded from the list of selected jets. We require all selected jets in the event to be not matched to the tau. We reapply the jet criteria (e.g. leading jet $p_T > 30$ GeV) with the revised jet list.

Before the tau neural net cut is applied, we cross-check the validity of tau neural net output in data and Monte Carlo. Figure 5.4 shows the distributions of tau neural net output in the above sample before the application of tau neural net cut. We found good agreement between data and Monte Carlo in the prediction of tau neural net output. As expected, W+jets sample which has fake taus peaks near zero, while $Z \to \tau\tau$ sample which has real taus peaks near one.

We divide the lepton+tau+jets events sample into two disjoint samples. The first sample contains muon-tau pairs with opposite charge sign (OS). This sample contains the signal events, as well as various background contributions from Z+jets, W+jets, diboson, and multijet processes. The second sample contains the muon-tau pairs with have same-sign charge (SS). This sample is dominated by multijet and W+jets events. We use this sample to estimate contributions from multijet processes to the OS sample, as will be discussed in Section 5.5.1.

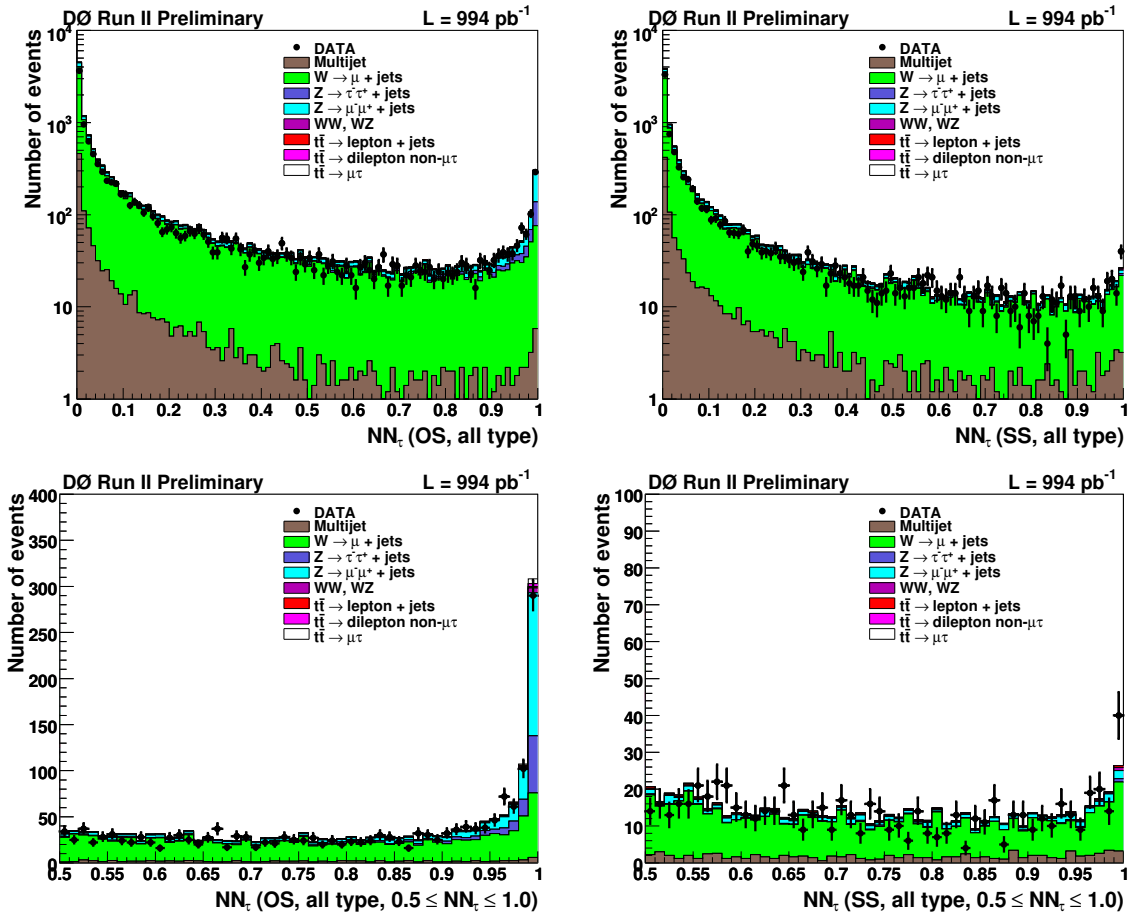

Figure 5.5: Distributions of tau neural net output (NN_τ) in the preselected muon+tau+jets sample before NN_τ cut. Left figure is for all values of NN_τ in logarithmic scale, right figure is for values of NN_τ greater than 0.5 in linear scale.

5.4.1 Monte Carlo to data correction factor for jets faking taus

A significant number of events passing our tau criteria arise from having a jet fake a tau. This results in non-negligible contributions from W+jets, multijet and $t\bar{t} \to \ell$+jets. Since the W and $t\bar{t}$ components are estimated from MC it is important to account for any differences between data and MC with respect to jets faking taus.

We use the muon+jets data sample from Section 5.3 and W+jets Monte Carlo to derive the Monte Carlo to data correction factor of jets faking taus. In addition to the muon+jets selection criteria, we add a cut on the minimum transverse mass of 40 GeV to reduce the multijet component. We also subtract the estimated contribution of $Z \to \tau\tau$, $Z \to \mu\mu$, and $t\bar{t}$ to the data sample to

Table 5.4: Number of events in data and Monte Carlo W+jets enriched sample. The Monte Carlo sample is normalized to the generator cross-section.

Sample	Number of events without tau requirement	Number of events with tau requirement
Data	6789.0	113.4
W+jets Monte Carlo	5431.9	84.3

increase the sample purity.

We cross-check that the samples used in this study are indeed dominated by W+jets events. Figure 5.6 shows the W transverse mass plots used in this calculation, before and after tau selection. Within statistical limitations (especially after tau selection), we found that the shapes of the transverse mass distributions; before and after tau selection; are consistent with samples which are enriched in W+jets events.

The correction factor is obtained by taking the ratio of tau fake rate in data and Monte Carlo. This will ensure that the correction factor is independent of Monte Carlo normalization. Table 5.4 lists the estimated number of W+jets events in data and Monte Carlo without and with tau requirement. The correction factor is defined as:

$$f = \frac{\frac{\#\text{of data w/ tau}}{\#\text{of data}}}{\frac{\#\text{of MC w/ tau}}{\#\text{of MC}}} = \frac{\frac{113.4}{6789.0}}{\frac{84.3}{5431.9}} \quad (5.9)$$

$$= 1.04 \pm 0.08 \quad (5.10)$$

This value is then applied to W+jets and $t\bar{t} \to \ell$+jets samples in the rest of this analysis.

5.5 Background Yield Estimation

5.5.1 Multijet events

The contributions of multijet background comes primarily from heavy-quark pair production, $b\bar{b}$ and $c\bar{c}$ production. One of the heavy-quark decays via semileptonic process into a muon which becomes isolated, while the fake tau come from a jet.

Events with same-sign charge lepton-tau pair (SS) are used to estimate the contribution of multijet processes in the opposite-sign (OS) sample. We use the following two assumptions to make the estimation of multijet background:

- Taus in SS sample are dominated by fake taus that come from multijet and W+jets-like processes.

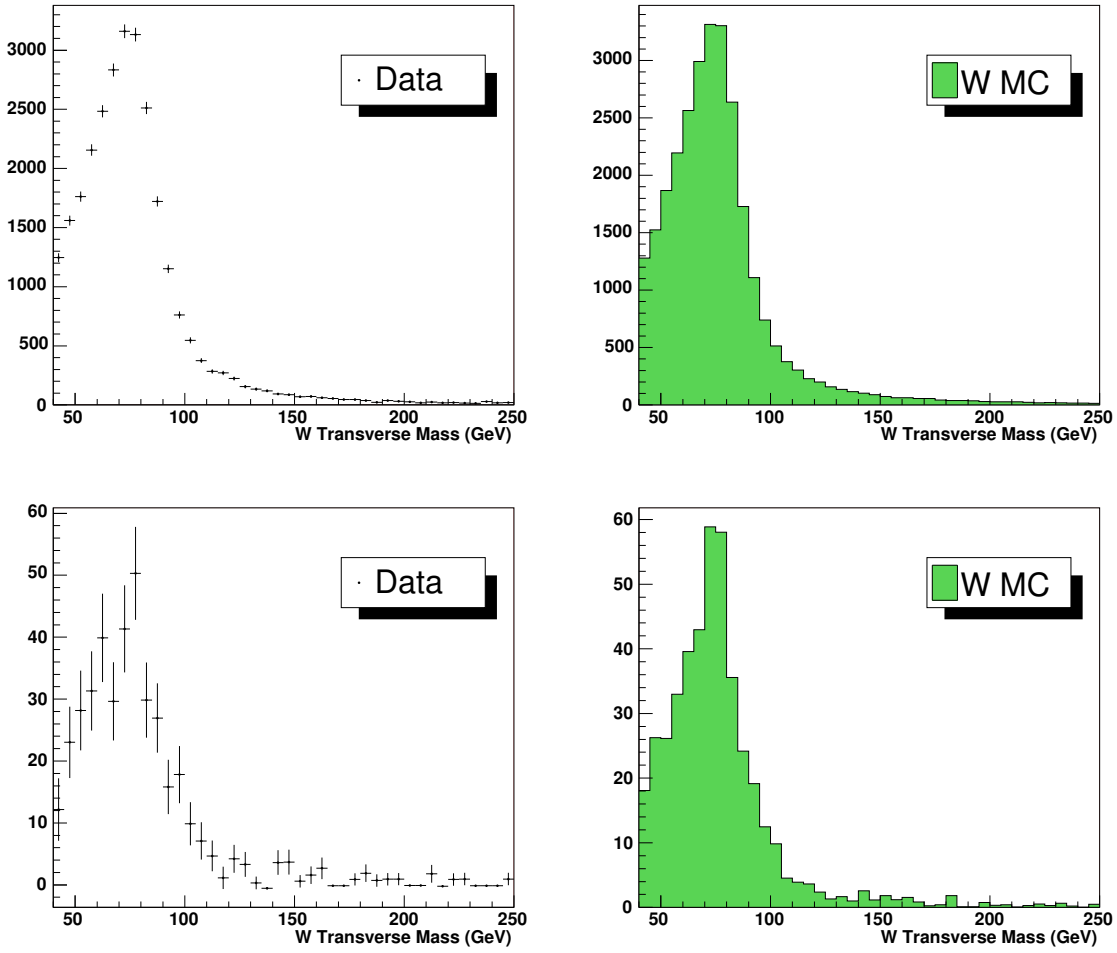

Figure 5.6: Distributions of the W transverse mass for the muon+jets sample. The top row shows the distributions where a muon and at least one jet are required. The bottom rows shows distributions where a tau is required to be found. The left are data (with Z, multijet and $t\bar{t}$ subtracted) while the right are W MC.

- Multijet processes contribute equally to the SS sample and OS sample.

With those assumptions, we estimate that the contributions of multijet events in the OS sample is approximately equal to the number of events in the SS sample after subtracting the contributions of W+jets and $t\bar{t}$ processes to the SS sample.

$$N_{QCD}^{OS} = N_{QCD}^{SS} = N_{DATA}^{SS} - N_{W+\text{jets}}^{SS} - N_{t\bar{t}}^{SS} \tag{5.11}$$

Table 5.5 lists the observed number of events in SS data sample, and the estimated contributions of W+jets and $t\bar{t}$ lepton+jets into the SS data sample for the $\mu\tau$ channel. A negative sign means the

Table 5.5: Observed/expected same-sign events in data at the pre-tagged level, and the expected amount of W+jets and $t\bar{t}$ lepton+jets events to be subtracted from SS data to get the estimation of multijet background contributions in the opposite sign (OS) sample.

Sample	Type 1	Type 2	Type 3	All type
SS data	3 ± 1.73	12 ± 3.46	23 ± 4.80	38 ± 6.16
SS $t\bar{t} \rightarrow$ dilepton	-0.00 ± 0.00	-0.06 ± 0.00	-0.21 ± 0.01	-0.28 ± 0.01
SS $t\bar{t} \rightarrow$ lepton+jets	-0.06 ± 0.01	-0.52 ± 0.03	-4.30 ± 0.09	-4.88 ± 0.09
SS $Wb\bar{b}$	-0.02 ± 0.01	-0.12 ± 0.03	-0.72 ± 0.14	-0.86 ± 0.16
SS $Wc\bar{c}$	-0.06 ± 0.04	-0.42 ± 0.14	-3.95 ± 0.80	-4.43 ± 0.87
SS WNlp	-0.33 ± 0.18	-3.29 ± 0.52	-11.32 ± 0.95	-14.95 ± 1.10
TOTAL	2.53 ± 1.74	7.65 ± 3.51	2.71 ± 5.01	12.89 ± 6.40

Table 5.6: Sum of ALPGEN LO cross-section across different parton-level multiplicity bins for different mass ranges, the corresponding NLO theoretical cross-sections, and the relative scale factor between the two. Here the Z boson is decayed into one lepton flavor only.

Process	$\sum \sigma_{\mathrm{ALPGEN}}$	σ_{NLO}	K_Z
$Z+ \rightarrow \ell\ell +$ (15 GeV $< m(\ell,\ell) <$ 60 GeV)	386.02	409.3	1.06 ± 0.1
$Z+ \rightarrow \ell\ell +$ (60 GeV $< m(\ell,\ell) <$ 130 GeV)	195.33	241.6	1.23 ± 0.1
$Z+ \rightarrow \ell\ell +$ (130 GeV $< m(\ell,\ell) <$ 250 GeV)	1.42	1.92	1.33 ± 0.1

contributions are to be subtracted from the SS data to make the estimation of multijet background contributions in the OS data sample. The errors included are statistical error only.

Figure 5.7 shows the transverse mass distributions in SS sample at the pre-tagged level, before and after subtraction of W+jets and $t\bar{t}$. It is clear that the sample is dominated by W+jets events. In the 2-jet inclusive sample, we also expect some contributions from $t\bar{t}$ lepton+jets events. We do not expect any contributions from Z events.

5.5.2 Z+jets events

The Z background is normalized by using the NLO theoretical cross-sections [63]. Table 5.6 lists the ALPGEN cross-sections for $Z \rightarrow \ell\ell$ processes, the NLO theoretical cross-sections used for normalization, and the scaling factors required to correct the ALPGEN cross-sections to match NLO theoretical cross-sections. We assume that the cross-sections are identical for Z decaying into $\mu\mu$ and $\tau\tau$. We assign an error of ± 0.1 to those scale factors. For $Z + b\bar{b}$ and $Z + c\bar{c}$ we apply additional heavy flavor K-factor of 1.1 as has been discussed earlier in Section 5.2.2.

As a cross-check, we also derive the normalization scaling factor from data. We select events

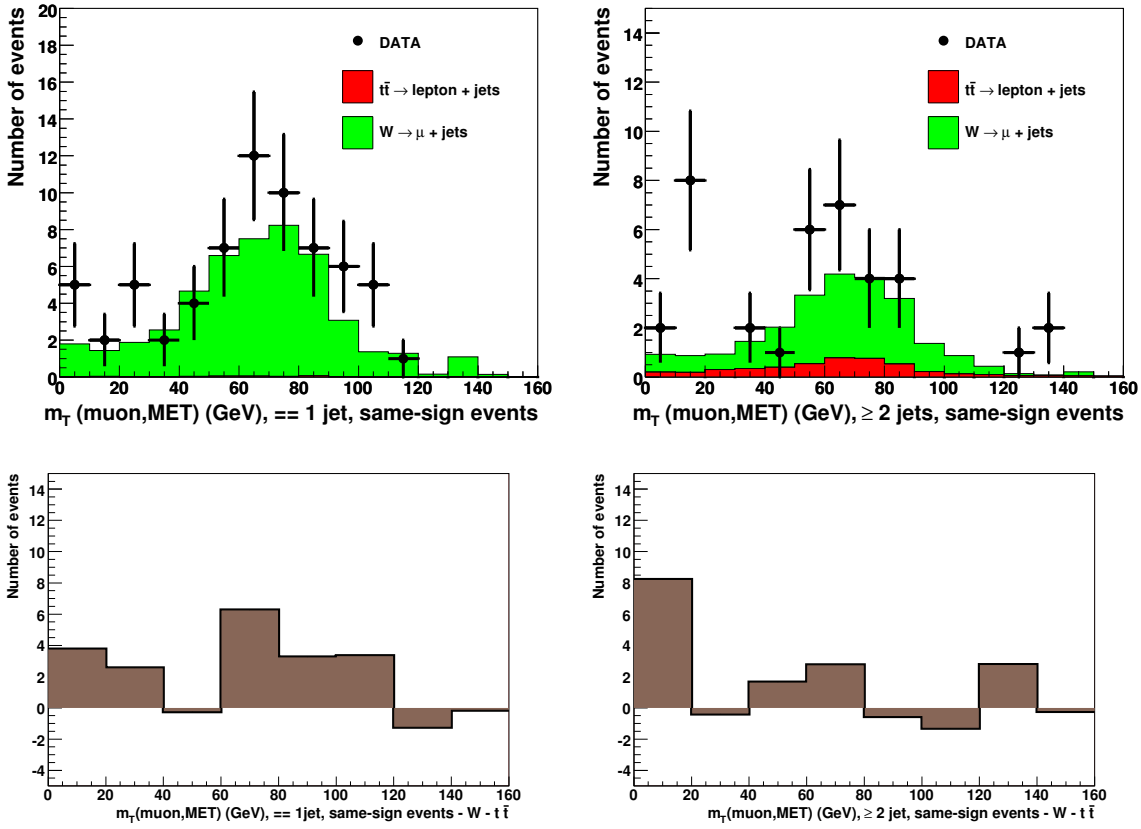

Figure 5.7: Transverse mass distributions in the SS sample at the pre-tagged level. Left column is for events with exactly one jet, right column is for events with two or more jets. Top row show the distributions before subtraction of W+jets and $t\bar{t}$ events. Bottom row show the distributions after subtraction of W+jets and $t\bar{t}$ events, with gray-shaded areas indicate the statistical errors.

with two isolated muons and one or more jets, using the same criteria for leptons and jets, same trigger and same dataset, but remove the tau requirements. Then we fit the dilepton invariant mass distributions using a template from ALPGEN Monte Carlo to data. A scale factor of

$$\kappa_{Z+\text{jets}} = 1.30 \pm 0.03 \tag{5.12}$$

is obtained from the fit. The fit result is consistent with the K_Z factor and its assigned error obtained by taking the ratio of NLO to ALPGEN LO cross-sections.

We cross-check the method of Z+jets normalization by checking the distributions of control variables in the dimuon sample. Figure 5.8 shows the distributions of these control variables. The Monte Carlo template is built of $Z/\gamma \rightarrow \mu\mu$ samples in three different dimuon mass bins: 15-60

Table 5.7: List of Pythia diboson MC used in this analysis.

Sample	Number of generated events	σ_{NLO}(pb)
$WW \rightarrow$ inclusive	1,984,651	12.0
$WZ \rightarrow$ inclusive	276,520	3.68

GeV, 60-130 GeV, and 130-250 GeV. We found that the contribution from the 15-60 GeV and 130-250 GeV are small, and fitting template is strongly dominated by the 60-130 GeV mass bin. Good agreement is found between the observed data and Monte Carlo prediction.

5.5.3 Diboson events

The contributions from dibosons are estimated purely from PYTHIA Monte Carlo, normalized to NLO cross-sections. We consider to include the WW and WZ processes in the background estimation. The inclusive cross-section for the third diboson process, ZZ, is smaller than the $t\bar{t}$ cross-section, and we expect that the contribution will be negligible. Table 5.7 lists the MC diboson samples used in this analysis and their respective cross-sections.

5.6 Analysis of Pre-tagged Sample

We defined the pre-tagged sample as the sample that pass the muon+tau+jets selection criteria as described in Sections 5.3 and 5.4. There are 104 events in the pre-tagged sample. Breaking down the samples into tau type, we found that there are 15 events with tau type 1, 37 events with tau type 2, and 52 events with tau type 3. The analysis is therefore statistically limited.

Table 5.8 lists the contributions of various processes into the muon+tau+$\geq$2 jets sample at the pre-tag level. Some processes such as Z+jets in the mass bin $15 - 60$ GeV and $130 - 250$ GeV only contribute a small amount into the total expected events. One can see that there are four dominant processes in this sample: $t\bar{t}$ signal, $W \rightarrow \mu$+jets, $Z \rightarrow \mu^{-}\mu^{+}$+jets, and $Z \rightarrow \tau^{-}\tau^{+}$+jets.

We check distributions of control variables that are expected to uniquely characterize the muon+tau+jets sample. In general, the selected sample has characteristics of W+jets (due to the presence of $t\bar{t}$ and W+jets component) and Z+jets events (due to the presence of $Z \rightarrow \mu^{-}\mu^{+}$+jets and $Z \rightarrow \tau^{-}\tau^{+}$+jets). We chose variables which characterize W+jets-like events (such as transverse mass, the azimuthal difference between the muon and missing transverse energy) and those which characterize Z+jets events (such as the invariant mass between the muon and tau, the azimuthal difference between the muon and the tau). Figure 5.9 and 5.10 shows distributions of control

Table 5.8: Estimated and observed yield for various component in the $\mu\tau$ OS sample with at least two jets and no $b-$tagged jet requirement.

Sample	Type 1	Type 2	Type 3	All type
Multijet	2.49 ± 1.74	7.34 ± 3.51	0.77 ± 4.94	10.60 ± 6.31
$Wb\bar{b}$	0.12 ± 0.03	0.31 ± 0.05	1.95 ± 0.14	2.38 ± 0.16
$Wc\bar{c}$	0.12 ± 0.08	1.15 ± 0.22	4.67 ± 0.45	5.94 ± 0.50
WNlp	1.32 ± 0.31	6.05 ± 0.71	22.28 ± 1.39	29.65 ± 1.59
$Z \to \mu\mu + b\bar{b}$	0.19 ± 0.03	0.79 ± 0.05	0.07 ± 0.02	1.06 ± 0.06
$Z \to \mu\mu + c\bar{c}$	0.25 ± 0.07	1.32 ± 0.17	0.29 ± 0.07	1.87 ± 0.19
$Z \to \mu\mu + N\text{lp}(15-60)$	0.09 ± 0.06	0.66 ± 0.18	0.47 ± 0.15	1.28 ± 0.24
$Z \to \mu\mu + N\text{lp}(60-130)$	2.89 ± 0.43	10.90 ± 0.85	2.14 ± 0.35	15.94 ± 1.01
$Z \to \mu\mu + N\text{lp}(130-250)$	0.10 ± 0.01	0.37 ± 0.02	0.04 ± 0.01	0.52 ± 0.02
$Z \to \tau\tau + b\bar{b}$	0.08 ± 0.01	0.53 ± 0.03	0.25 ± 0.02	0.86 ± 0.04
$Z \to \tau\tau + c\bar{c}$	0.10 ± 0.05	1.01 ± 0.17	0.55 ± 0.10	1.66 ± 0.20
$Z \to \tau\tau + N\text{lp}(15-60)$	0.07 ± 0.07	0.25 ± 0.10	0.22 ± 0.09	0.53 ± 0.15
$Z \to \tau\tau + N\text{lp}(60-130)$	1.58 ± 0.31	9.72 ± 0.92	4.58 ± 0.58	15.88 ± 1.13
$Z \to \tau\tau + N\text{lp}(130-250)$	0.05 ± 0.01	0.39 ± 0.02	0.20 ± 0.01	0.64 ± 0.03
WW	0.12 ± 0.02	0.66 ± 0.05	1.24 ± 0.07	2.02 ± 0.09
WZ	0.12 ± 0.03	0.36 ± 0.06	0.25 ± 0.05	0.73 ± 0.08
$t\bar{t} \to$ dilepton	0.79 ± 0.01	8.34 ± 0.04	2.98 ± 0.03	12.11 ± 0.05
$t\bar{t} \to$ lepton+jets	0.32 ± 0.02	2.18 ± 0.05	10.19 ± 0.12	12.69 ± 0.14
TOTAL	10.80 ± 1.86	52.34 ± 3.81	53.56 ± 5.21	116.69 ± 6.72
Data	15	37	52	104

variables in the muon+tau+jets sample with at least two jets. Appendix A shows more distributions of control variables, both in the one-jet exclusive and two-jets inclusive samples.

Table 5.8 shows that at the current selection stage, the expected contribution of $t\bar{t}$ event into the selected sample is about 20% of the sample composition. While there is already a hint of $t\bar{t}$ events in the sample, their significance is small. The last step in the analysis, $b-$tagging, is expected to reduce the contributions of background with light-flavor jets significantly, while retaining contributions of $t\bar{t}$ signal events. After applying $b-$tagging, it is expected that the sample will be dominated by top events. This will be discusssed in detail in the next chapter.

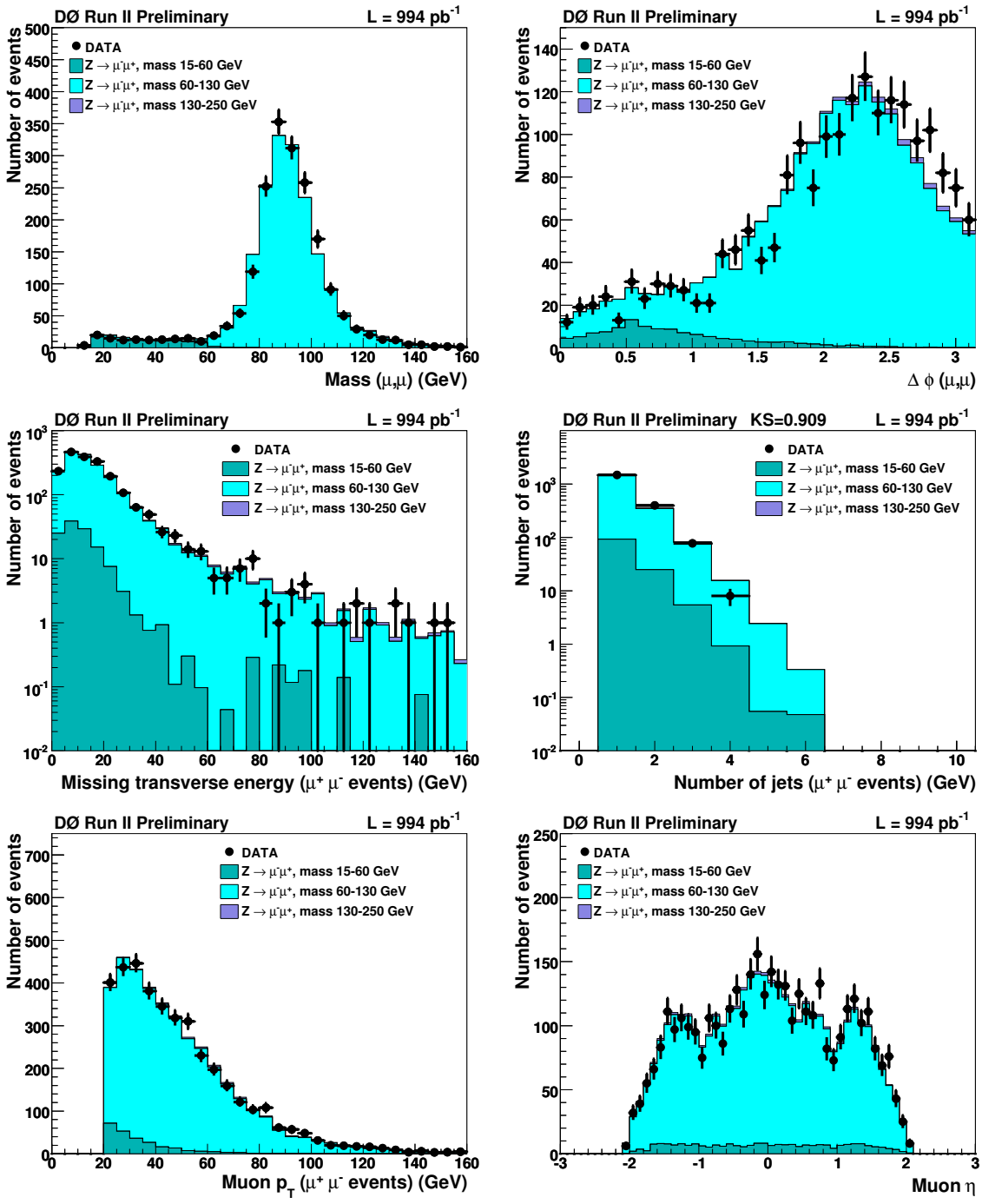

Figure 5.8: Distributions of control variables from normalization of $Z/\gamma \to \mu^-\mu^+$ by invariant mass template fit.

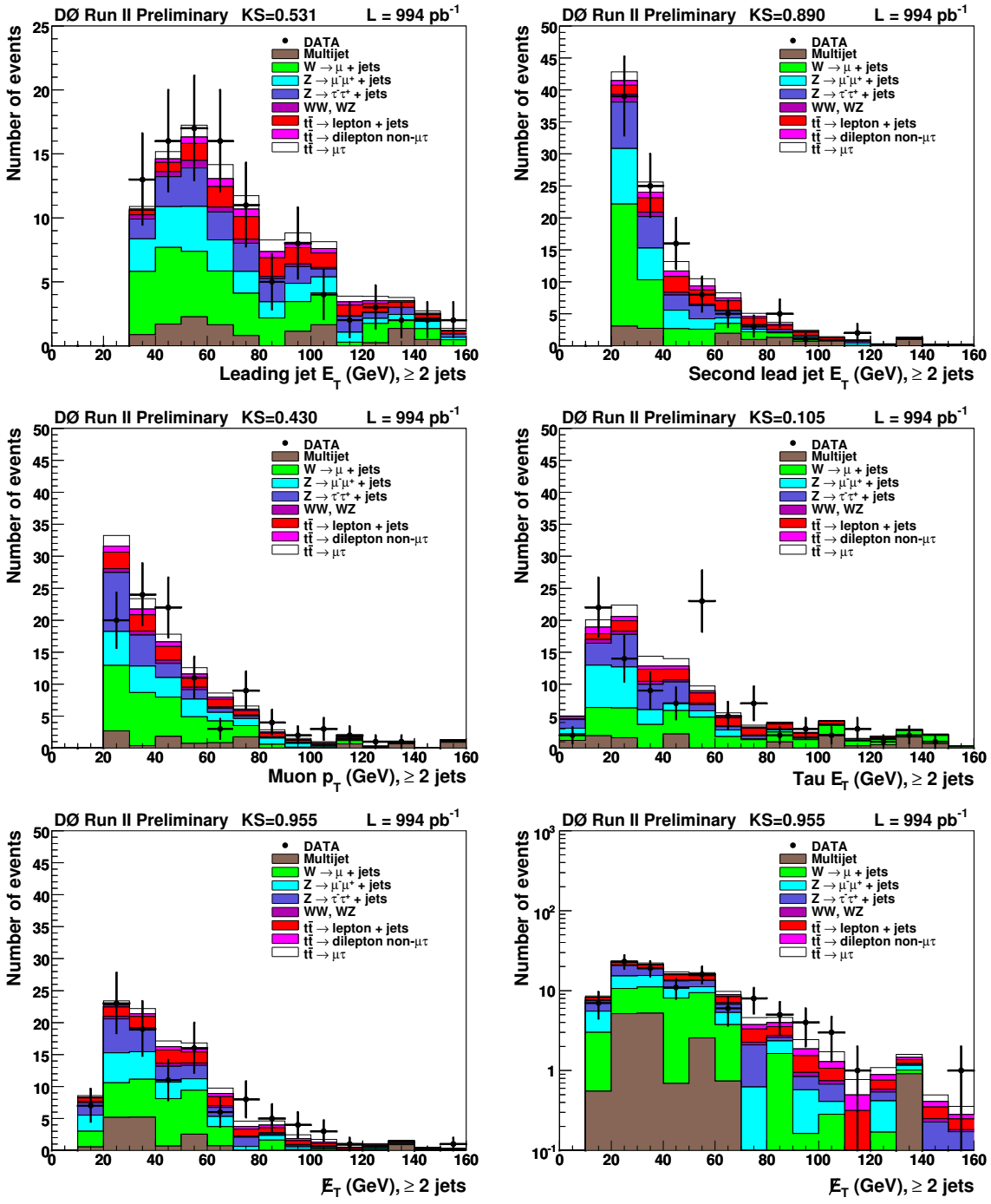

Figure 5.9: Distributions of control variables in the preselected muon+tau+jets sample (Part 1 of 2)

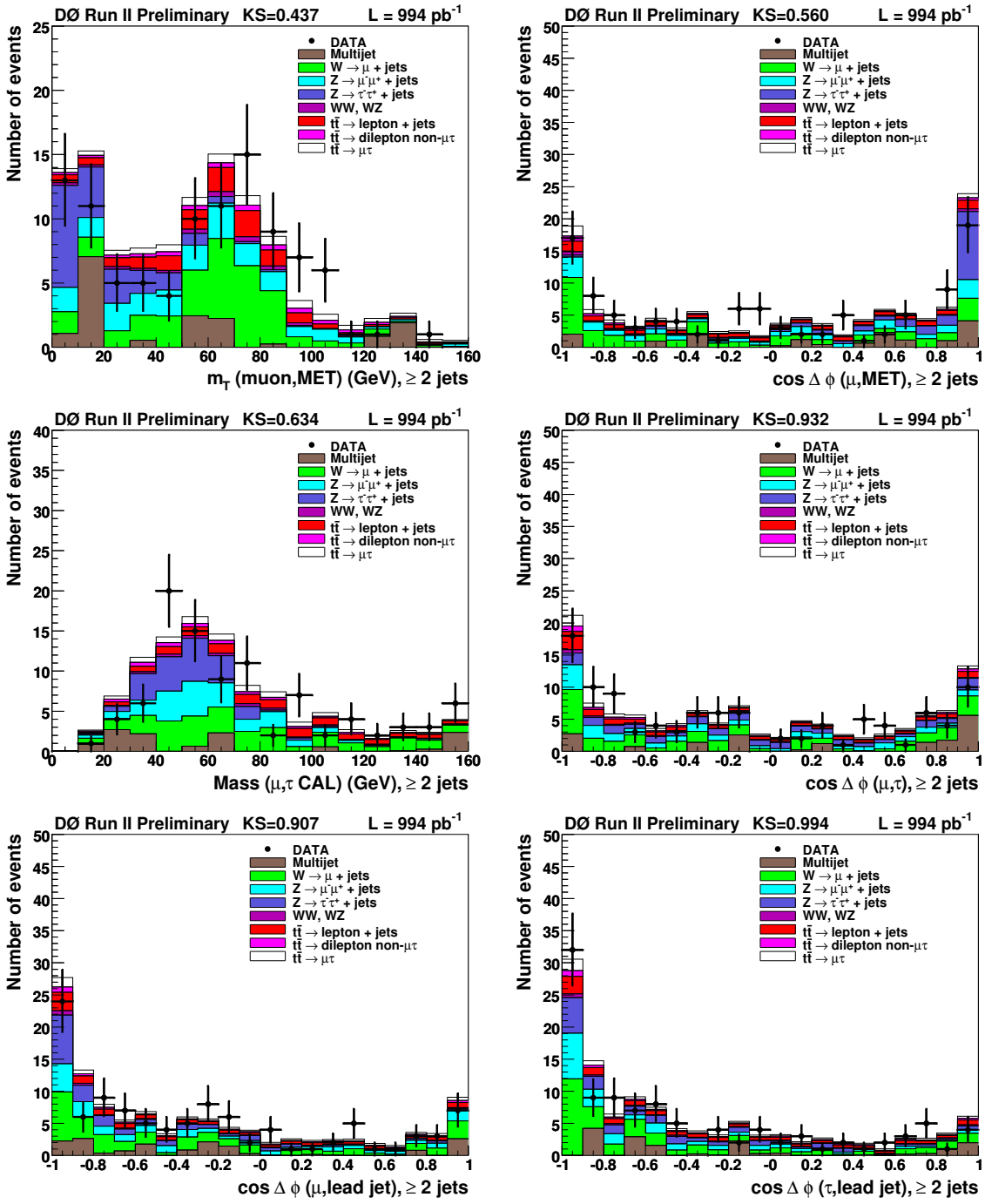

Figure 5.10: Distributions of control variables in the preselected muon+tau+jets sample (Part 2 of 2)

CHAPTER 6

MEASUREMENT OF $\boldsymbol{\sigma}\left(p\bar{p} \to t\bar{t}\right)$ AND $\boldsymbol{\sigma}\left(p\bar{p} \to t\bar{t}\right) \cdot \mathbf{BR}\left(t\bar{t} \to \mu\tau_h b\bar{b}\right)$

6.1 Estimation of $t\bar{t}$ Event Efficiency

As stated in Chapter 5, we use ALPGEN to model the $t\bar{t}$ signal events and estimate the efficiencies. As Table 5.8 shows, the expected contributions from $t\bar{t}$ in both inclusive dilepton final states and inclusive lepton+jets final states are roughly equal. We use both the dilepton sample and lepton+jets sample to estimate the inclusive $t\bar{t}$ efficiency. Here lepton means all three lepton flavors: e, μ, τ.

Table 6.1 and Table 6.2 list the selection criteria applied to the signal samples and the cumulative efficiency for each step. We use the SM branching ratio of top quark decay, as listed in Table 1.2, to combine the efficiencies for the two decay modes, giving the total efficiencies with respect to the $t\bar{t}$ initial state. Table 6.1 also lists the cumulative efficiency for dilepton samples with the exclusive final state $\mu\tau_h b\bar{b}$ only. The efficiency of this final state is of importance in looking for non-SM decay of top quarks.

Table 6.3 summarizes the efficiencies for both types of signal events, and shows the total efficiencies with respect to the $t\bar{t}$ initial state. After weighting with their respective branching ratios, the efficiency from $t\bar{t} \to$ lepton+jets is about the same size as the efficiency from $t\bar{t} \to$ dilepton.

6.2 Analysis of $b-$tagged Sample

The $b-$tagged sample is defined as the preselected muon+tau+jets sample with an additional requirement of the presence of one or more jets which are identified as a $b-$jet. In data events, we apply the $b-$tagging algorithm into every jet in the event. For each jet, the algorithm returns a binary value whether the jet is a $b-$jet or not. In Monte Carlo events, we first assign a probability to each jet in the event to be a $b-$jet. We then compute the probability for at least one jet in the

Table 6.1: Efficiency of muon+tau+jets selection cuts on $t\bar{t} \to$ dilepton and $t\bar{t} \to \mu\tau_h b\bar{b}$ generated by ALPGEN Monte Carlo.

Selection criteria	Cumulative efficiency $t\bar{t} \to$ dilepton inclusive	Cumulative efficiency $t\bar{t} \to \mu\tau_h b\bar{b}$
At least one jet with $p_T > 20$ GeV	0.9844 ± 0.0004	0.9909 ± 0.0012
Leading jet $p_T > 30$ GeV	0.9639 ± 0.0004	0.9753 ± 0.0012
No tight electron in central calorimeter	0.6395 ± 0.0006	0.9737 ± 0.0012
One or more loosely isolated muons with $p_T > 20$ GeV	0.2488 ± 0.0005	0.4392 ± 0.0015
Exactly one tightly isolated muon with $p_T > 20$ GeV	0.2101 ± 0.0005	0.4237 ± 0.0015
Veto second tightly isolated muon with $p_T > 15$ GeV	0.2054 ± 0.0005	0.4237 ± 0.0015
Veto on $Z-$window	0.1999 ± 0.0005	0.4232 ± 0.0015
Primary vertex ($\lvert z_{PV}\rvert < 60$ cm, number of tracks ≥ 3	0.1968 ± 0.0005	0.4177 ± 0.0015
Muon comes from primary vertex, $\lvert\Delta z(\mu, PV)\rvert < 1$ cm	0.1966 ± 0.0005	0.4172 ± 0.0015
MET cut, $15 < \not\!\!E_T < 200$ GeV	0.1866 ± 0.0005	0.3962 ± 0.0015
Trigger Efficiency	0.1525 ± 0.0004	0.3255 ± 0.0012
Muon ID correction factors	0.1386 ± 0.0004	0.2961 ± 0.0012
Loose tau (without NN cut)	0.1219 ± 0.0004	0.2673 ± 0.0011
Tight tau (NN cut)	0.0257 ± 0.0002	0.0931 ± 0.00076
Opposite sign muon-tau pair	0.0227 ± 0.0002	0.0868 ± 0.00074
Number of jets not matched to the tau ≥ 1	0.0225 ± 0.0002	0.0861 ± 0.00074
Leading jet $p_T > 30$ GeV	0.0222 ± 0.0002	0.0846 ± 0.00073
Two or more jets not matched to the tau	0.0175 ± 0.0001	0.0663 ± 0.00065
At least one $b-$tagged jet	0.0126 ± 0.0001	0.0481 ± 0.00031

event to be a $b-$jet. The probability can be

$$\begin{aligned} P(\text{at least one tag}) &= 1.0 - P(\text{zero tag}) \\ &= 1.0 - \prod_{j}^{\text{all jets}} P_j(\text{not tagged}) \end{aligned} \tag{6.1}$$

Multijet background contributions in the tagged sample are estimated using the same method discussed in Section 5.5.1, with the addition of the $b-$jet requirement. Table 6.4 lists the yield of $W+$jets and $t\bar{t}$ lepton+jets events in the same-sign (SS) data events, as well as the observed number of events in SS data. Nine events are found in the sS data sample.

Finally, in Table 6.5 we list the expected yields from the signal and background processes in the tagged sample. We find that the multijet process is the dominant background in the tagged sample, both in terms of magnitude and error. The principal source of error is the small size of the same-sign sample. As expected, the requirement of at least one $b-$jet in the sample reduced the contributions from $W + N$lp and $Z + N$lp significantly. The final selected, $b-$tagged sample now

Table 6.2: Efficiency of muon+tau+jets selection cuts on $t\bar{t} \rightarrow$ lepton+jets signal generated by ALPGEN Monte Carlo.

Selection criteria	Cumulative efficiency
At least one jet with $p_T > 20$ GeV	0.9958 ± 0.0005
Leading jet $p_T > 30$ GeV	0.9943 ± 0.0005
No tight electron in central calorimeter	0.8162 ± 0.0006
One or more loosely isolated muons with $p_T > 20$ GeV	0.1705 ± 0.0005
Exactly one tightly isolated muon with $p_T > 20$ GeV	0.1619 ± 0.0005
Veto second tightly isolated muon with $p_T > 15$ GeV	0.1619 ± 0.0005
Veto on $Z-$window	0.1618 ± 0.0005
Primary vertex ($\lvert z_{PV}\rvert < 60$ cm, number of tracks ≥ 3	0.1595 ± 0.0005
Muon comes from primary vertex, $\lvert\Delta z(\mu, PV)\rvert < 1$ cm	0.1594 ± 0.0005
MET cut, $15 < \not\!\!E_T < 200$ GeV	0.1498 ± 0.0005
Trigger Efficiency	0.1300 ± 0.0004
Muon ID correction factors	0.1183 ± 0.0004
Loose tau (without NN cut)	0.1116 ± 0.0004
Tight tau (NN cut)	0.00836 ± 0.00011
Opposite sign muon-tau pair	0.00449 ± 0.00008
Number of jets not matched to the tau ≥ 1	0.00448 ± 0.00008
Leading jet $p_T > 30$ GeV	0.00448 ± 0.00008
Two or more jets not matched to the tau	0.00414 ± 0.00008
At least one $b-$tagged jet	0.00274 ± 0.00001

Table 6.3: Efficiencies of the muon+tau+jets selection for $t\bar{t}$ dilepton and $t\bar{t}$lepton+jets sample, and the total efficiencies for $t\bar{t} \rightarrow$ inclusive sample.

Processes	Efficiency ϵ	Branching ratio BR	$\epsilon \times BR$
$t\bar{t} \rightarrow$ dilepton	0.01266 ± 0.0001	0.10608	0.001304 ± 0.000015
$t\bar{t} \rightarrow$ lepton+jets	0.00274 ± 0.0001	0.43924	0.001247 ± 0.000027
$t\bar{t} \rightarrow$ inclusive			0.002551 ± 0.000031

is dominated by top quark events.

Figure 6.1 shows some distributions in the tagged sample. Due to the poor statistics, we chose to check kinematics of individual physics object and variables which describes $t\bar{t}$ events, such as H_T (the sum of transverse energy of all physics object in the event). Appendix A has a more exhaustive set of distributions in the $b-$tagged sample.

Table 6.4: Observed same-sign (SS) events in data at the tagged level, and the expected number of W+jets and $t\bar{t}$ lepton+jets events to be subtracted from SS data to get estimation of multijet background in the opposite sign (OS) sample. Notice the large statistical error on the SS data sample due to small statistics.

Sample	Type 1	Type 2	Type 3	All type
SS data	1 ± 1.00	1 ± 1.00	7 ± 2.65	9 ± 3.00
SS $t\bar{t} \rightarrow$ dilepton	-0.00 ± 0.00	-0.04 ± 0.00	-0.12 ± 0.01	-0.16 ± 0.01
SS $t\bar{t} \rightarrow$ lepton+jets	-0.04 ± 0.01	-0.33 ± 0.02	-2.72 ± 0.06	-3.09 ± 0.07
SS $Wb\bar{b}$	-0.01 ± 0.01	-0.05 ± 0.02	-0.36 ± 0.05	-0.42 ± 0.06
SS $Wc\bar{c}$	-0.02 ± 0.01	-0.04 ± 0.02	-0.42 ± 0.07	-0.48 ± 0.07
SS WNlp	-0.00 ± 0.00	-0.08 ± 0.02	-0.24 ± 0.02	-0.32 ± 0.02
TOTAL	0.92 ± 1.00	0.45 ± 1.00	3.15 ± 2.65	4.52 ± 3.001

6.3 Cross-section Extraction

The small size of the $b-$tagged sample suggests using a counting method to extract the cross section. One can relate the observed number of events to the cross-section by

$$\sigma_{t\bar{t}} = \frac{N_{\text{observed}} - N_{\text{expected background}}}{\epsilon \times \mathcal{L}}, \tag{6.2}$$

where ϵ is the efficiency for inclusive $t\bar{t}$ events and $\mathcal{L}$ is total amount of integrated luminosity in the data sample.

However, as discussed in Sec. 5.5.1 we subtract same-sign top events in the multijet background estimate which creates a circular dependence: the number of background events requires knowledge of the $t\bar{t}$ production cross-section. It is possible to extract the cross-section with exact treatment of the $t\bar{t}$ cross-section for both the opposite-sign and the same-sign sample.

We begin by writing down the contributions of various processes into the opposite-sign (OS) and same-sign sample (SS).

$$N_{DATA}^{OS} = N_{t\bar{t}}^{OS} + N_{W}^{OS} + N_{Z}^{OS} + N_{Diboson}^{OS} + N_{Multijet}^{OS} \tag{6.3}$$

$$N_{DATA}^{SS} = N_{t\bar{t}}^{SS} + N_{W}^{SS} + N_{Multijet}^{SS} \tag{6.4}$$

If we use the following two assumptions

- The contribution from Z+jets and diboson production to the same-sign sample are small;
- The contribution from multijet events to the opposite-sign and same-sign sample are equal;

Table 6.5: Estimated and observed yield for various component in the OS sample with at least two jets and at least one $b-$tagged jet requirement.

Sample	Type 1	Type 2	Type 3	All type
Multijet	0.92 ± 1.00	0.45 ± 1.00	3.15 ± 2.65	4.52 ± 3.01
$Wb\bar{b}$	0.05 ± 0.02	0.12 ± 0.03	0.85 ± 0.09	1.02 ± 0.18
$Wc\bar{c}$	0.01 ± 0.01	0.16 ± 0.04	0.54 ± 0.07	0.71 ± 0.13
WNlp	0.03 ± 0.02	0.11 ± 0.01	0.44 ± 0.03	0.58 ± 0.03
$Z \to \mu\mu + b\bar{b}$	0.09 ± 0.02	0.42 ± 0.04	0.03 ± 0.01	0.54 ± 0.10
$Z \to \mu\mu + c\bar{c}$	0.03 ± 0.01	0.18 ± 0.02	0.03 ± 0.01	0.24 ± 0.05
$Z \to \mu\mu + N$lp$(15-60)$	0.00 ± 0.00	0.01 ± 0.00	0.01 ± 0.00	0.02 ± 0.00
$Z \to \mu\mu + N$lp$(60-130)$	0.05 ± 0.01	0.20 ± 0.01	0.03 ± 0.00	0.28 ± 0.02
$Z \to \mu\mu + N$lp$(130-250)$	0.00 ± 0.00	0.01 ± 0.00	0.00 ± 0.00	0.01 ± 0.00
$Z \to \tau\tau + b\bar{b}$	0.04 ± 0.01	0.30 ± 0.02	0.13 ± 0.01	0.46 ± 0.08
$Z \to \tau\tau + c\bar{c}$	0.01 ± 0.01	0.16 ± 0.03	0.07 ± 0.01	0.23 ± 0.05
$Z \to \tau\tau + N$lp$(15-60)$	0.00 ± 0.00	0.00 ± 0.00	0.00 ± 0.00	0.01 ± 0.00
$Z \to \tau\tau + N$lp$(60-130)$	0.03 ± 0.00	0.19 ± 0.01	0.09 ± 0.01	0.31 ± 0.02
$Z \to \tau\tau + N$lp$(130-250)$	0.00 ± 0.00	0.01 ± 0.00	0.00 ± 0.00	0.01 ± 0.00
WW	0.01 ± 0.00	0.04 ± 0.01	0.10 ± 0.01	0.14 ± 0.01
WZ	0.01 ± 0.00	0.02 ± 0.00	0.04 ± 0.01	0.07 ± 0.01
Background total	1.29 ± 1.00	2.36 ± 1.00	5.51 ± 2.65	9.16 ± 3.01
$t\bar{t} \to$ dilepton	0.58 ± 0.01	6.13 ± 0.04	2.07 ± 0.02	8.78 ± 0.04
$t\bar{t} \to$ lepton+jets	0.22 ± 0.02	1.51 ± 0.04	6.68 ± 0.09	8.40 ± 0.11
Background total + expected $t\bar{t}$	2.08 ± 1.00	10.00 ± 1.01	14.26 ± 2.66	26.34 ± 3.01
Data	2	15	12	29

then we have two equations with two unknowns: $t\bar{t}$ cross-section $\sigma_{t\bar{t}}$ and contribution from multijet processes $N^{OS}_{Multijet} = N^{SS}_{Multijet}$. Solving for $\sigma_{t\bar{t}}$, we obtain

$$\sigma_{t\bar{t}} \quad = \quad \frac{N^{OS}_{DATA} - N^{SS}_{DATA} - \left(N^{OS}_{W} - N^{SS}_{W}\right) - N^{OS}_{Z} - N^{OS}_{Diboson}}{\left(\epsilon^{OS}_{t\bar{t}} - \epsilon^{SS}_{t\bar{t}}\right) \cdot \mathcal{L}} \tag{6.5}$$

where we have rewritten $N^{OS/SS}_{t\bar{t}} = \sigma_{t\bar{t}} \epsilon^{OS/SS}_{t\bar{t}} \mathcal{L}$.

Table 6.6 shows the efficiencies for $t\bar{t}$ dilepton and lepton+jets sample with requirements of a same-sign lepton-tau pair. Using the $t\bar{t}$ efficiencies from Table 6.3 and 6.6, and the expected yield from Table 6.4 and Table 6.5, we measure the $t\bar{t}$ cross-section to be:

$$\sigma_{t\bar{t}} = 8.0^{+2.8}_{-2.4}(\text{stat}). \tag{6.6}$$

The statistical error on the cross-section is calculated by varying the data yield by $\pm$ one standard deviation, assuming a Poisson fluctuation, and then recomputing the cross-section with equation 6.5.

Table 6.6: Efficiencies of the muon+tau+jets selection with same-sign muon-tau pair for $t\bar{t}$ dilepton and $t\bar{t}$lepton+jets sample, and the total efficiencies for $t\bar{t} \rightarrow$ inclusive sample.

Processes	Efficiency ϵ	Branching ratio BR	$\epsilon \times BR$
$t\bar{t} \rightarrow$ dilepton, same-sign	0.000238 ± 0.000002	0.10608	0.000025 ± 0.000002
$t\bar{t} \rightarrow$ lepton+jets, same-sign	0.001007 ± 0.000022	0.43924	0.000459 ± 0.000020
$t\bar{t} \rightarrow$ inclusive			0.000484 ± 0.000020

6.4 Measurement of $\boldsymbol{\sigma}(p\bar{p} \rightarrow t\bar{t}) \cdot \mathbf{BR}(t\bar{t} \rightarrow \mu\tau_h b\bar{b})$

While the previous sections measured the top pair production cross section in events with a reconstructed tau, many of those tau candidates arose from jet or lepton fakes. In this section we measure the cross-section times branching ratio for muon+tau events with a real hadronic tau.

We measure the cross section times branching ratio so that we don't need to make any assumptions about either the cross section or branching ratio. By comparing this measurement with standard model expectations, we can look for deviations which might indicate new physics (such as a $t \rightarrow H^+ b$ decay mode).

For this part of the analysis, we divide the top pair production into two types of events: one that represents our final state (muon + hadronic tau + $2b$ + 2ν at the parton level) and one that includes all other top quark pair events passing our criteria. We use a filter to select Monte Carlo $t\bar{t}$ events in which the top quark pair decays into our final state. final state. The other set is found by subtracting this sample from the total dilepton sample and adding in the ℓ+jets events. The events in the second category are included in the background estimate. The standard model cross-section for $t\bar{t}$ production and the standard model branching ratio for top quark decay is assumed for the second type of events.

With the efficiency of $t\bar{t} \rightarrow \mu\tau_h b\bar{b}$ as shown in Table 6.1, we obtained

$$\sigma(t\bar{t}) \times BR(t\bar{t} \rightarrow \mu + \tau + 2b + 2\nu) = 0.18 \pm 0.13 \tag{6.7}$$

The expected SM value is

$$\sigma_{SM}(t\bar{t}) \times BR_{SM}(t\bar{t} \rightarrow \mu + \tau + 2b + 2\nu) = 6.77 \times 0.0186 = 0.126 \tag{6.8}$$

Table 6.7: Summary of statistical uncertainties on each of the sources of events in the $\mu\tau$ channel. The SM cross section is used for $t\bar{t}$ production.

	# of Events	Statistical uncertainty
W (OS)	2.31	$\pm$0.13
W (SS)	$-$1.22	$\pm$0.09
$Z \to \mu\mu$	1.09	$\pm$0.05
$Z \to \tau\tau$	1.20	$\pm$0.06
diboson	0.21	$\pm$0.07
$t\bar{t}$ →dilepton (OS)	8.78	$\pm$0.04
$t\bar{t}$ →dilepton (SS)	$-$0.16	$\pm$0.01
$t\bar{t} \to \ell$+jets (OS)	8.40	$\pm$0.11
$t\bar{t} \to \ell$+jets (SS)	$-$3.09	$\pm$0.07
SS data	9	$\pm$3

6.5 Systematic Uncertainties

Numerous factors contribute to systematic uncertainties in the cross section measurement. This section describes the various factors, estimates of their uncertainty and the resulting uncertainty on the final measurement. Many of these uncertainties are based on numerous studies performed by various members of the DØ collaboration. We take a conservative approach by assuming all systematic uncertainties to be completely uncorrelated.

The considered systematics include:

- **Data quality:** the data quality correction factor has been previously measured to be 0.97 $\pm$ 0.005 [51], therefore a $\pm$0.5% uncertainty is evaluated for all MC samples.

- **Primary vertex selection:** the uncertainty in primary vertex selection between data and MC is taken from [64]. A value of $\pm$3.0% is assigned as systematic error for this.

- **Vertex z simulation:** the uncertainty due to difference in z vertex simulation from data is taken from [64]. A value of $\pm$2.2% is assigned as systematic error for this.

- **MC luminosity profile:** this uncertainty arises from differences in the luminosity profile of the zerobias overlay events used in MC compared to the data sample. The value is $\pm$0.5% for Monte Carlo $t\bar{t}$ sample and $\pm$2.0% for other Monte Carlo samples [64].

- **Muon identification:** the systematic uncertainty on muon identification are estimated to be $\pm 0.7\%$ in the muon certification documentation [33].

- **Muon track:** the systematic errors on muon track reconstruction are estimated to be $\pm 0.7\%$ in the muon certification documentation [33].

- **Muon isolation:** we use an estimate from the single top analysis, which is $\pm 2.0\%$.

- **Muon trigger:** the uncertainty on muon trigger efficiency is taken from the lepton+jets analysis [65], by calculating the percent systematic error listed in Table 39. The value is found to be very close to zero, and we decided to assign a zero value.

- **Jet trigger:** the uncertainty on jet triggers in the μ+jets triggers are taken from the lepton+jets analysis [65]. The value is $\pm 0.3\%$.

- **Tau reconstruction:** the uncertainty in the data/MC agreement with respect to tau reconstruction is taken from the $H \to \tau\tau$ analysis [66]. The assigned value is $\pm 3\%$.

- **Jet-tau fake rate:** the data/MC correction factor for jets faking taus was measured to be 1.04 ± 0.08 as described in Section 5.4.1. An 8% uncertainty is applied to the W, $Z \to \mu\mu(ee)$, and $t\bar{t} \to \ell$ + jets.

- **K-factor:** we assign an uncertainty of 0.1 on the K factor for both W ($k = 1.6$, Sec. 5.3.3) and Z ($k = 1.23$, Sec. 5.5.2) by comparison with data.

- **HF K-factor:** we use the uncertainties described in Sec. 5.2.2 scaled to the appropriate fraction of events that contain heavy flavor.

- **Tag rate function:** this uncertainty is evaluated by shifting the value of the tagging probability (Sec. 3.6.2) for each jet by ($\pm 1\sigma$) from the central value of the tag rate function.

- **Jet energy scale:** this uncertainty is evaluated by shifting the jet energy scale in the JSSR processor by ($\pm 1\sigma$).

- **Jet energy resolution:** this uncertainty is evaluated by shifting the jet energy correction by ($\pm 1\sigma$).

- **NLO $t\bar{t}$ cross-section:** this uncertainty is evaluated by shifting the NLO $t\bar{t}$ cross-section by ($\pm 1\sigma$). This uncertainty is only considered for measurement of $\boldsymbol{\sigma}\left(p\bar{p} \to t\bar{t}\right) \cdot \mathbf{BR}\left(t\bar{t} \to \mu\tau_h b\bar{b}\right)$.

- **Background Statistics:** an uncorrelated combination of the statistical error on the Monte Carlo and same-sign data contributions to the background (for the individual component statistical errors see Tables 6.7).

Table 6.8 lists the various sources of systematic uncertainties and their contributions to the uncertainty on the cross-section and $\sigma \times BR$.

The values and uncertainties for the cross-section and $\sigma \times BR$ after inclusion of systematic uncertainties are:

$$\sigma(t\bar{t}) = 8.0^{+2.8}_{-2.4}\,(\text{stat})^{+1.8}_{-1.7}\,(\text{syst}) \pm 0.5\,(\text{lumi})\ \text{pb} \quad (6.9)$$

$$\sigma(t\bar{t}) \times BR(t\bar{t} \to \mu + \tau + 2\nu + 2b) = 0.18^{+0.13}_{-0.11}\,(\text{stat})^{+0.09}_{-0.09}\,(\text{syst}) \pm 0.01\,(\text{lumi})\ \text{pb}. \quad (6.10)$$

6.6 Combinations with the electron+tau channel

The electron+tau analysis bears many similarities with the muon+tau analysis in the sense that both channels have one lepton and one tau in the final states. Analysis in the electron+tau channel has been performed in parallel, and the results are:

$$\sigma(t\bar{t}) = 8.6^{+3.1}_{-2.6}\,(\text{stat})^{+1.6}_{-1.6}\,(\text{syst}) \pm 0.5\,(\text{lumi})\ \text{pb}, \quad (6.11)$$

$$\sigma(t\bar{t}) \times BR(t\bar{t} \to e + \tau + 2\nu + 2b) = 0.19^{+0.12}_{-0.10}\,(\text{stat})^{+0.07}_{-0.07}\,(\text{syst}) \pm 0.01\,(\text{lumi})\ \text{pb}. \quad (6.12)$$

A combination of the results in the muon+tau and electron+tau channel has been done [67]. The combination is done by minimizing the sum of the negative log-likelihood functions for the two channel. The likelihood for an individual channel is based on the Poisson probability of observing a number of events (N_j^{obs}) given the luminosity ($\mathcal{L}_j$), branching fraction (BR_j), efficiency (ϵ_j) and a number of background events (N_j^{bkg}),

$$rmL(\sigma_j, \{N_j^{obs}, N_j^{bkg}, BR_j, \mathcal{L}_j, \varepsilon_j\}) = \mathcal{P}(N_j^{obs}, \mu_j) = \frac{\mu^{N_j^{obs}}}{N_j^{obs}!} e^{-\mu_j}. \quad (6.13)$$

More details of the method can be found in Reference [68].

The combined results of $\mu\tau$ and $e\tau$ are:

$$\sigma(t\bar{t}) = 8.3^{+2.0}_{-1.8}\,(\text{stat})^{+1.4}_{-1.2}\,(\text{syst}) \pm 0.5\,(\text{lumi})\ \text{pb}, \quad (6.14)$$

(combined)

$$\sigma(t\bar{t}) \times BR(t\bar{t} \to \ell + \tau + 2\nu + 2b) = 0.19^{+0.08}_{-0.08}\,(\text{stat})^{+0.07}_{-0.07}\,(\text{syst}) \pm 0.01\,(\text{lumi})\ \text{pb}. \quad (6.15)$$

(combined)

Figure 6.2 shows a comparison of DØ results of $t\bar{t}$ cross-section measurements in the different channels as of Summer 2007, with the results in the combined $\mu\tau$ and $e\tau$ channels included.

6.7 Conclusions and Outlook

We have performed the first DØ Run 2 top pair production cross-section analysis dedicated to a dilepton state with a muon and a hadronic tau decay. By selecting events with an isolated muon, a hadronic tau, two or more jets (at least one of which is b-tagged) and missing transverse energy, we find that about two thirds of the events are expected to be top quark candidates.

We measured a top pair production cross-section of $8.0\ ^{+2.8}_{-2.4}$ (stat) $^{+1.8}_{-1.7}$ (syst) $\pm$ 0.5 (lumi) pb We also measured the cross section times branching ratio to be $0.18\ ^{+0.13}_{-0.11}$ (stat) $^{+0.09}_{-0.09}$ (syst) $\pm$ 0.01 (lumi) pb.

In conclusion, we show that it is possible to do an analysis involving the decay of a top quark into a tau lepton in hadronic decay modes. We outlined a general analysis strategy and identified the principal source of backgrounds. We pointed out the limitations of the current analysis and made suggestions about how to overcome them. In the future, it will be interesting to improve the analysis with the following things:

- An increase in the amount of data.
- An increase in triggering and selection efficiency.
- Use of an advanced analysis method, especially involving multivariate methods.

The Fermilab Tevatron is expected to continue its current data-taking run until the year of 2009. A possible plan to extend the Tevatron running period until 2010 is under consideration. With the currently stable operational status, the Fermilab Tevatron is likely to be the most feasible place to perform a dedicated search for the decay $t \to \tau\nu b$ in the next two or three years. While the Large Hadron Collider (LHC) offers a higher rate of top quark production, the much larger background from multijet events is expected to make hadronic tau identification at the LHC more difficult compared to the Tevatron.

Within the current rate of data accumulated by DØ, it is possible to have an observation of direct top quark decay into a tau lepton with a 3σ confidence level. The time will then be open for deeper analyses into the nature of the third generation.

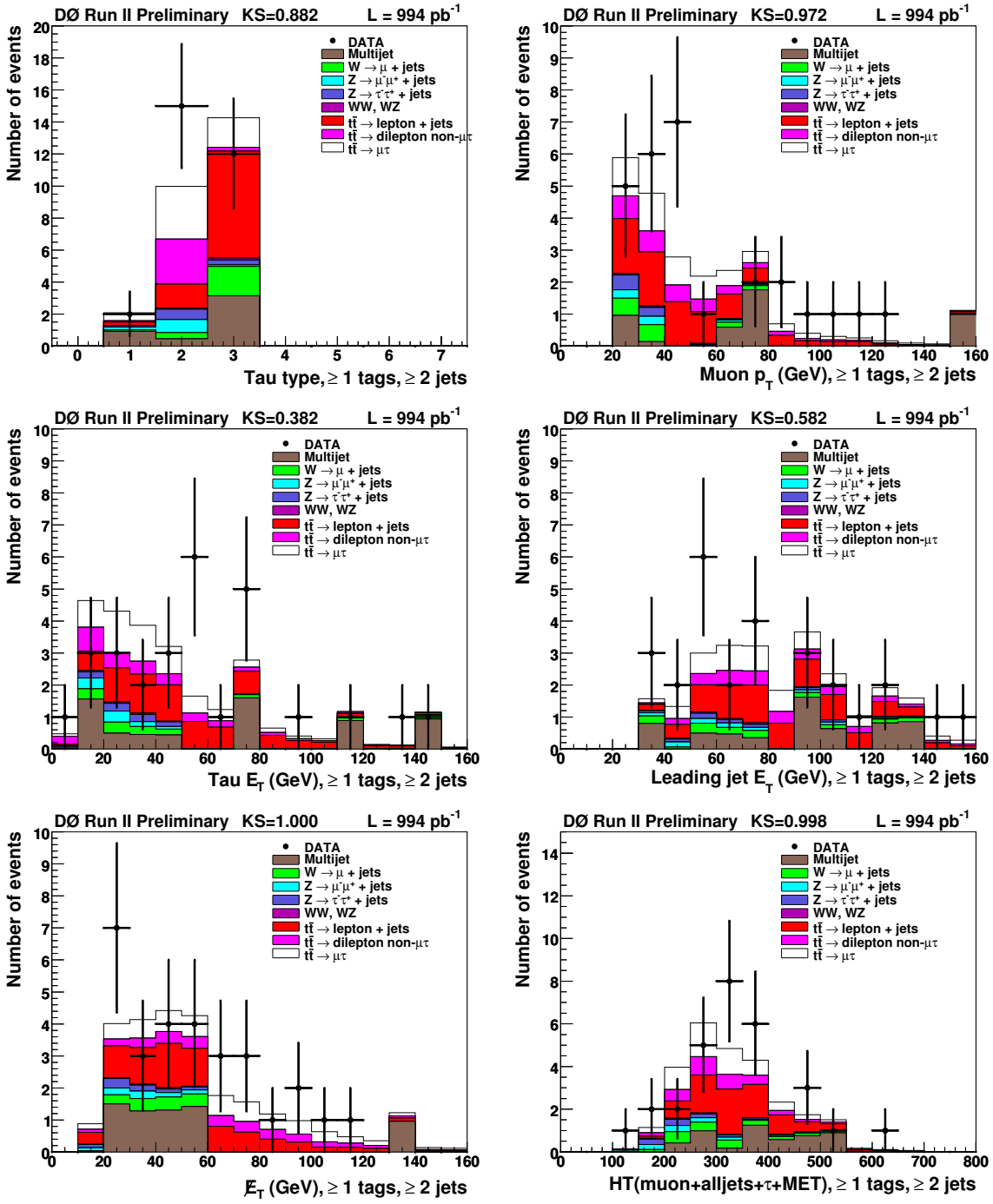

Figure 6.1: Plots of some distributions in the sample with at least two jets one of which is b-tagged.

Table 6.8: Relative systematics for the various Monte Carlo samples.

	$t\bar{t} \to 2\ell 2\nu 2b$, %		$t\bar{t} \to \ell$+jets, %		W, %		$Z \to \mu\mu$, %		$Z \to \tau\tau$, %		$WW + WZ$, %		Total, pb		$\sigma \times BR$, pb	
Source of uncertainty	up	down	up	down	up	down	up	down	up	down	up	down	up	down	up	down
Data quality	+0.50	−0.50	+0.50	−0.50	+0.50	−0.50	+0.50	−0.50	+0.50	−0.50	+0.50	−0.50	+0.05	−0.05	+0.003	−0.003
Primary vertex selection	+0.00	−3.00	+0.00	−3.00	+0.00	−3.00	+0.00	−3.00	+0.00	−3.00	+0.00	−3.00	+0.29	−0.00	+0.016	−0.000
Vertex z simulation	+2.20	−2.20	+2.20	−2.20	+2.20	−2.20	+2.20	−2.20	+2.20	−2.20	+2.20	−2.20	+0.21	−0.20	+0.012	−0.011
Luminosity profile	+0.50	−0.50	+0.50	−0.50	+2.00	−2.00	+2.00	−2.00	+2.00	−2.00	+2.00	−2.00	+0.06	−0.06	+0.003	−0.003
Muon ID	+0.70	−0.70	+0.70	−0.70	+0.70	−0.70	+0.70	−0.70	+0.70	−0.70	+0.70	−0.70	+0.06	−0.06	+0.003	−0.003
Muon track	+0.70	−0.70	+0.70	−0.70	+0.70	−0.70	+0.70	−0.70	+0.70	−0.70	+0.70	−0.70	+0.06	−0.06	+0.003	−0.003
Muon isolation	+2.00	−2.00	+2.00	−2.00	+2.00	−2.00	+2.00	−2.00	+2.00	−2.00	+2.00	−2.00	+0.19	−0.18	+0.001	−0.001
Muon trigger	+2.50	−2.50	+2.50	−2.50	+2.50	−2.50	+2.50	−2.50	+2.50	−2.50	+2.50	−2.50	+0.24	−0.23	+0.014	−0.013
Jet trigger	+0.20	−0.20	+0.20	−0.20	+0.20	−0.20	+0.20	−0.20	+0.20	−0.20	+0.20	−0.20	+0.02	−0.02	+0.001	−0.001
Tau reconstruction	+3.00	−3.00	+0.00	−0.00	+0.00	−0.00	+0.00	−0.00	+3.00	−3.00	+3.00	−3.00	+0.16	−0.15	+0.006	−0.006
Jet-tau fake rate	+0.00	−0.00	+11.00	−11.00	+11.00	−11.00	+11.00	−11.00	+0.00	−0.00	+11.00	−11.00	+0.48	−0.44	+0.034	−0.036
K-factor	+0.00	−0.00	+0.00	−0.00	+6.25	−6.25	+8.10	−8.10	+8.10	−8.10	+0.00	−0.00	+0.08	−0.08	+0.004	−0.004
HF K-factor	+0.00	−0.00	+0.00	−0.00	+10.00	−10.00	+10.80	−10.80	+10.00	−10.00	+0.00	−0.00	+0.16	−0.16	+0.008	−0.008
Tag rate function	+3.30	−4.00	+3.30	−4.50	+5.90	−5.40	+6.40	−5.50	+4.90	−4.90	+4.80	−4.80	+0.31	−0.34	+0.025	−0.019
Jet energy scale	+1.00	−3.30	+0.10	−2.40	+24.90	−16.90	+14.70	−12.00	+14.70	−10.80	+9.50	−42.90	+0.30	−0.50	+0.029	−0.022
Jet energy resolution	+0.40	−0.20	−0.80	−0.80	−9.30	+0.40	+0.90	−1.80	+0.00	−0.00	+0.00	−0.00	+0.02	−0.06	+0.007	−0.007
NLO $t\bar{t}$ cross section	+0.09	−0.09	+0.09	−0.09											+0.027	−0.026
Subtotal	+6.84	−7.25	+12.60	−12.80	+32.10	−24.40	+24.30	−22.80	+21.10	−18.30	+16.50	−44.90	+0.84	−0.87	+0.065	−0.059
Background statistics													+1.46	−1.46	+0.066	−0.066

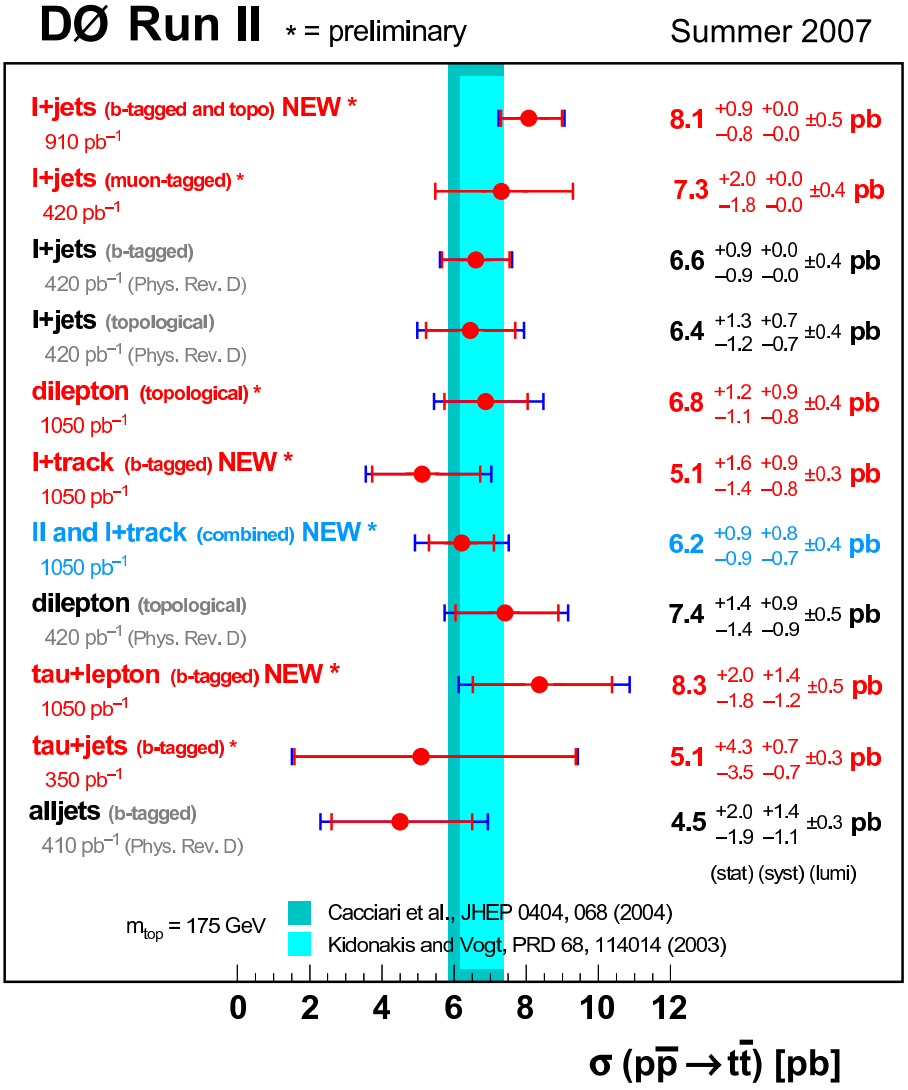

Figure 6.2: Summary of DØ measurements of $t\bar{t}$ cross-section at the Tevatron in various channels as of Summer 2007 [7].

APPENDIX A

CONTROL PLOTS

A.1 One-jet exclusive sample

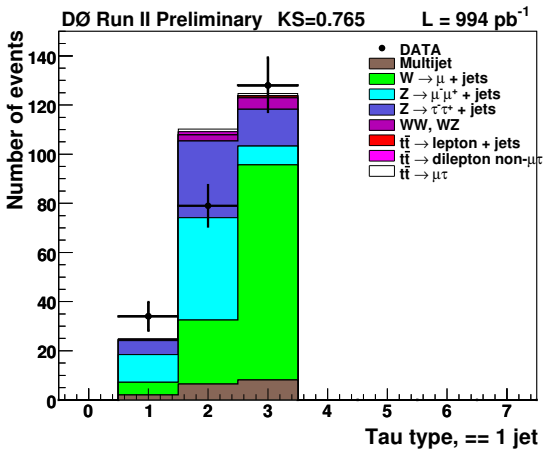

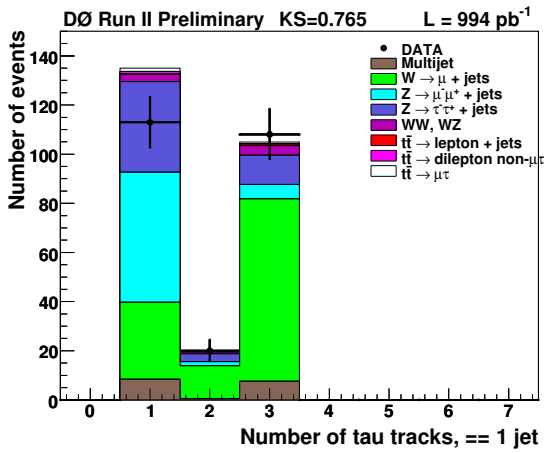

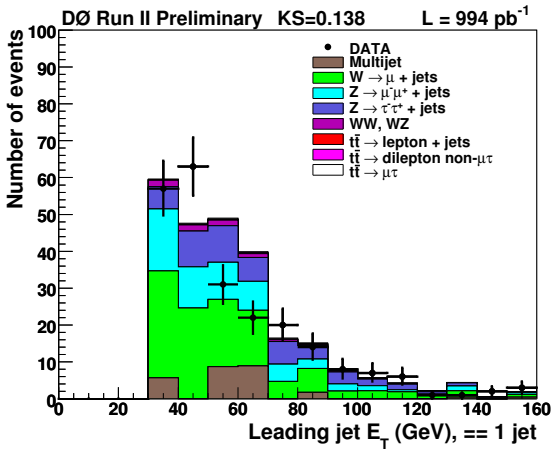

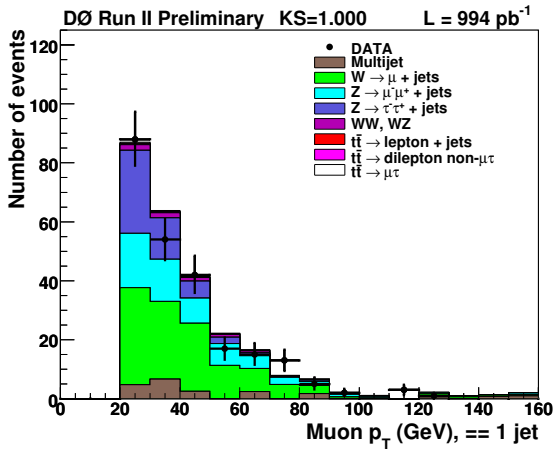

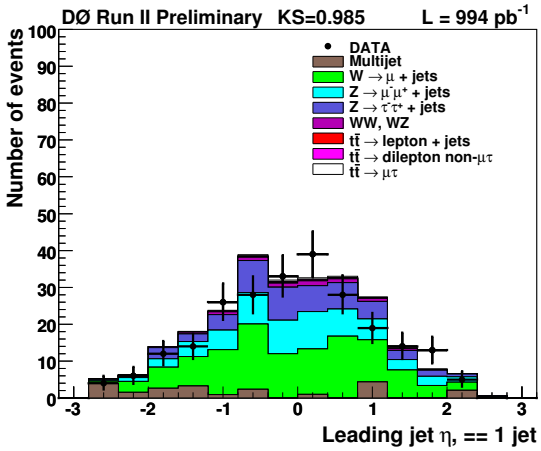
DØ Run II Preliminary KS=0.985 L = 994 pb-1
DATA
Multijet
W → μ + jets
Z → μ-μ+ + jets
Z → τ-τ+ + jets
WW, WZ
tt̄ → lepton + jets
tt̄ → dilepton non-μτ
tt̄ → μτ
Number of events
Leading jet η, == 1 jet

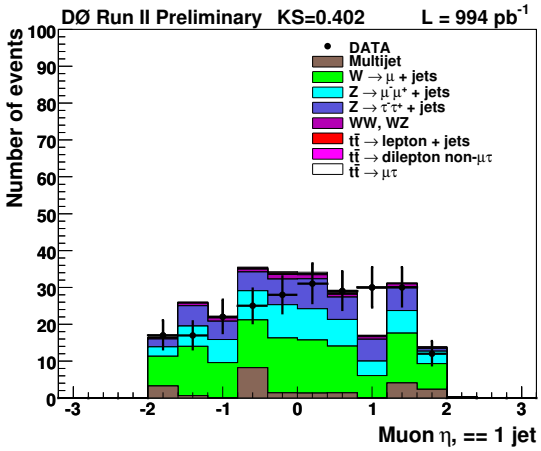
DØ Run II Preliminary KS=0.402 L = 994 pb-1
DATA
Multijet
W → μ + jets
Z → μ-μ+ + jets
Z → τ-τ+ + jets
WW, WZ
tt̄ → lepton + jets
tt̄ → dilepton non-μτ
tt̄ → μτ
Number of events
Muon η, == 1 jet

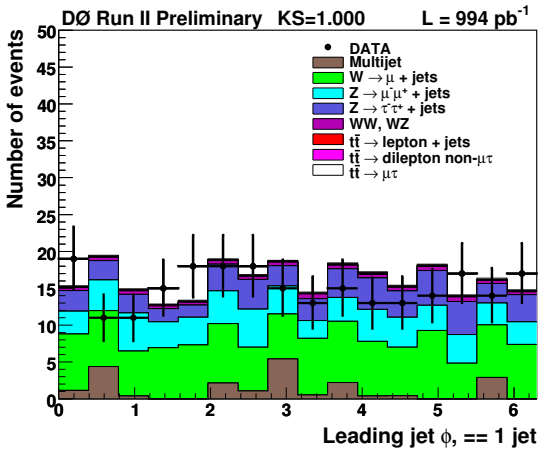
DØ Run II Preliminary KS=1.000 L = 994 pb-1
DATA
Multijet
W → μ + jets
Z → μ-μ+ + jets
Z → τ-τ+ + jets
WW, WZ
tt̄ → lepton + jets
tt̄ → dilepton non-μτ
tt̄ → μτ
Number of events
Leading jet φ, == 1 jet

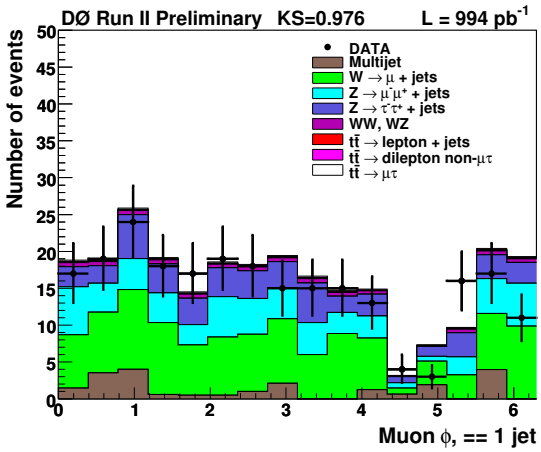
DØ Run II Preliminary KS=0.976 L = 994 pb-1
DATA
Multijet
W → μ + jets
Z → μ-μ+ + jets
Z → τ-τ+ + jets
WW, WZ
tt̄ → lepton + jets
tt̄ → dilepton non-μτ
tt̄ → μτ
Number of events
Muon φ, == 1 jet

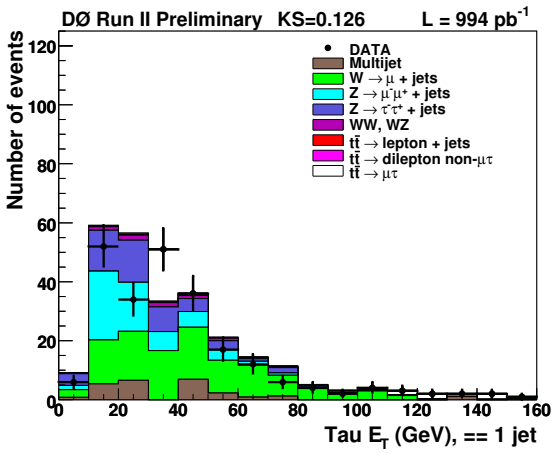
DØ Run II Preliminary KS=0.126 L = 994 pb-1
DATA
Multijet
W → μ + jets
Z → μ-μ+ + jets
Z → τ-τ+ + jets
WW, WZ
tt̄ → lepton + jets
tt̄ → dilepton non-μτ
tt̄ → μτ
Number of events
Tau ET (GeV), == 1 jet

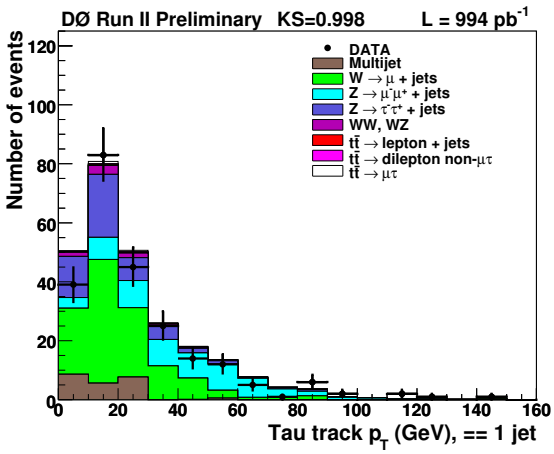
DØ Run II Preliminary KS=0.998 L = 994 pb-1
DATA
Multijet
W → μ + jets
Z → μ-μ+ + jets
Z → τ-τ+ + jets
WW, WZ
tt̄ → lepton + jets
tt̄ → dilepton non-μτ
tt̄ → μτ
Number of events
Tau track pT (GeV), == 1 jet

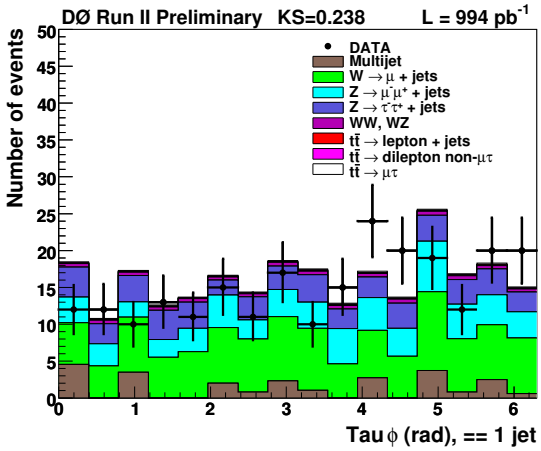
DØ Run II Preliminary KS=0.238 L = 994 pb-1
Number of events
DATA
Multijet
W → μ + jets
Z → μ-μ+ + jets
Z → τ-τ+ + jets
WW, WZ
tt̄ → lepton + jets
tt̄ → dilepton non-μτ
tt̄ → μτ
Tau φ (rad), == 1 jet

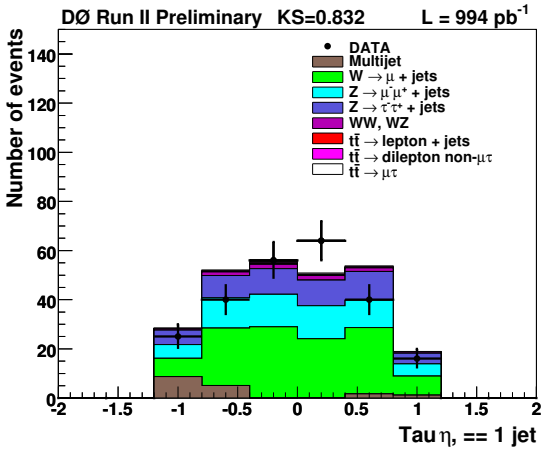
DØ Run II Preliminary KS=0.832 L = 994 pb-1
Number of events
DATA
Multijet
W → μ + jets
Z → μ-μ+ + jets
Z → τ-τ+ + jets
WW, WZ
tt̄ → lepton + jets
tt̄ → dilepton non-μτ
tt̄ → μτ
Tau η, == 1 jet

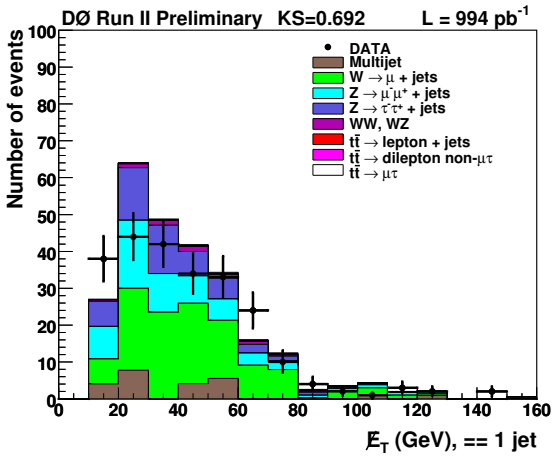
DØ Run II Preliminary KS=0.692 L = 994 pb-1
Number of events
DATA
Multijet
W → μ + jets
Z → μ-μ+ + jets
Z → τ-τ+ + jets
WW, WZ
tt̄ → lepton + jets
tt̄ → dilepton non-μτ
tt̄ → μτ
ℰT (GeV), == 1 jet

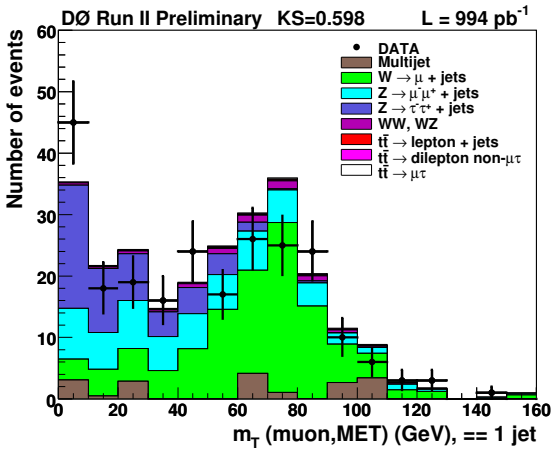
DØ Run II Preliminary KS=0.598 L = 994 pb-1
Number of events
DATA
Multijet
W → μ + jets
Z → μ-μ+ + jets
Z → τ-τ+ + jets
WW, WZ
tt̄ → lepton + jets
tt̄ → dilepton non-μτ
tt̄ → μτ
mT (muon,MET) (GeV), == 1 jet

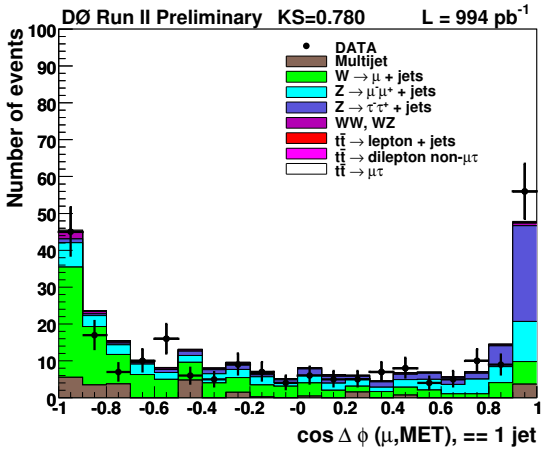
DØ Run II Preliminary KS=0.780 L = 994 pb-1
Number of events
DATA
Multijet
W → μ + jets
Z → μ-μ+ + jets
Z → τ-τ+ + jets
WW, WZ
tt̄ → lepton + jets
tt̄ → dilepton non-μτ
tt̄ → μτ
cos Δ φ (μ,MET), == 1 jet

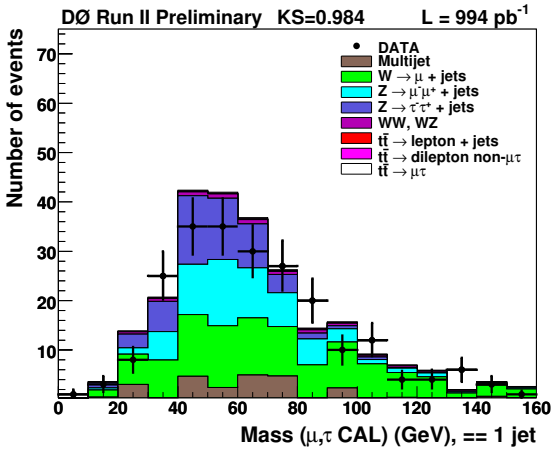
DØ Run II Preliminary KS=0.984 L = 994 pb-1
Number of events
DATA
Multijet
W → μ + jets
Z → μ-μ+ + jets
Z → τ-τ+ + jets
WW, WZ
tt̄ → lepton + jets
tt̄ → dilepton non-μτ
tt̄ → μτ
Mass (μ,τ CAL) (GeV), == 1 jet

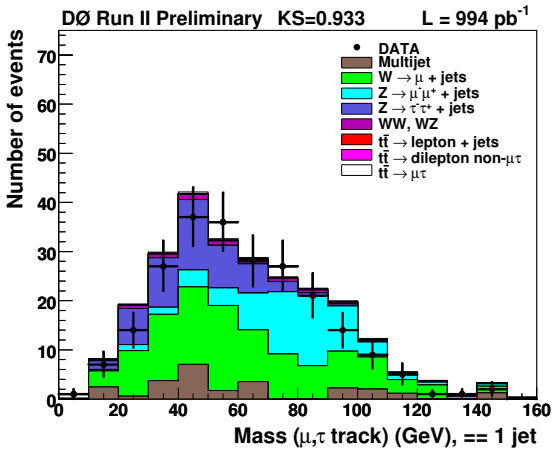
DØ Run II Preliminary KS=0.933 L = 994 pb-1
DATA
Multijet
W → μ + jets
Z → μ⁻μ⁺ + jets
Z → τ⁻τ⁺ + jets
WW, WZ
tt̄ → lepton + jets
tt̄ → dilepton non-μτ
tt̄ → μτ
Number of events
Mass (μ,τ track) (GeV), == 1 jet

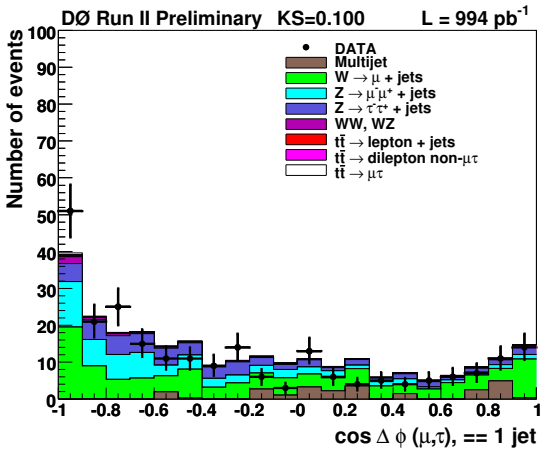
DØ Run II Preliminary KS=0.100 L = 994 pb-1
DATA
Multijet
W → μ + jets
Z → μ⁻μ⁺ + jets
Z → τ⁻τ⁺ + jets
WW, WZ
tt̄ → lepton + jets
tt̄ → dilepton non-μτ
tt̄ → μτ
Number of events
cos Δ φ (μ,τ), == 1 jet

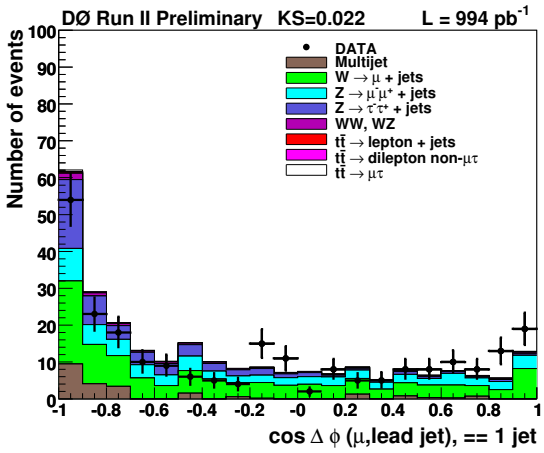
DØ Run II Preliminary KS=0.022 L = 994 pb-1
DATA
Multijet
W → μ + jets
Z → μ⁻μ⁺ + jets
Z → τ⁻τ⁺ + jets
WW, WZ
tt̄ → lepton + jets
tt̄ → dilepton non-μτ
tt̄ → μτ
Number of events
cos Δ φ (μ,lead jet), == 1 jet

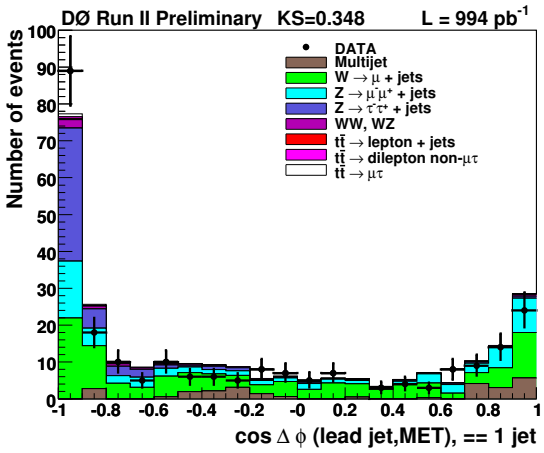
DØ Run II Preliminary KS=0.348 L = 994 pb-1
DATA
Multijet
W → μ + jets
Z → μ⁻μ⁺ + jets
Z → τ⁻τ⁺ + jets
WW, WZ
tt̄ → lepton + jets
tt̄ → dilepton non-μτ
tt̄ → μτ
Number of events
cos Δ φ (lead jet,MET), == 1 jet

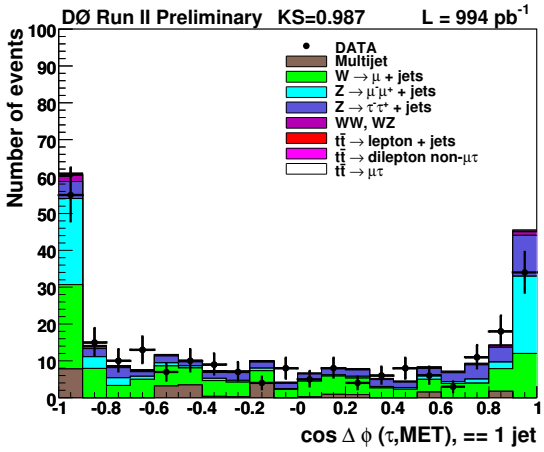
DØ Run II Preliminary KS=0.987 L = 994 pb-1
DATA
Multijet
W → μ + jets
Z → μ⁻μ⁺ + jets
Z → τ⁻τ⁺ + jets
WW, WZ
tt̄ → lepton + jets
tt̄ → dilepton non-μτ
tt̄ → μτ
Number of events
cos Δ φ (τ,MET), == 1 jet

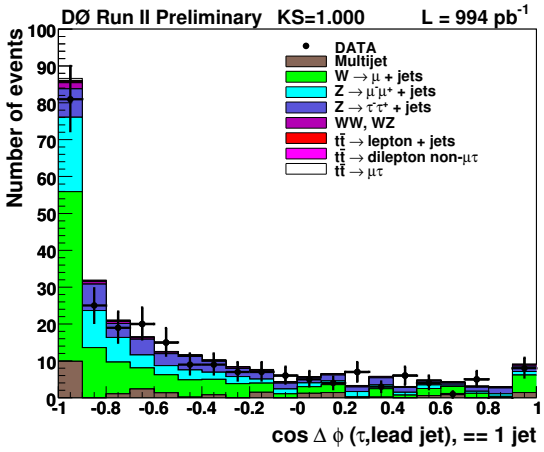
DØ Run II Preliminary KS=1.000 L = 994 pb-1
DATA
Multijet
W → μ + jets
Z → μ⁻μ⁺ + jets
Z → τ⁻τ⁺ + jets
WW, WZ
tt̄ → lepton + jets
tt̄ → dilepton non-μτ
tt̄ → μτ
Number of events
cos Δ φ (τ,lead jet), == 1 jet

A.2 Two-jet inclusive sample

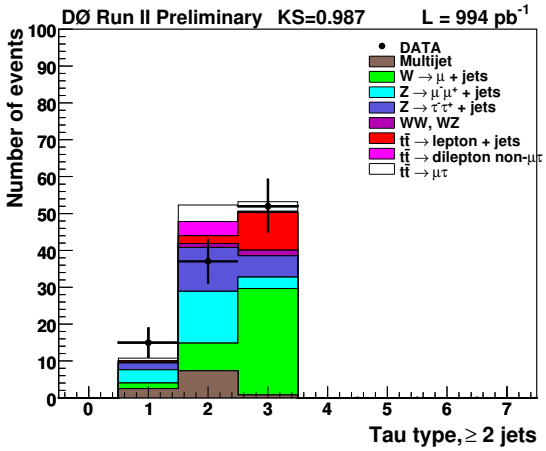

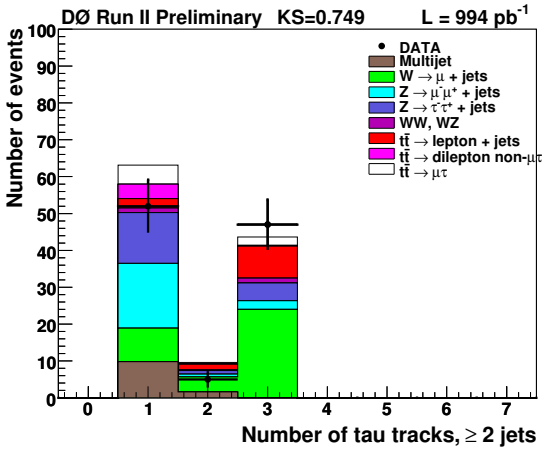

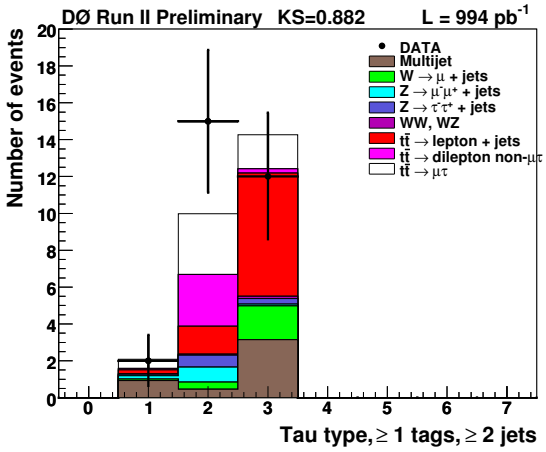

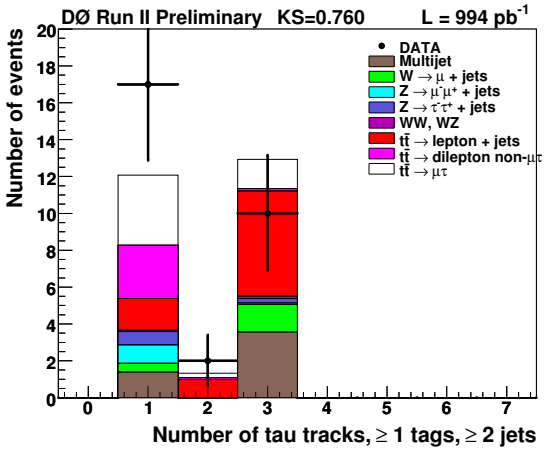

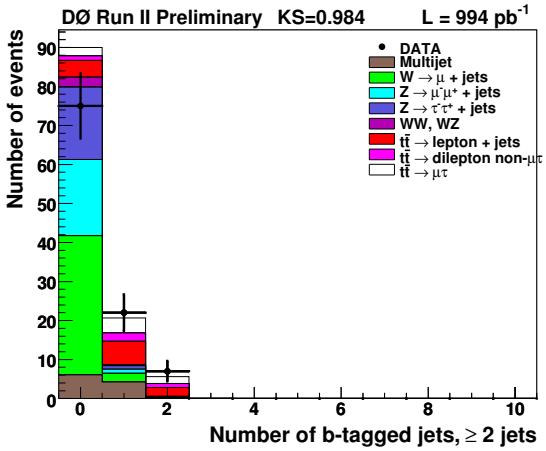

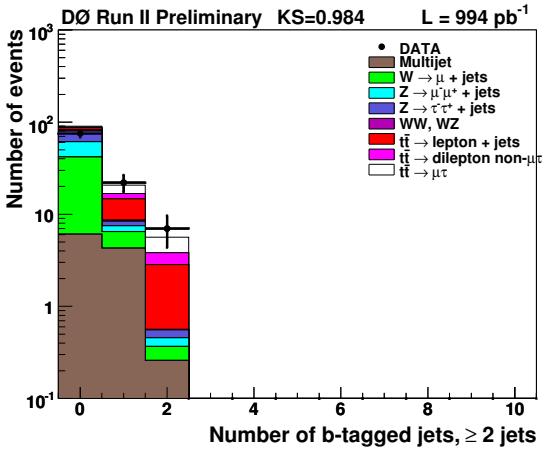

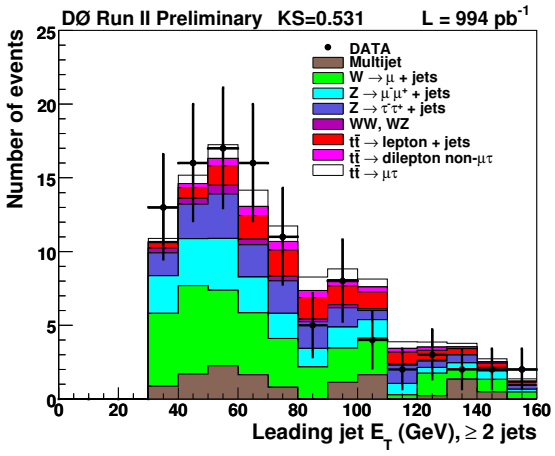
DØ Run II Preliminary KS=0.531 L = 994 pb-1
Number of events
Leading jet ET (GeV), ≥ 2 jets
DATA
Multijet
W → μ + jets
Z → μ+μ- + jets
Z → τ+τ- + jets
WW, WZ
tt̄ → lepton + jets
tt̄ → dilepton non-μτ
tt̄ → μτ

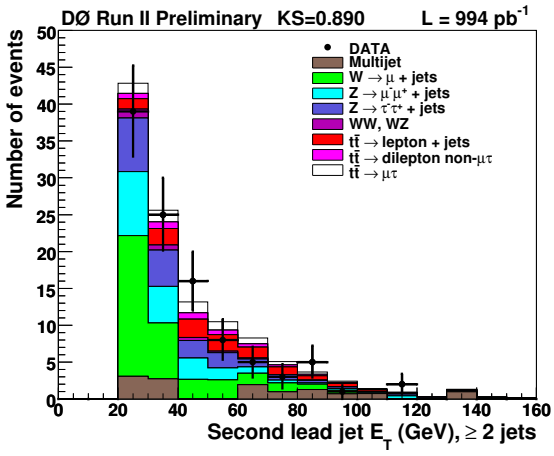
DØ Run II Preliminary KS=0.890 L = 994 pb-1
Number of events
Second lead jet ET (GeV), ≥ 2 jets
DATA
Multijet
W → μ + jets
Z → μ+μ- + jets
Z → τ+τ- + jets
WW, WZ
tt̄ → lepton + jets
tt̄ → dilepton non-μτ
tt̄ → μτ

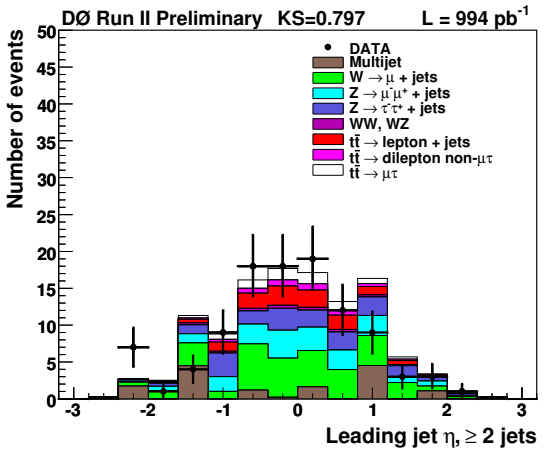
DØ Run II Preliminary KS=0.797 L = 994 pb-1
Number of events
Leading jet η, ≥ 2 jets
DATA
Multijet
W → μ + jets
Z → μ+μ- + jets
Z → τ+τ- + jets
WW, WZ
tt̄ → lepton + jets
tt̄ → dilepton non-μτ
tt̄ → μτ

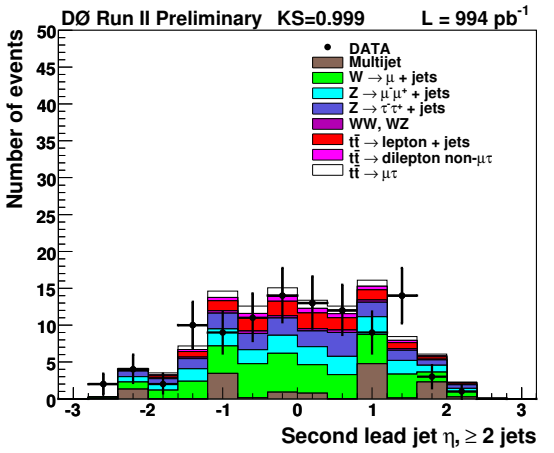
DØ Run II Preliminary KS=0.999 L = 994 pb-1
Number of events
Second lead jet η, ≥ 2 jets
DATA
Multijet
W → μ + jets
Z → μ+μ- + jets
Z → τ+τ- + jets
WW, WZ
tt̄ → lepton + jets
tt̄ → dilepton non-μτ
tt̄ → μτ

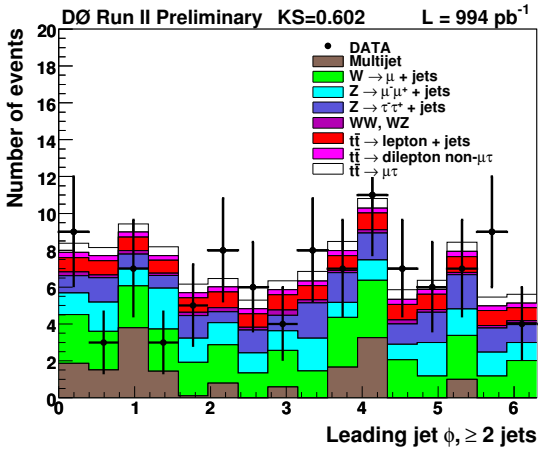
DØ Run II Preliminary KS=0.602 L = 994 pb-1
Number of events
Leading jet φ, ≥ 2 jets
DATA
Multijet
W → μ + jets
Z → μ+μ- + jets
Z → τ+τ- + jets
WW, WZ
tt̄ → lepton + jets
tt̄ → dilepton non-μτ
tt̄ → μτ

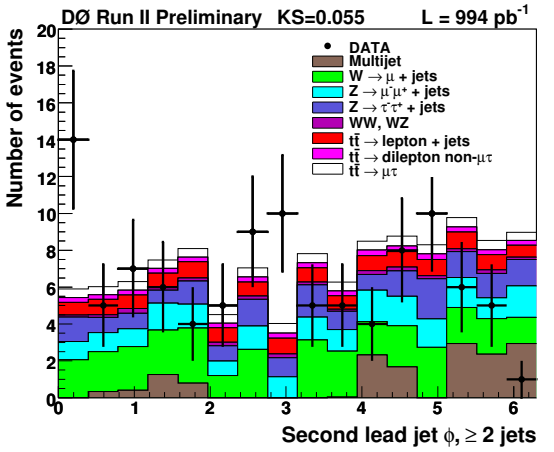
DØ Run II Preliminary KS=0.055 L = 994 pb-1
Number of events
Second lead jet φ, ≥ 2 jets
DATA
Multijet
W → μ + jets
Z → μ+μ- + jets
Z → τ+τ- + jets
WW, WZ
tt̄ → lepton + jets
tt̄ → dilepton non-μτ
tt̄ → μτ

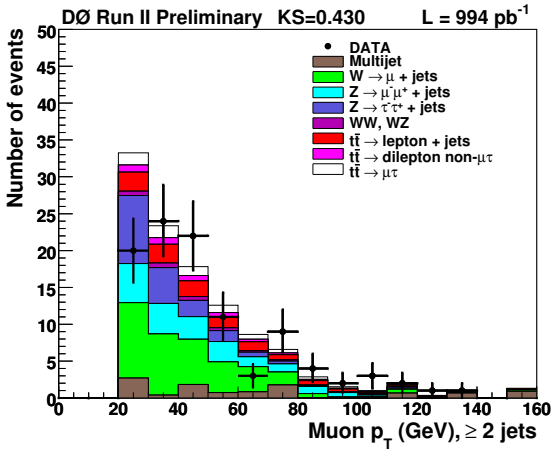
DØ Run II Preliminary KS=0.430 L = 994 pb-1
Number of events
DATA
Multijet
W → μ + jets
Z → μ-μ+ + jets
Z → τ-τ+ + jets
WW, WZ
tt̄ → lepton + jets
tt̄ → dilepton non-μτ
tt̄ → μτ
Muon pT (GeV), ≥ 2 jets

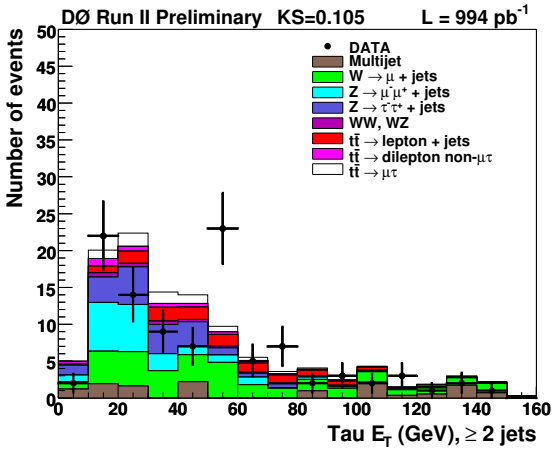
DØ Run II Preliminary KS=0.105 L = 994 pb-1
Number of events
DATA
Multijet
W → μ + jets
Z → μ-μ+ + jets
Z → τ-τ+ + jets
WW, WZ
tt̄ → lepton + jets
tt̄ → dilepton non-μτ
tt̄ → μτ
Tau ET (GeV), ≥ 2 jets

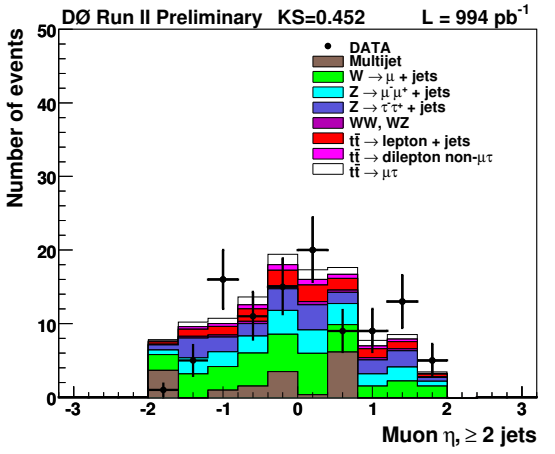
DØ Run II Preliminary KS=0.452 L = 994 pb-1
Number of events
DATA
Multijet
W → μ + jets
Z → μ-μ+ + jets
Z → τ-τ+ + jets
WW, WZ
tt̄ → lepton + jets
tt̄ → dilepton non-μτ
tt̄ → μτ
Muon η, ≥ 2 jets

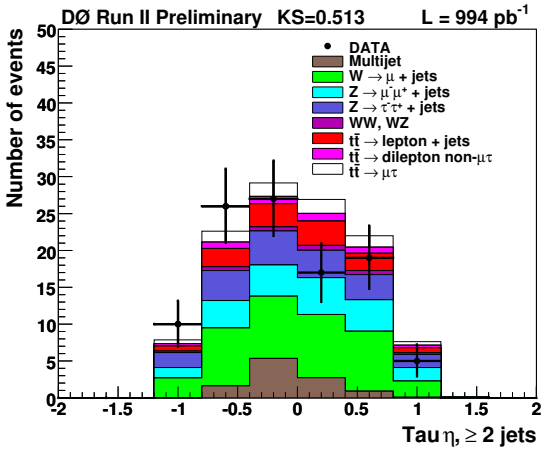
DØ Run II Preliminary KS=0.513 L = 994 pb-1
Number of events
DATA
Multijet
W → μ + jets
Z → μ-μ+ + jets
Z → τ-τ+ + jets
WW, WZ
tt̄ → lepton + jets
tt̄ → dilepton non-μτ
tt̄ → μτ
Tau η, ≥ 2 jets

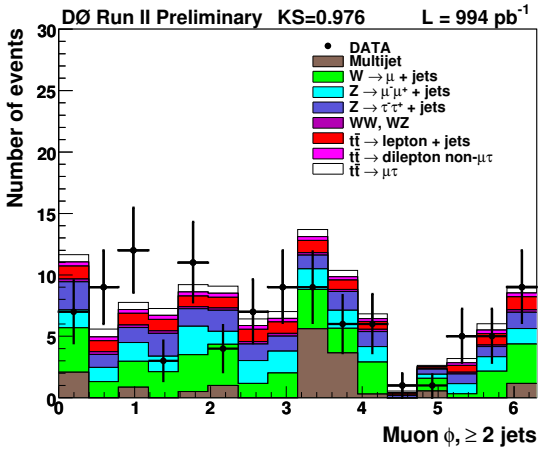
DØ Run II Preliminary KS=0.976 L = 994 pb-1
Number of events
DATA
Multijet
W → μ + jets
Z → μ-μ+ + jets
Z → τ-τ+ + jets
WW, WZ
tt̄ → lepton + jets
tt̄ → dilepton non-μτ
tt̄ → μτ
Muon φ, ≥ 2 jets

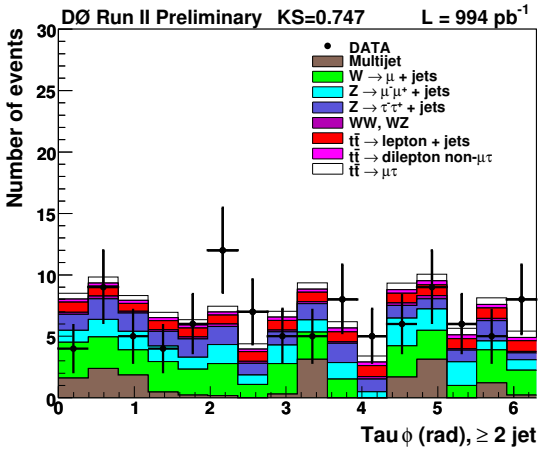
DØ Run II Preliminary KS=0.747 L = 994 pb-1
Number of events
DATA
Multijet
W → μ + jets
Z → μ-μ+ + jets
Z → τ-τ+ + jets
WW, WZ
tt̄ → lepton + jets
tt̄ → dilepton non-μτ
tt̄ → μτ
Tau φ (rad), ≥ 2 jet

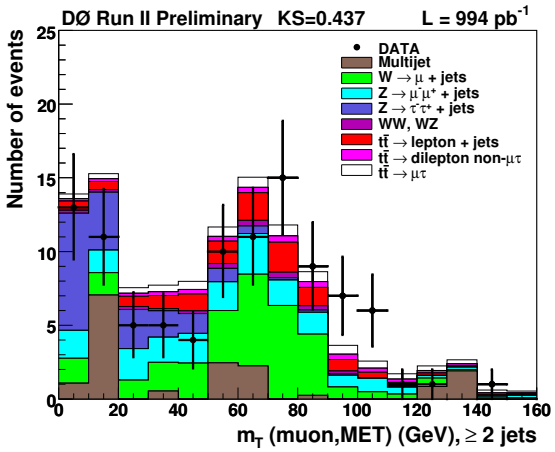
DØ Run II Preliminary KS=0.437 L = 994 pb-1
Number of events
DATA
Multijet
W → μ + jets
Z → μ-μ+ + jets
Z → τ-τ+ + jets
WW, WZ
tt̄ → lepton + jets
tt̄ → dilepton non-μτ
tt̄ → μτ
mT (muon,MET) (GeV), ≥ 2 jets

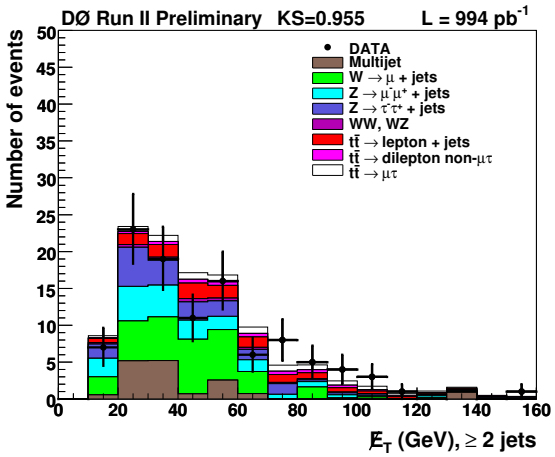
DØ Run II Preliminary KS=0.955 L = 994 pb-1
Number of events
DATA
Multijet
W → μ + jets
Z → μ-μ+ + jets
Z → τ-τ+ + jets
WW, WZ
tt̄ → lepton + jets
tt̄ → dilepton non-μτ
tt̄ → μτ
ÆT (GeV), ≥ 2 jets

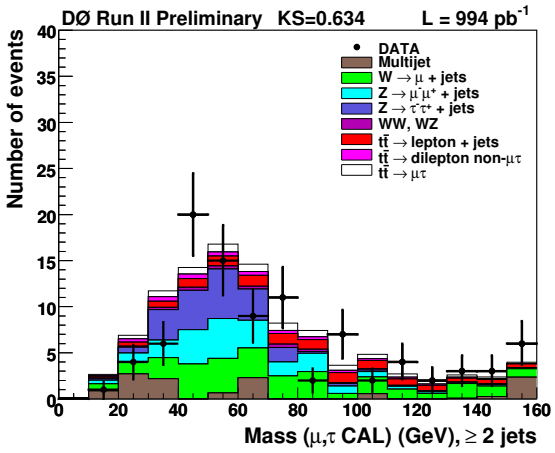
DØ Run II Preliminary KS=0.634 L = 994 pb-1
Number of events
DATA
Multijet
W → μ + jets
Z → μ-μ+ + jets
Z → τ-τ+ + jets
WW, WZ
tt̄ → lepton + jets
tt̄ → dilepton non-μτ
tt̄ → μτ
Mass (μ,τ CAL) (GeV), ≥ 2 jets

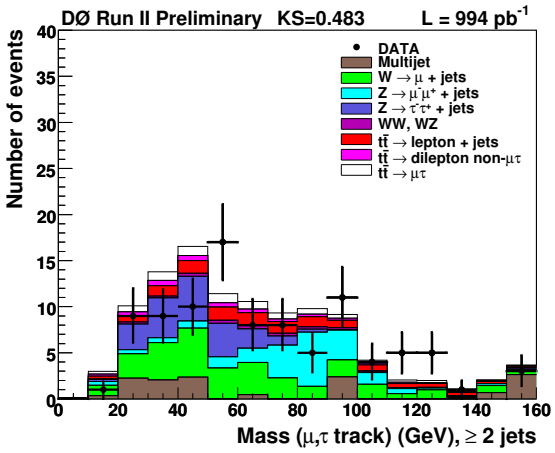
DØ Run II Preliminary KS=0.483 L = 994 pb-1
Number of events
DATA
Multijet
W → μ + jets
Z → μ-μ+ + jets
Z → τ-τ+ + jets
WW, WZ
tt̄ → lepton + jets
tt̄ → dilepton non-μτ
tt̄ → μτ
Mass (μ,τ track) (GeV), ≥ 2 jets

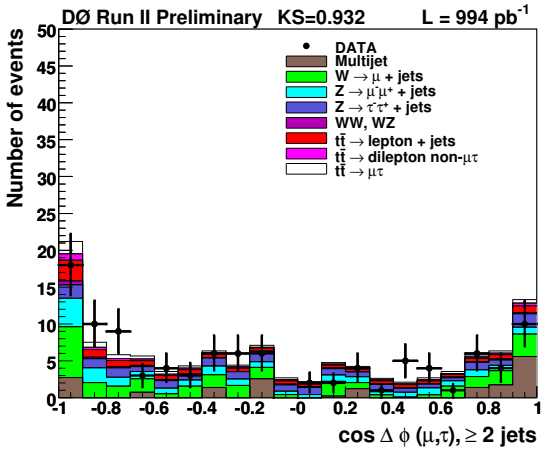
DØ Run II Preliminary KS=0.932 L = 994 pb-1
Number of events
DATA
Multijet
W → μ + jets
Z → μ-μ+ + jets
Z → τ-τ+ + jets
WW, WZ
tt̄ → lepton + jets
tt̄ → dilepton non-μτ
tt̄ → μτ
cos Δ φ (μ,τ), ≥ 2 jets

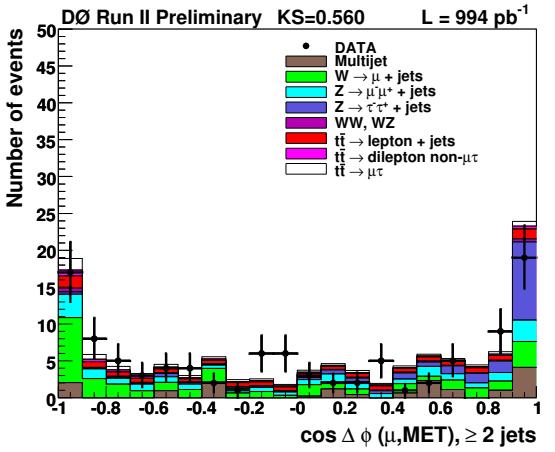
DØ Run II Preliminary KS=0.560 L = 994 pb-1
Number of events
DATA
Multijet
W → μ + jets
Z → μ-μ+ + jets
Z → τ-τ+ + jets
WW, WZ
tt̄ → lepton + jets
tt̄ → dilepton non-μτ
tt̄ → μτ
cos Δ φ (μ,MET), ≥ 2 jets

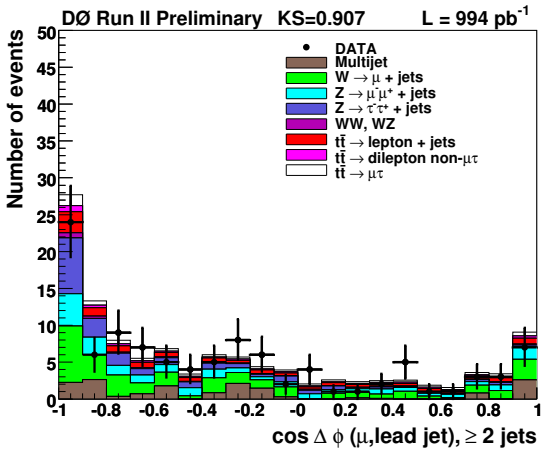
DØ Run II Preliminary KS=0.907 L = 994 pb-1
Number of events
DATA
Multijet
W → μ + jets
Z → μ⁻μ⁺ + jets
Z → τ⁻τ⁺ + jets
WW, WZ
tt̄ → lepton + jets
tt̄ → dilepton non-μτ
tt̄ → μτ
cos Δ φ (μ,lead jet), ≥ 2 jets

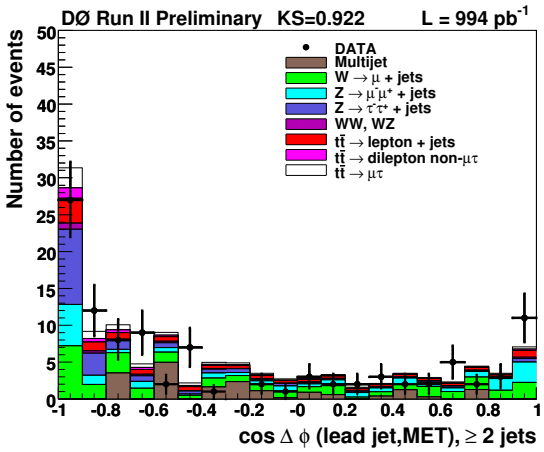
DØ Run II Preliminary KS=0.922 L = 994 pb-1
Number of events
DATA
Multijet
W → μ + jets
Z → μ⁻μ⁺ + jets
Z → τ⁻τ⁺ + jets
WW, WZ
tt̄ → lepton + jets
tt̄ → dilepton non-μτ
tt̄ → μτ
cos Δ φ (lead jet,MET), ≥ 2 jets

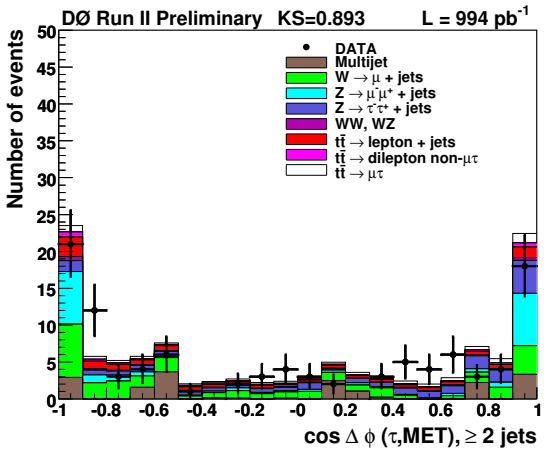
DØ Run II Preliminary KS=0.893 L = 994 pb-1
Number of events
DATA
Multijet
W → μ + jets
Z → μ⁻μ⁺ + jets
Z → τ⁻τ⁺ + jets
WW, WZ
tt̄ → lepton + jets
tt̄ → dilepton non-μτ
tt̄ → μτ
cos Δ φ (τ,MET), ≥ 2 jets

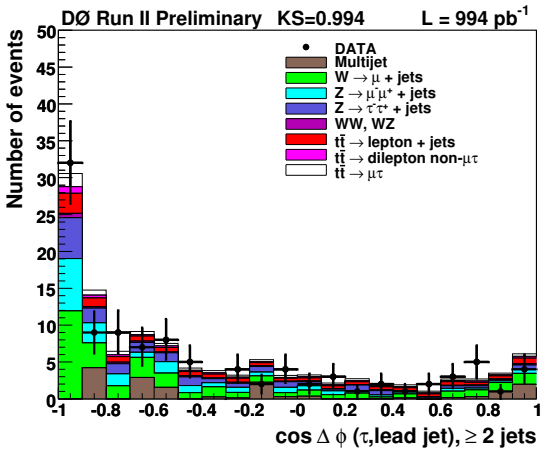
DØ Run II Preliminary KS=0.994 L = 994 pb-1
Number of events
DATA
Multijet
W → μ + jets
Z → μ⁻μ⁺ + jets
Z → τ⁻τ⁺ + jets
WW, WZ
tt̄ → lepton + jets
tt̄ → dilepton non-μτ
tt̄ → μτ
cos Δ φ (τ,lead jet), ≥ 2 jets

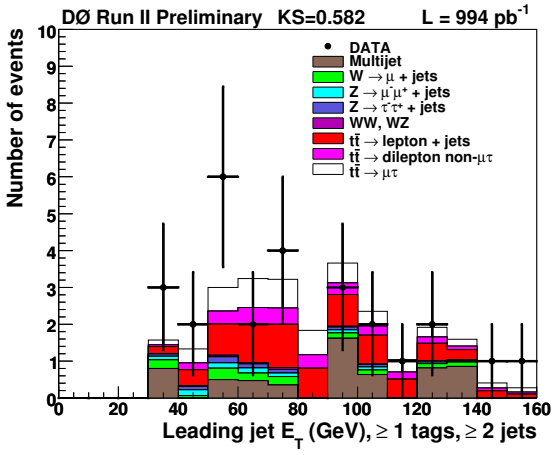
DØ Run II Preliminary KS=0.582 L = 994 pb-1
Number of events
DATA
Multijet
W → μ + jets
Z → μ-μ+ + jets
Z → τ-τ+ + jets
WW, WZ
tt̄ → lepton + jets
tt̄ → dilepton non-μτ
tt̄ → μτ
Leading jet ET (GeV), ≥ 1 tags, ≥ 2 jets

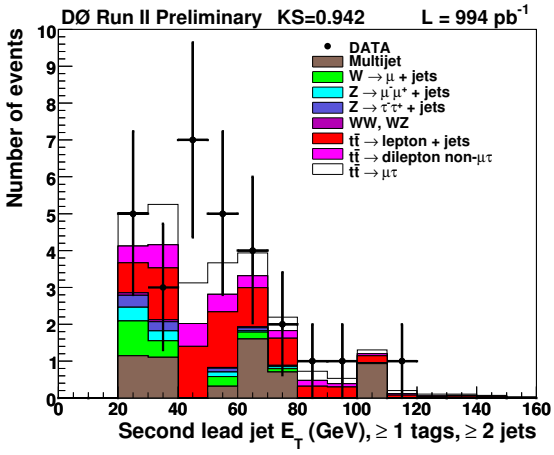
DØ Run II Preliminary KS=0.942 L = 994 pb-1
Number of events
DATA
Multijet
W → μ + jets
Z → μ-μ+ + jets
Z → τ-τ+ + jets
WW, WZ
tt̄ → lepton + jets
tt̄ → dilepton non-μτ
tt̄ → μτ
Second lead jet ET (GeV), ≥ 1 tags, ≥ 2 jets

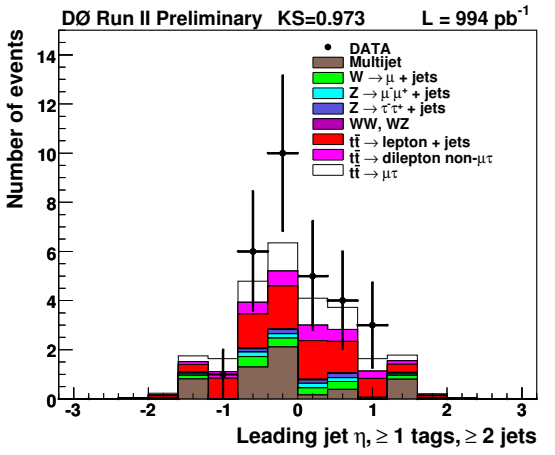
DØ Run II Preliminary KS=0.973 L = 994 pb-1
Number of events
DATA
Multijet
W → μ + jets
Z → μ-μ+ + jets
Z → τ-τ+ + jets
WW, WZ
tt̄ → lepton + jets
tt̄ → dilepton non-μτ
tt̄ → μτ
Leading jet η, ≥ 1 tags, ≥ 2 jets

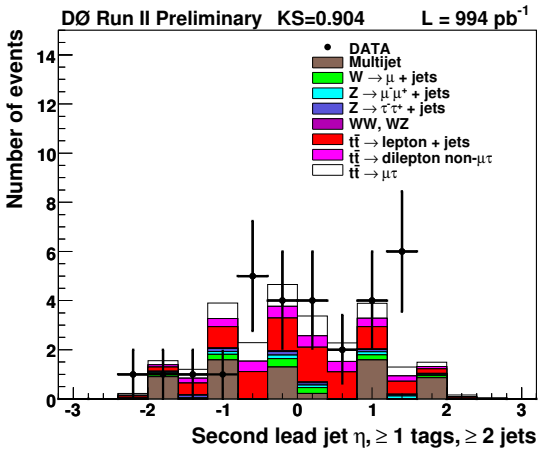
DØ Run II Preliminary KS=0.904 L = 994 pb-1
Number of events
DATA
Multijet
W → μ + jets
Z → μ-μ+ + jets
Z → τ-τ+ + jets
WW, WZ
tt̄ → lepton + jets
tt̄ → dilepton non-μτ
tt̄ → μτ
Second lead jet η, ≥ 1 tags, ≥ 2 jets

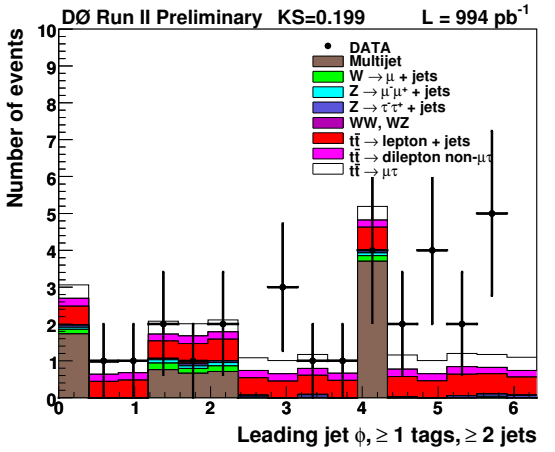
DØ Run II Preliminary KS=0.199 L = 994 pb-1
Number of events
DATA
Multijet
W → μ + jets
Z → μ-μ+ + jets
Z → τ-τ+ + jets
WW, WZ
tt̄ → lepton + jets
tt̄ → dilepton non-μτ
tt̄ → μτ
Leading jet φ, ≥ 1 tags, ≥ 2 jets

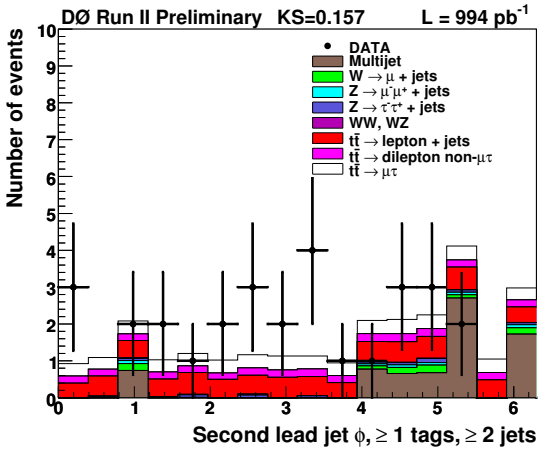
DØ Run II Preliminary KS=0.157 L = 994 pb-1
Number of events
DATA
Multijet
W → μ + jets
Z → μ-μ+ + jets
Z → τ-τ+ + jets
WW, WZ
tt̄ → lepton + jets
tt̄ → dilepton non-μτ
tt̄ → μτ
Second lead jet φ, ≥ 1 tags, ≥ 2 jets

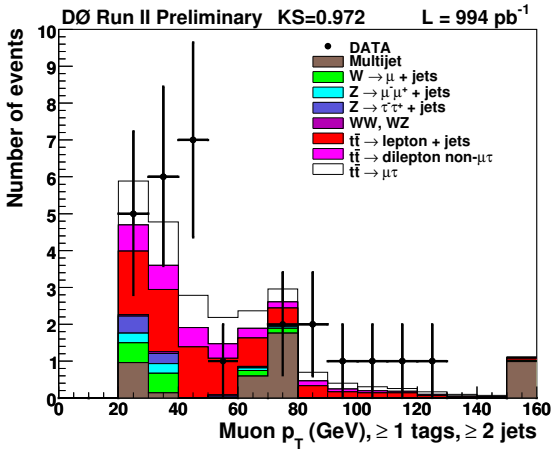
DØ Run II Preliminary KS=0.972 L = 994 pb-1
Number of events
DATA
Multijet
W → μ + jets
Z → μ-μ+ + jets
Z → τ-τ+ + jets
WW, WZ
tt̄ → lepton + jets
tt̄ → dilepton non-μτ
tt̄ → μτ
Muon pT (GeV), ≥ 1 tags, ≥ 2 jets

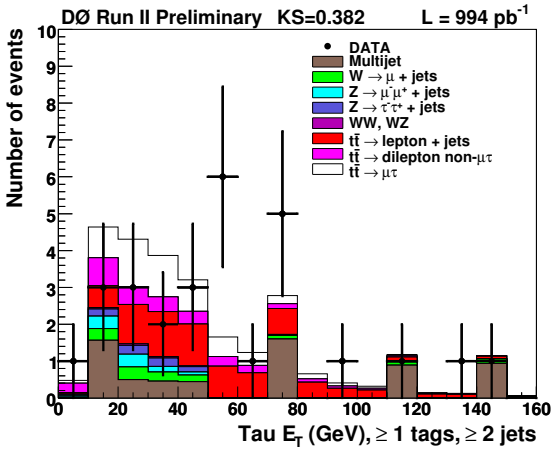
DØ Run II Preliminary KS=0.382 L = 994 pb-1
Number of events
DATA
Multijet
W → μ + jets
Z → μ-μ+ + jets
Z → τ-τ+ + jets
WW, WZ
tt̄ → lepton + jets
tt̄ → dilepton non-μτ
tt̄ → μτ
Tau ET (GeV), ≥ 1 tags, ≥ 2 jets

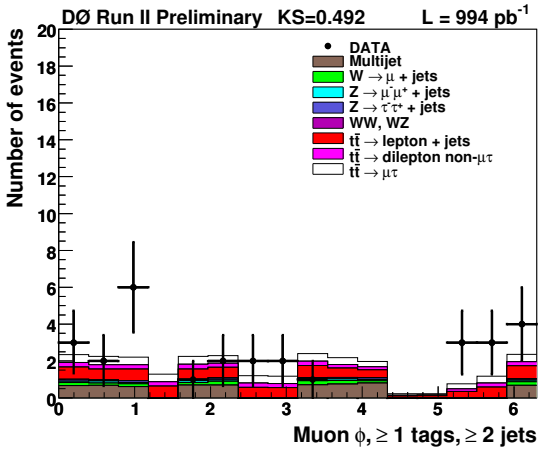
DØ Run II Preliminary KS=0.492 L = 994 pb-1
Number of events
DATA
Multijet
W → μ + jets
Z → μ-μ+ + jets
Z → τ-τ+ + jets
WW, WZ
tt̄ → lepton + jets
tt̄ → dilepton non-μτ
tt̄ → μτ
Muon φ, ≥ 1 tags, ≥ 2 jets

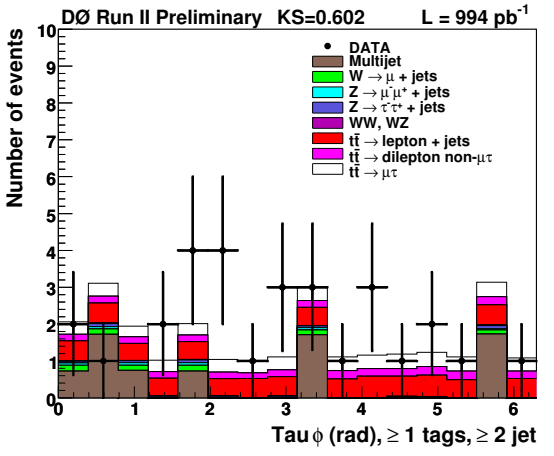
DØ Run II Preliminary KS=0.602 L = 994 pb-1
Number of events
DATA
Multijet
W → μ + jets
Z → μ-μ+ + jets
Z → τ-τ+ + jets
WW, WZ
tt̄ → lepton + jets
tt̄ → dilepton non-μτ
tt̄ → μτ
Tau φ (rad), ≥ 1 tags, ≥ 2 jet

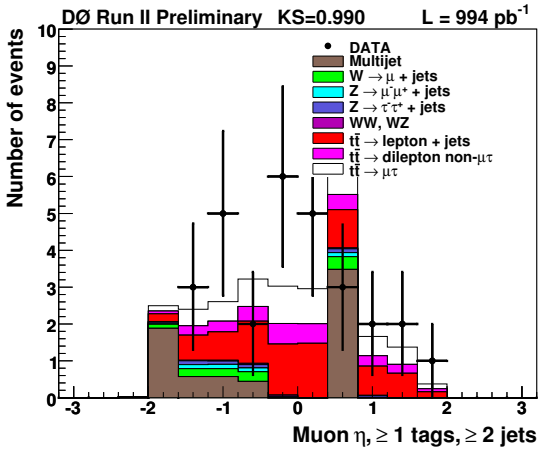
DØ Run II Preliminary KS=0.990 L = 994 pb-1
Number of events
DATA
Multijet
W → μ + jets
Z → μ-μ+ + jets
Z → τ-τ+ + jets
WW, WZ
tt̄ → lepton + jets
tt̄ → dilepton non-μτ
tt̄ → μτ
Muon η, ≥ 1 tags, ≥ 2 jets

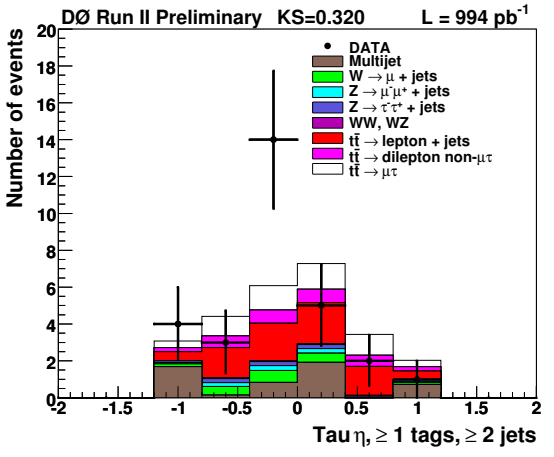
DØ Run II Preliminary KS=0.320 L = 994 pb-1
Number of events
DATA
Multijet
W → μ + jets
Z → μ-μ+ + jets
Z → τ-τ+ + jets
WW, WZ
tt̄ → lepton + jets
tt̄ → dilepton non-μτ
tt̄ → μτ
Tau η, ≥ 1 tags, ≥ 2 jets

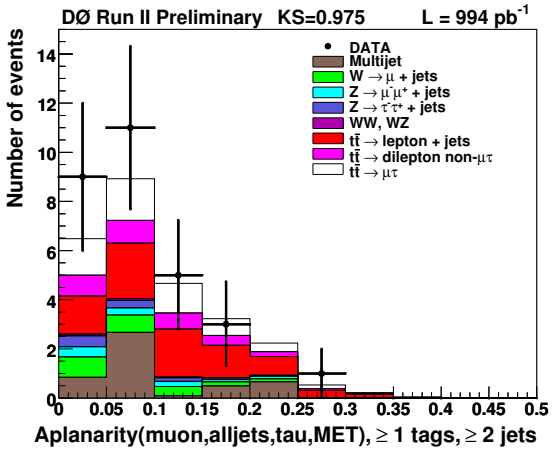
DØ Run II Preliminary KS=0.975 L = 994 pb-1
Number of events
DATA
Multijet
W → μ + jets
Z → μ⁻μ⁺ + jets
Z → τ⁻τ⁺ + jets
WW, WZ
tt̄ → lepton + jets
tt̄ → dilepton non-μτ
tt̄ → μτ
Aplanarity(muon,alljets,tau,MET), ≥ 1 tags, ≥ 2 jets

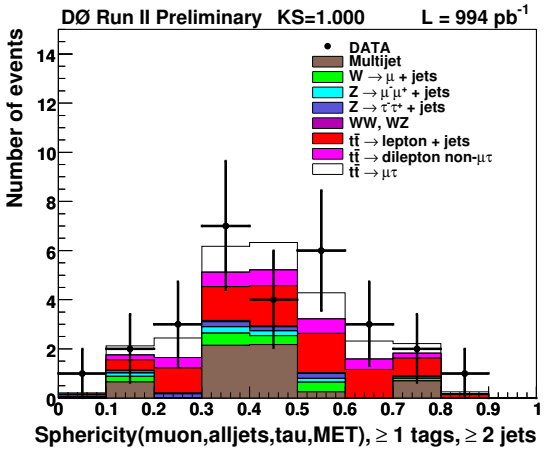
DØ Run II Preliminary KS=1.000 L = 994 pb-1
Number of events
DATA
Multijet
W → μ + jets
Z → μ⁻μ⁺ + jets
Z → τ⁻τ⁺ + jets
WW, WZ
tt̄ → lepton + jets
tt̄ → dilepton non-μτ
tt̄ → μτ
Sphericity(muon,alljets,tau,MET), ≥ 1 tags, ≥ 2 jets

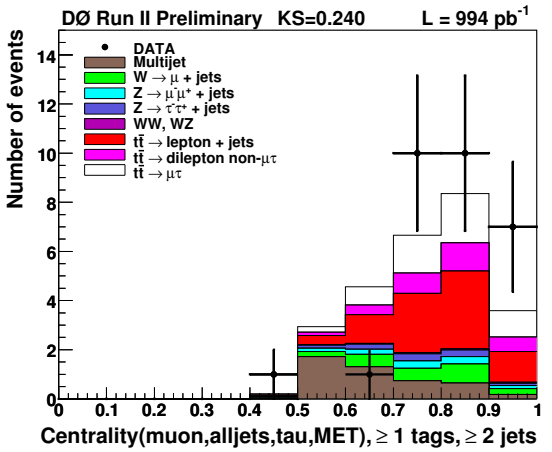
DØ Run II Preliminary KS=0.240 L = 994 pb-1
Number of events
DATA
Multijet
W → μ + jets
Z → μ⁻μ⁺ + jets
Z → τ⁻τ⁺ + jets
WW, WZ
tt̄ → lepton + jets
tt̄ → dilepton non-μτ
tt̄ → μτ
Centrality(muon,alljets,tau,MET), ≥ 1 tags, ≥ 2 jets

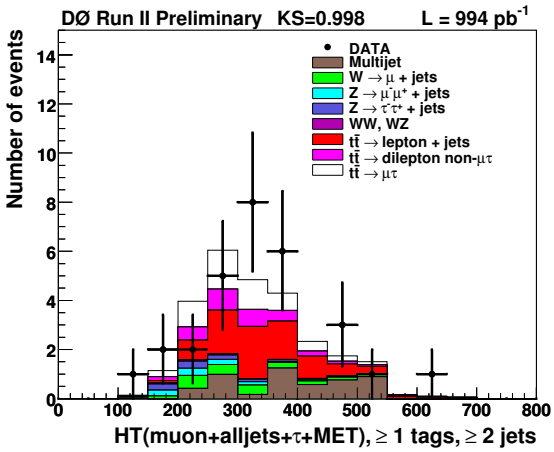
DØ Run II Preliminary KS=0.998 L = 994 pb-1
Number of events
DATA
Multijet
W → μ + jets
Z → μ⁻μ⁺ + jets
Z → τ⁻τ⁺ + jets
WW, WZ
tt̄ → lepton + jets
tt̄ → dilepton non-μτ
tt̄ → μτ
HT(muon+alljets+τ+MET), ≥ 1 tags, ≥ 2 jets

REFERENCES

[1] LEP Electroweak Working Group, Alcaraz, J. and others, *A combination of preliminary electroweak measurements and constraints on the standard model*, hep-ex/0612034.

[2] DØ Collaboration, S. Abachi *et al.*, *Observation of the top quark*, *Phys. Rev. Lett.* **74** (1995) 2632–2637, hep-ex/9503003.

[3] CDF Collaboration, F. Abe *et al.*, *Observation of top quark production in $p\bar{p}$ collisions*, *Phys. Rev. Lett.* **74** (1995) 2626–2631, hep-ex/9503002.

[4] M. Cacciari, S. Frixione, M. L. Mangano, P. Nason, and G. Ridolfi, *The $t\bar{t}$ cross-section at 1.8 TeV and 1.98 TeV: A study of the systematics due to parton densities and scale dependence*, *JHEP* **04** (2004) 068, hep-ph/0303085.

[5] N. Kidonakis and R. Vogt, *Next-to-next-to-leading order soft-gluon corrections in top quark hadroproduction*, *Phys. Rev.* **D68** (2003) 114014, hep-ph/0308222.

[6] DØ Collaboration, , "Measurement of the $t\bar{t}$ pair production cross-section in $p\bar{p}$ collisions at $\sqrt{s} = 1.96$ TeV in the lepton+jets final state using lifetime tagging on 900 pb^{-1} of DØ data." DØ Note 5355-CONF, 2007. `http://www-d0.fnal.gov/Run2Physics/WWW/results/prelim/TOP/T43`.

[7] DØ Collaboration, "DØ Top Quark Physics Results." `http://www-d0.fnal.gov/Run2Physics/top/top_public_web_pages/top_public.html`.

[8] DØ Collaboration, V. M. Abazov *et al.*, *Measurement of the $t\bar{t}$ production cross section in $p\bar{p}$ collisions at $\sqrt{s} = 1.96$ TeV in dilepton final states*, *Phys. Lett.* **B626** (2005) 55, hep-ex/0505082.

[9] DØ Collaboration, V. M. Abazov *et al.*, *Measurement of the $t\bar{t}$ production cross section in $p\bar{p}$ collisions using dilepton events*, *Phys. Rev.* **D76** (2007) 052006, arXiv:0706.0458 [hep-ex].

[10] DØ Collaboration, V. M. Abazov *et al.*, *Measurement of the $t\bar{t}$ production cross section in $p\bar{p}$ collisions at $\sqrt{s} = 1.96$ TeV using kinematic characteristics of lepton + jets events*, *Phys. Lett.* **B626** (2005) 45, hep-ex/0504043.

[11] DØ Collaboration, V. M. Abazov *et al.*, *Measurement of the $t\bar{t}$ production cross section in $p\bar{p}$ collisions at $\sqrt{s} = 1.96$ TeV using lepton + jets events with lifetime b−tagging*, *Phys. Lett.* **B626** (2005) 35, hep-ex/0504058.

[12] DØ Collaboration, V. M. Abazov *et al.*, *Measurement of the $t\bar{t}$ production cross section in $p\bar{p}$ collisions at $\sqrt{s} = 1.96$ TeV using secondary vertex b tagging*, *Phys. Rev.* **D74** (2006) 112004, hep-ex/0611002.

[13] DØ Collaboration, "Measurement of $\sigma(p\bar{p} \to t\bar{t})$ in $\tau+$ jets channel." DØ Note 5234-CONF, 2006. `http://www-d0.fnal.gov/Run2Physics/WWW/results/prelim/TOP/T38`.

[14] DØ Collaboration, V. M. Abazov *et al.*, *Measurement of the $p\bar{p} \to t\bar{t}$ production cross section at $\sqrt{s} = 1.96$ TeV in the fully hadronic decay channel*, hep-ex/0612040.

[15] MARK I Collaboration, M. L. Perl *et al.*, *Evidence for Anomalous Lepton Production in e^+e^- Annihilation*, *Phys. Rev. Lett.* **35** (1975) 1489–1492.

[16] CDF Collaboration, F. Abe *et al.*, *The $\mu\tau$ and $e\tau$ decays of top quark pairs produced in $p\bar{p}$ collisions at $\sqrt{s} = 1.8$ TeV*, *Phys. Rev. Lett.* **79** (1997) 3585–3590, hep-ex/9704007.

[17] CDF Collaboration, A. Abulencia *et al.*, *A Search for $t \to \tau\nu q$ in $t\bar{t}$ Production*, *Phys. Lett.* **B639** (2006) 172, hep-ex/0510063.

[18] S. Levy and H. Frisch, "Search for anomalous τ production in $b-$tagged top quark events." CDF Note 8353, 2006.

[19] S. Tourneur and A. Savoy-Navarro, "Search for $t\bar{t}$ in τ dilepton channels based on 350 pb^{-1} of CDF data." CDF Note 8376, 2006.

[20] J. F. Gunion, H. E. Haber, G. L. Kane, and S. Dawson, *The Higgs Hunter's Guide*. Westview Press, paperback ed., 2000.

[21] Particle Data Group, W. M. Yao *et al.*, *Review of Particle Physics*, *J. Phys.* **G33** (2006) 1–1232.

[22] DØ Collaboration, V. M. Abazov *et al.*, *The Upgraded DØ Detector*, *Nucl. Instrum. Meth.* **A565** (2005) 463–537, physics/0507191. FERMILAB-PUB-05-341-E.

[23] J. Simkin and C. W. Trowbridge, "Three-Dimensional Computer Program (TOSCA) for Non-Linear Electromagnetic Fields." Rutherford Appleton Laboratory report RL-79-097, 1979.

[24] T. Andeen, B. C. K. Casey, K. DeVaughan, Y. Enari, E. Gallas, D. Krop, R. Partridge, H. Schellman, G. R. Snow, S. Yacoob, and H.-D. Yoo, "The D0 Experiment's Integrated Luminosity for Tevatron Run IIa." FERMILAB-TM-2365, DØ Note 5398, 2007.

[25] A. Khanov, "HTF: histogramming method for finding tracks. The algorithm description." DØ Note 3778, 2000.

[26] P. V. C. Hough, *Machine analysis of bubble chamber pictures*, in *International Conference on High Energy Accelerators and Instrumentation* (L. Kowarski, ed.), (CERN), pp. 554–556, 1959.

[27] D. Adams, "Finding Tracks." DØ Note 2958, 1998.

[28] H. Greenlee, "The DØ Kalman Track Fit." DØ Note 2004, 2004.

[29] R. E. Kálmán, *A New Approach to Linear Filtering and Prediction Problems*, *Transactions of the ASME - Journal of Basic Engineering* **82** (1960) 35–45.

[30] H. Greenlee, "The DØ Interacting propagator." DØ Note 4293, 2003.

[31] A. Schwartzman and C. Tully, "Primary Vertex Reconstruction by Means of Adaptive Vertex Fitting." DØ Note 4918, 2005.

[32] A. Schwartzman and M. Narain, "Probabilistic Primary Vertex Selection." DØ Note 4042, 2002.

[33] P. Calfayan, T. Gadfort, G. Hesketh, V. Lesne, M. Owen, R. Ströhmer, V. Sharyy, and B. Tuchming, "Muon Identification Certification for p17 data." DØ Note 5157, 2007.

[34] G. Hesketh, "Central Track Extrapolation Through the DØ Detector." DØ Note 4079, 2003.

[35] L. Duflot and M. Ridel, "The CellNN algorithm: cell level clustering in the DØ calorimeter." DØ Note 3923, 2001.

[36] DØ EM ID Group, "Electron/Photon ID Getting Started." `http://www-d0.fnal.gov/phys_id/emid/d0_private/emid_intro.html`.

[37] S.-J. Park, "EM Particle Documentation." `http://www-d0.fnal.gov/phys_id/emid/d0_private/EM_Particle_Documentation_EMID.html`.

[38] L. Wang, J. Hays, J. Mitrevski, and C. Schwanenberger, "Electron Likelihood Efficiency in p17." DØ Note 5114, 2006.

[39] G. C. Blazey, J. R. Dittmann, S. D. Ellis, V. D. Elvira, K. Frame, G. S., R. Hirosky, R. Peigaia, H. Schellman, R. Snihur, V. Sorin, and D. Zeppenfeld, *Run II Jet Physics*, in *QCD and Weak Boson Physics in Run II*, (Batavia), pp. 47–77, 1999. hep-ex/0005012.

[40] E. Busato and B. Andrieu, "Jet Algorithms in the DØ Run II Software: Description and User's Guide." DØ Note 4457, 2004.

[41] A. Harel, "Jet ID Optimization." DØ Note 4919, 2006.

[42] DØ Jet Energy Scale Group, "DØ Certified Preliminary Jet Energy Scale." `http://www-d0.fnal.gov/phys_id/jet/d0_private/certified/v07-01-02/jetcorr_v07-01-02.html`.

[43] N. Makovec and J.-F. Grivaz, "Shifting, Smearing and Removing Simulated Jets." DØ Note 4914, 2005.

[44] T. Scanlon, "A Neural-network $b-$tagging tool." DØ Note 4889, 2005.

[45] M. Anastasoaie, S. Robinson, and T. Scanlon, "Performance of the NN b-tagging tool on p17 data." DØ Note 5213, 2007.

[46] T. Scanlon, *$b-$tagging and the search for neutral supersymmetric Higgs bosons at DØ*. PhD thesis, Imperial College, University of London, 2006. FERMILAB-THESIS-2006-43.

[47] L. Sawyer and A. Stone, "Missing ET Reconstruction: Variables and Methods." DØ Note 3957, 2003.

[48] S. Trincaz-Duvoid and P. Verdier, "Missing ET Reconstruction in p17." DØ Note 4474, 2004.

[49] D. Chakraborty, Y. Coadou, S. Duensing, C. Galea, Y. Gershtein, A.-C. Le Bihan, C. Nöding, and S. Protopopescu, "Reconstruction of τ leptons in hadronic final states at DØ Run II." DØ Note 4210, 2003.

[50] DØ Data Quality Group. `http://www-d0.fnal.gov/computing/data_quality/d0_private/forusers.html`, 2006.

[51] S.-J. Park and M. Begel, "Efficiency of the Data Quality Calorimeter Flags." DØ Note 5324, 2007.

[52] M. L. Mangano, M. Moretti, F. Piccinini, R. Pittau, and A. D. Polosa, *ALPGEN, a generator for hard multiparton processes in hadronic collisions*, *JHEP* **07** (2003) 001, hep-ph/0206293.

[53] S. Höche, F. Krauss, N. Lavesson, L. Lönnblad, M. Mangano, A. Schälicke, and S. Schumann, *Matching Parton Showers and Matrix Elements*, hep-ph/0602031.

[54] J. Alwall *et al.*, *Comparative study of various algorithms for mergin of parton showers and matrix elements in hadronic collisions*, arXiv:0706.2569 [hep-ph].

[55] T. Sjöstrand, L. Lonnblad, S. Mrenna, and P. Skands, PYTHIA *6.3: Physics and Manual*, hep-ph/0308153.

[56] S. Jadach, Z. Was, R. Decker, and J. H. Kuhn, *The tau decay library TAUOLA: Version 2.4*, *Comput. Phys. Commun.* **76** (1993) 361–380.

[57] D. J. Lange, *The* EVTGEN *particle decay simulation package*, *Nucl. Instrum. Meth.* **A462** (2001) 152–155, hep-ph/0109231.

[58] F. Febres Cordero, L. Reina, and D. Wackeroth, *NLO QCD corrections to W boson production with a massive b−quark jet pair at the Fermilab Tevatron $p\bar{p}$ collider*, *Phys. Rev.* **D74** (2006) 034007, hep-ph/0606102.

[59] J. Campbell, R. Keith Ellis, F. Maltoni, and S. Willenbrock, *Production of a W boson and two jets with one b-quark tag*, *Phys. Rev.* **D75** (2007) 054015, hep-ph/0606102.

[60] Y. Peters, M. Begel, E. Shabalina, and D. Wicke, "Study of the W+Jets heavy flavor scale factor in p17." DØ Note 5406, 2007.

[61] DØ Collaboration, , "Search for $ZH(\to \ell^+\ell^- b\bar{b})$ in $p\bar{p}$ collisions at $\sqrt{s} = 1960$ GeV." DØ Note 5482-CONF, 2007. `http://www-d0.fnal.gov/Run2Physics/WWW/results/prelim/HIGGS/H39`.

[62] R. J. Barlow and C. Beeston, *Fitting using finite Monte Carlo samples*, *Comput. Phys. Commun.* **77** (1993) 219–228.

[63] R. Hamberg, W. L. van Neerven, and T. Matsuura, *A complete calculation of the order α_s^2 correction to the Drell-Yan K factor*, *Nucl. Phys.* **B359** (1991) 343–405.

[64] M. Arthaud, M. Besancon, S. Chakrabarti, F. Deliot, E. Shabalina, and V. Sharry, "Measurement of the $t\bar{t}$ Production Cross-section at $\sqrt{s} = 1.96$ TeV in Electron Muon Final States using p17 data set." DØ Note 5360, 2007.

[65] D.-K. Cho, U. Heintz, M. Narain, S.-J. Park, R. Partridge, M.-A. Pleier, E. Shabalina, S. Sumowidagdo, M. Weber, and H.-D. Yoo, "Measurement of the $t\bar{t}$ Production Cross-Section at $\sqrt{s} = 1.96$ TeV in the Lepton+Jets Final State using Neural Network b-tagging algorithm on 1 fb^{-1} of DØ Data." DØ Note 5335, 2007.

[66] M. Owen, S. Soldner-Rembold, and X. Goddon, "Search for Neutral Higgs in the Decay Channel Tau(mu) Tau with p17 Data." DØ Note 5252, 2006.

[67] DØ Collaboration, "Measurement of $t\bar{t}$ Production Cross-Section in the Lepton + Tau + b-jet(s) + Missing Transverse Energy Channel Using 1 fb^{-1} of Run II Data." DØ Note 5451-CONF, 2007. `http://www-d0.fnal.gov/Run2Physics/WWW/results/prelim/TOP/T58`.

[68] E. Shabalina, "Combined $t\bar{t}$ Production Cross Section at $\sqrt{s} = 1.96$ TeV in the Lepton+Jets and Dilepton Final States using Event Topology." DØ Note 4906, 2005.

BIOGRAPHICAL SKETCH

Suharyo Sumowidagdo

The author was born in the city of Singaraja, Province of Bali, Indonesia. He obtained his undergraduate degree from the Department of Physics, University of Indonesia in 1999, with an honor thesis in phenomenology and data analysis of kaon electromagnetic production on nucleon target. He continued his education at the same university, leading to a master's degree in 2001 with a thesis on Regge phenomenology in kaon photoproduction.

During his years at University of Indonesia, he learned about many important discoveries in physics: the top quark, the existence of neutrino mass, and the mysterious dark energy and the accelerating universe. Outside campus, he witnessed the Indonesian 1998 Revolution that toppled the authoritarian New Order regime and brought a new and democratic government in Indonesia.

In the fall of 2001, he started his graduate education at Department of Physics, Florida State University. He joined the DØ experiment at Fermilab in the summer of 2002, and later moved to Fermilab permanently in the summer of 2003. During his stay at Fermilab, he worked mainly on detector operations, control systems, tau lepton algorithm, and physics of top quark.